CENTRO DE INVESTIGACIÓN Y DE ESTUDIOS AVANZADOS
DEL INSTITUTO POLITÉCNICO NACIONAL

UNIDAD ZACATENCO
DEPARTAMENTO DE FÍSICA

"Sobre algunas características cuánticas de los estados coherentes de la bicapa de grafeno"

Tesis que presenta

Dennis Itzel Martínez Moreno

para obtener el Grado de

Doctora en Ciencias

en la Especialidad de

Física

Director de tesis: Dr. David José Fernández Cabrera

Ciudad de México Octubre, 2023

CENTER FOR RESEARCH AND ADVANCED STUDIES OF THE NATIONAL POLYTECHNIC INSTITUTE

UNIT ZACATENCO
PHYSICS DEPARTMENT

"On some quantum features of bilayer graphene coherent states"

by

Dennis Itzel Martínez Moreno

In order to obtain the

Doctor of Science

degree, speciality in

Physics

Advisor: Ph. D. David José Fernández Cabrera

Mexico City October, 2023

Dedicado a,

Mi querida familia, que en el día a día con su presencia, apoyo y amor me impulsan para salir adelante, además de saber que mis logros también son los suyos.

Agradecimientos

Agradezco de manera muy especial a mi mamá y hermanos. Su amor y apoyo incondicional han sido fundamentales para mí. Este logro no habría sido posible sin ellos.

Me gustaría expresar mi sincera gratitud a mi asesor, Dr. David José Fernández Cabrera, por su orientación experta y su apoyo constante durante mi maestría y doctorado. Además, me gustaría agradecerle por todas las oportunidades que me ha brindado impulsando mi desarrollo profesional. Sus conocimientos y consejos han sido invaluables.

Agradezco a mis sinodales: Dr. David Bermúdez Rosales, Dr. Alonso Contreras Astorga, Dr. Erik Díaz Bautista y Dr. Omar Gustavo Miranda Romagnoli por su tiempo, dedicación y valiosos comentarios durante la revisión de mi tesis.

A los profesores Dr. Javier Negro Vadillo y Dr. Luis Miguel Nieto Calzada por su hospitalidad durante mi estancia en Valladolid. Sus valiosos consejos y contribuciones han sido de gran ayuda para este trabajo.

Quiero expresar mi agradecimiento a Rodrigo Díaz por su constante compañía y apoyo incondicional durante todos estos años.

Finalmente, agradezco al CONAHCyT por la beca de doctorado número 786589 y al CINVESTAV por el apoyo recibido para culminar este trabajo.

Este trabajo ha sido apoyado por el proyecto FORDECYT PRONACES/61533/2020.

Dennis Itzel Martínez Moreno.

Contents

List of Figures

Resumen

En este trabajo, estudiamos la interacción de los electrones en la bicapa de grafeno con un campo magnético constante, homogéneo perpendicular a la superficie de la bicapa. Partiendo del hamiltoniano que describe a la bicapa de grafeno, resolvemos el problema de manera exacta encontrando los niveles de energía del sistema y sus funciones propias asociadas, lo cual constituye el enfoque mecánico-cuántico estándar. Sin embargo, es posible estudiar este sistema desde una perspectiva alternativa derivando los llamados estados coherentes. Estos estados representan un enfoque semi-clásico que proporciona información complementaria a la obtenida por el método estándar.

Consideramos los estados coherentes de la bicapa de grafeno (ECBG), derivados en un trabajo anterior, y exploramos la dinámica del sistema estudiando su evolución temporal a través de la función de autocorrelación, obteniendo el período de evolución de estos estados, es decir, el tiempo en el que el estado coherente evolucionado coincide con el inicial. Además, se calculan las escalas de tiempo asociadas con los ECBG, con el objetivo de analizar la llamada estructura de *revivals* para la bicapa de grafeno.

En la misma línea, también se han derivado los estados coherentes multifotónicos. Estos estados representan una generalización de los ECBG, los cuales se definen como estados propios de un operador de aniquilación generalizado con un valor propio complejo. Además, se analizan algunas cantidades físicas para estos estados, incluyendo la relación de incertidumbre de Heisenberg, la densidad de probabilidad, el valor medio de la energía y su evolución temporal.

Como complemento a estos estudios, analizamos el mismo sistema utilizando ahora un *gauge* simétrico y coordenadas polares. Derivamos los ECBG con simetría radial. Luego, las densidades de corriente se derivan en detalle para la bicapa de grafeno y se calculan para los estados propios del sistema y para los estados coherentes con simetría radial.

Abstract

In this work, we study the interaction of electrons in bilayer graphene with a constant homogeneous magnetic field perpendicular to the bilayer surface. Starting from the Hamiltonian describing the bilayer graphene, we solve the problem exactly by finding the energy levels of the system and their associated eigenfunctions, which constitutes the standard quantum mechanical framework. However, it is possible to study this system from an alternative perspective by deriving the so-called coherent states. These states represent a semi-classical approach that supplies complementary information to that obtained by the standard method.

We consider the bilayer graphene coherent states (BGCS), derived in a previous work, and the dynamics of the system is explored by studying their time evolution through the autocorrelation function, obtaining the evolution period of these states, *i.e.*, the time at which the evolved coherent state coincides with the initial one. Additionally, the time scales associated with the BGCS are calculated, with the aim of analyzing the so-called *revivals* structure for bilayer graphene.

In the same line, the multiphoton coherent states have also been derived. These states represent a generalization of the BGCS, which are defined as eigenstates of a generalized annihilation operator with a complex eigenvalue. In addition, some physical quantities are analyzed for these states, including the Heisenberg uncertainty relation, probability density, mean energy value, and their time evolution.

As a complement to these studies, we analyze the same system now using a symmetric gauge and polar coordinates. We derived the BGCS with radial symmetry. Then, the current densities are derived in detail for bilayer graphene and computed for the eigenstates of the system and the radially symmetric coherent states.

Chapter 1

Introduction

Carbon is the basis of all organic chemistry. Due to the flexibility of carbon bonds, it is possible to obtain different structures, each of them with a variety of interesting physical properties. Graphene, an allotrope of carbon, is formed by a single layer of carbon atoms organized in a hexagonal lattice structure [1, 2]. For decades, the scientific community has theorized on the possible existence and fabrication of such 2D-material, starting from Wallace who in 1946 wrote the first work about the band structure of graphene [3], until Geim and Novoselov who in 2004 rediscovered and isolated graphene [4]. Thus, extensive theoretical and experimental research have been carried out on this material. A particularly interesting characteristic of graphene is that its low-energy excitations are massless chiral Dirac fermions that move at a velocity $v_0 = c/300$. These Dirac fermions behave in unusual ways compared with conventional electrons placed in external magnetic fields, leading to physical phenomena referred to as anomalous integer quantum Hall effect [5,6]. Furthermore, several studies have examined the monolayer graphene under different magnetic field profiles, determining its energy levels and corresponding eigenfunctions through supersymmetric quantum mechanics [7, 8].

Nowadays, it is possible to produce few-layer carbon systems; the simplest one, which is composed of two layers, is called bilayer graphene and it was initially reported in 2004 [4]. Bilayer graphene can exist in several stacking configurations [14, 15]. In the AA configuration the two layers align perfectly to each other. On the other hand, in the AB configuration, also known as Bernal stacking, half of the carbon atoms of the top layer align directly above to atoms of the bottom layer, while the remaining atoms are placed above the center of the hexagons of the bottom layer. This particular configuration is the most stable one in nature. Finally, when the two layers are rotated to an specific angle, known as *magic angle*, bilayer graphene takes on a unique special form. This rotation induces the appearance of unconventional superconductivity and Mott-like insulating states [16, 17]. However, in this work we will focus on the most prevalent configuration, namely, Bernal stacking.

The electronic band structure of bilayer graphene is typically examined using the tight-binding model [18, 19], leading to the existence of four energy bands, two conduction and two valence bands. At certain symmetry points, a conduction band touches a valence band at zero energy. This implies that, at low energies, the electrons in bilayer graphene behave as chiral quasiparticles with effective mass m^* and parabolic dispersion relation $E = \pm p^2/2m^*$, different from the linear relationship found in monolayer graphene. Recently, some research have been conducted into the behavior of chiral electrons in bilayer graphene placed in a different magnetic field profiles [20, 21].

Coherent states have been recently derived [22] in the simplest case, where graphene is placed in a constant homogeneous magnetic field perpendicular to its surface. The importance of coherent states, from both theoretical and experimental viewpoints, in various fields of physics is well recognized [24–26]. These states were first derived by Schrödinger in 1926 for the harmonic oscillator [28] and their importance has grown since then. The most notable applications appeared in the early 60s, when Glauber, Klauder, and Sudarshan used them to describe coherent electromagnetic radiation [29–35]. Recently, these states and their generalizations have been used to study systems based on graphene [41–45]. This supplies us with an alternative semi-classical approach supplementing the information that can be obtained from the standard quantum mechanical perspective.

On the other hand, one of the most prominent features of coherent states is their time stability, *i.e.*, when a coherent state evolves in time it keeps its shape or coherence without deformation [46]. In this way, its shape remains constant over time and its center follows the motion of a classical particle in a harmonic oscillator potential. It is well known that the time stability of coherent states comes from the fact that the energy levels for the harmonic oscillator are equally spaced [46], thus their evolution period is $T = 2\pi/\omega$, where ω is the angular frequency of the harmonic oscillator. In contrast, quantum systems without equidistant energy levels generally lack such a stability [47–49].

Coherent states can be expanded or generalized, *i.e.*, defined appropriately in order to characterize various systems in diverse fields of physics. Specifically, the so-called multiphoton coherent states (MCS) are typically derived as eigenstates of powers of the annihilation operator [56–58]. These have been obtained recently for the harmonic oscillator within the framework of polynomial Heisenberg algebras [59–63]. The MCS have also recently been generated for the supersymmetric harmonic oscillator [64]. Let us notice that the MCS can be used as non-classical states of light for multiphoton precesses occurring in the matter-radiation interaction [66, 67].

With this in mind, and inspired by the pioneering work on coherent states for monolayer graphene [22], a similar methodology will be applied in this work to derive the coherent states for bilayer graphene (BGCS) placed in a constant homogeneous magnetic field perpendicular to the bilayer surface [50] (see also [51]). Starting from this derivation, different quantum properties and generalizations of these states will be analyzed throughout this thesis.

This thesis begins with a brief overview of certain fundamental aspects of graphene focusing, in particular, on the bilayer graphene in order to understand better the system under study (see chapter 2). In its initial section, we examine the crystal structure of bilayer graphene and its band structure in order to determine the Hamiltonian describing the electrons of bilayer graphene. It is important to mention that this description in the low energy regime is schematic and brief; for a more detailed study we refer the reader to [18]. After establishing this Hamiltonian, we proceed to calculate the energies and eigenfunctions considering the interaction of electrons of the bilayer graphene with constant homogeneous magnetic field perpendicular to the bilayer surface, using the minimum coupling rule and the well-known Landau gauge. Chapter 2 ends with the calculation of the probability and current densities for these eigenfunctions, often referred to as Landau states of bilayer graphene.

Chapter 3 addresses the derivation of the BGCS, which was carried out for the first time in our previous study [50]. After deriving these states, we focus on exploring the dynamics of the system, with special emphasis on studying the time evolution of the BGCS. In this analysis, an expression is supplied

to calculate approximately the period of evolution. Additionally, the revival structure of these coherent states will be explored and their associate time scales will be computed. By using the autocorrelation function, we will make evident these scales, which will allow us to analyze the time evolution of the BGCS through an additional tool.

Chapter 4 extends and generalizes the coherent states approach to bilayer graphene, by deriving the corresponding multiphoton coherent states. These states are defined as eigenstates of a generalized annihilation operator with complex eigenvalue $\tilde{\alpha}$. Several physical quantities are determined to describe the system using these MCS including the Heisenberg uncertainty relation, probability density and mean energy value. The time evolution and the time-correlation function for the MCS are also obtained.

In chapter 5, we analyze the bilayer graphene in a constant homogeneous magnetic field using a symmetric gauge and polar coordinates, instead of the Landau gauge used previously. First we construct the radially symmetric coherent states for bilayer graphene. Then, we derive and calculate the current densities of bilayer graphene for both the eigenstates of the system and the radially symmetric coherent states. The thesis ends up with the conclusions of this work in chapter 6, as well as with a discussion on the possible future directions of this research.

Chapter 2

Carbon materials: bilayer graphene

The flexibility of chemical bonding in systems formed by carbon atoms allows to obtain a number of different structures featuring a wide variety of physical properties [1]. There are allotropes of different dimensionality, such as the graphite and diamond (three-dimensional systems) or low-dimensional structures, as fullerenes and carbon nanotubes. Moreover, there is a two-dimensional (2D) carbon allotrope known as graphene, which is composed of a monolayer of carbon atoms arranged in a hexagonal crystal lattice [2, 4] and was the first produced stable 2D crystal. Its physical properties have attracted attention of the scientific community for the fundamental physics and important applications involved in their study [5, 9, 10]. Moreover, it is possible to manufacture few-layered carbon systems in order to increase the family of 2D materials, and the most natural one is bilayer graphene. In this chapter some important features about bilayer graphene will be briefly discussed.

2.1 The carbon atom and the sp^2-hybridization

The electronic configuration of carbon in its ground state is $1s^2 2s^2 2p^2$ [11]. The $2p$-orbitals, labelled $2p_x$, $2p_y$ and $2p_z$, are 4eV higher than the $2s$ orbital, then it is energetically favourable to excite one of the $2s$-electron pairs into one of the empty $2p$-orbitals, in order to form covalent bonds with other atoms, such as H, O or other carbon atoms. Consequently, the carbon atom is now said to be in an excited state, whose electron configuration turns out to be $1s^2 2s^1 2p^3$ (see figure 2.1(a)). Therefore, in the excited state there are four equivalent quantum mechanical states, and a superposition between the $|2s\rangle$ and n-$|2p_j\rangle$ states is called sp^n-hybridization [12].

When a superposition between the states $2s$ and two $2p$ orbitals (*e.g.* with the states $|2p_x\rangle$ and $|2p_y\rangle$) is carried out, one obtains the so-called sp^2-hybridization which is formed by three quantum states expressed by [12]

$$|sp_1^2\rangle = \frac{1}{\sqrt{3}}|2s\rangle - \sqrt{\frac{2}{3}}|2p_y\rangle, \tag{2.1a}$$

$$|sp_2^2\rangle = \frac{1}{\sqrt{3}}|2s\rangle - \sqrt{\frac{2}{3}}\left(\frac{\sqrt{3}}{2}|2p_x\rangle + \frac{1}{2}|2p_y\rangle\right), \tag{2.1b}$$

$$|sp_3^2\rangle = -\frac{1}{\sqrt{3}}|2s\rangle - \sqrt{\frac{2}{3}}\left(-\frac{\sqrt{3}}{2}|2p_x\rangle + \frac{1}{2}|2p_y\rangle\right). \tag{2.1c}$$

1

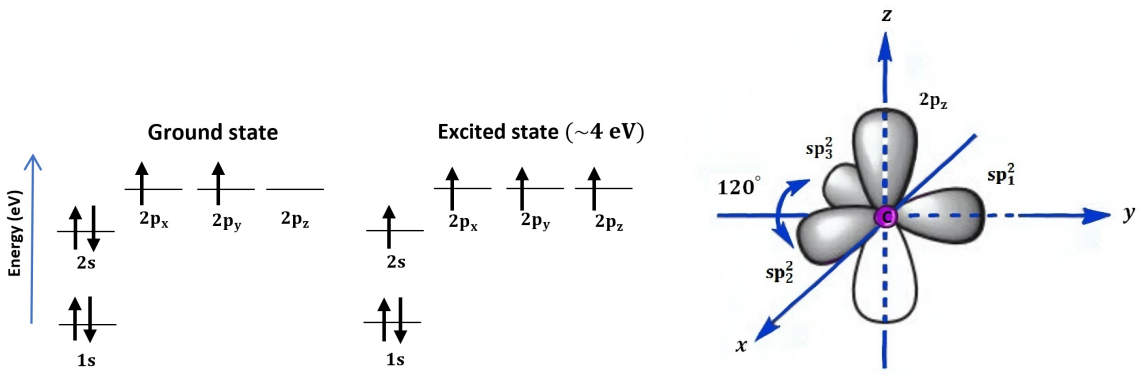

(a) (b)

Figure 2.1: (a) Electronic configurations for carbon atoms in the ground state and the first excited state. (b) sp^2-hybridization for carbon atoms.

These three hybridized orbitals lie on the xy-plane with mutual 120° angle difference and allow the formation of σ-bonds between the neighbouring atoms. The σ-bonds are responsible for the robustness of the lattice structure in all carbon allotropes, in particular, for the carbon atoms to condense in the hexagonal lattice of graphene. The remaining unhybridized $2p_z$-orbital is perpendicular to the plane and binds covalently with the nearby carbon atoms; then, since the $2p_z$-orbitals have one extra electron, a π-band is formed in each carbon atom, such that, is half filled (see figure 2.1(b)). These bands are responsible for the peculiar electronic properties of graphene at low energies [13]

On the other hand, in bilayer graphene (which consists of two graphene monolayers) the hybridization between the s-orbital and the p_z-orbitals is more complex. However, as for monolayer graphene, in bilayer graphene the π-bands are also formed and are half filled in the non-doping case, *i.e.*, the studies of the electronic properties of bilayer graphene are based on the knowledge of the electronic structure of monolayer graphene. Thus, in this chapter the study of the electrons in such π-bands will be discussed within the tight-binding approximation, which was originally addressed for the honeycomb lattice by Wallace in 1947 [3].

2.2 Electronic band structure of bilayer graphene

Bilayer graphene, which consists of two interacting layers of carbon atoms each with a honeycomb crystal structure, can exist in three different arrangements depending on its layer configurations [14], namely, *AA*, *AB* or Bernal phase, and twisted bilayer. The *AA* bilayer [15] is the most simple form and likely metastable, since its production has been reported very few works. On the other hand, the Bernal stacking is the most stable, and its is possible to produce high quality samples and study them in many experiments. Finally, in twisted bilayer graphene the top layer is rotated with respect to the lower layer by some angle θ. In this configuration the bilayer graphene displays unconventional superconductivity and Mott-like insulating states when the angle θ has a value of $\simeq 1.1^\circ$ (the magic angle) [16, 17]. In this work the *AB* arrangement or Bernal stacking will be considered.

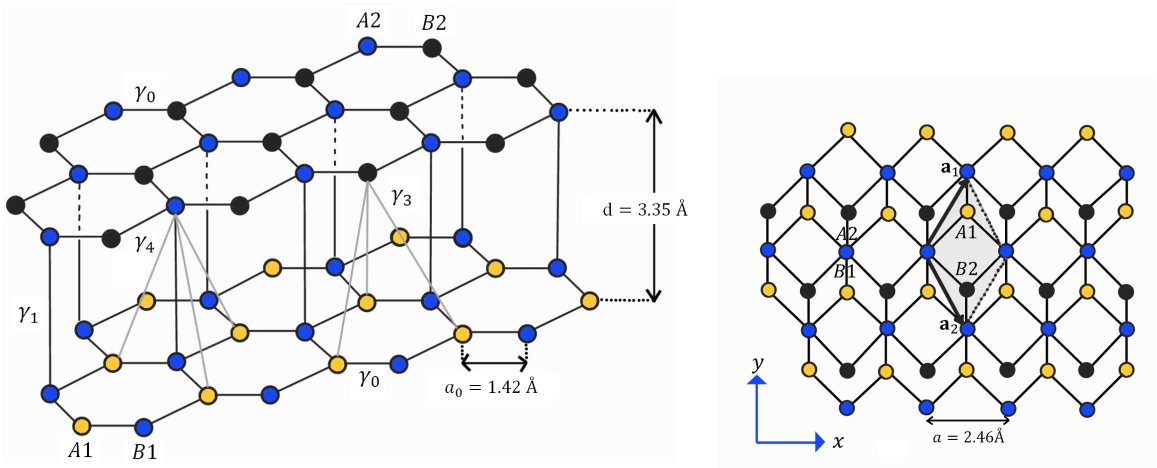

(a) (b)

Figure 2.2: (a) Lattice structure of bilayer graphene. The yellow and blue points correspond to the atoms A1 and B1 on the lower layer, while the blue and black points to the atoms A2 and B2 on the upper layer, respectively. (b) Bilayer graphene unit cell, indicated by a shaded rhombus.

2.2.1 The crystal structure

As mentioned before, bilayer graphene consists of two connected single layers of carbon atoms arranged in a hexagonal crystal lattice with a distance between adjacent carbon atoms of $a_0 = 1.42\text{Å}$ and an interlayer spacing of $d = 3.35\text{Å}$. The primitive lattice vectors $\mathbf{a}_1$ and $\mathbf{a}_2$ are defined by

$$\mathbf{a}_1 = \left(\frac{a}{2}, \frac{\sqrt{3}a}{2}\right), \qquad \mathbf{a}_2 = \left(\frac{a}{2}, -\frac{\sqrt{3}a}{2}\right), \tag{2.2}$$

where $a = |\mathbf{a}_1| = |\mathbf{a}_2|$ represents the distance between adjacent unit cell [2, 19]. Figure 2.2(a) shows the crystal structure of bilayer graphene .

All crystals can be described in terms of the geometry of this unit cell, which is defined as the smallest repeating unit having the full symmetry of the crystal structure. Each unit cell in bilayer graphene contains four carbon atoms, labelled A1, B1 for the lower layer and A2, B2 for the upper layer (see figure 2.2(b)). According to the Bernal stacking, the layers arrangement in bilayer graphene runs as follows: the B1-atoms on the lower layer are directly below to the A2-atoms from the upper layer and are known as dimer sites, while the other two atoms, A1 and B2, do not have any correspondence with atoms from the upper or lower layers, and referred to as non-dimer sites [19].

On the other hand, there is a set of points $\{\Gamma, M, K, K'\}$ known as crystallographic points, which play an important role in the electrons behavior of monolayer and bilayer graphene because their low-energy excitations are focused around points K and K', which belong to the so-called reciprocal space momentum space.

One can define the direct lattice or physical lattice in the same way as in real space. One can also define a reciprocal lattice in a space that represents the Fourier transform of the first lattice in real space.

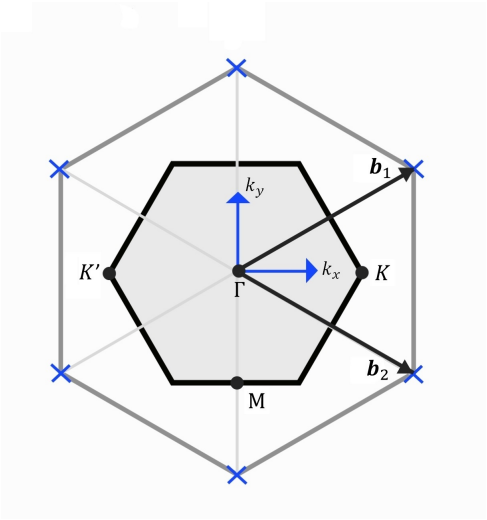

Figure 2.3: Reciprocal lattice of bilayer graphene showing the crystallographic points and the primitive reciprocal vectors.

The primitive reciprocal lattice vectors of bilayer graphene fulfill $\mathbf{a}_1 \cdot \mathbf{b}_1 = \mathbf{a}_2 \cdot \mathbf{b}_2 = 2\pi$ and $\mathbf{a}_1 \cdot \mathbf{b}_2 = \mathbf{a}_2 \cdot \mathbf{b}_1 = 0$, which are given by

$$\mathbf{b}_1 = \left(\frac{2\pi}{a}, \frac{2\pi}{\sqrt{3}a}\right), \qquad \mathbf{b}_2 = \left(\frac{2\pi}{a}, -\frac{2\pi}{\sqrt{3}a}\right). \tag{2.3}$$

These crystallographic points are shown in figure 2.3. Note that, the reciprocal lattice is a hexagonal Bravais lattice and the shaded hexagon represents the first Brillouin zone which is analogous to the unit cell in reciprocal space.

2.2.2 The tight-binding model

The electronic band structure can be studied looking for a relationship between the energy and momentum of the electrons in a given material, *i.e.*, trying to find a dispersion relation. In graphene systems, like bilayer graphene, it is possible to derive their electronic band structure through two different approaches. The first is the density functional theory [14] (DFT) and the second is the tight-binding model. The last approach turns out to be more simple and will be briefly described below for bilayer graphene in the way addressed by McCann and Koshino [19].

The general idea of the tight-binding model is to propose a trial wavefunction constructed from the atomic orbital wavefunctions $\phi_j(\mathbf{k}, \mathbf{r})$ per unit cell, with $\mathbf{k}$ being the wave vector and $\mathbf{r}$ the vector position, in order to find the matrix components of the Hamiltonian H describing the bilayer graphene. Taking into account the $2p_z$ orbitals on the four atomic sites forming the unit cell of bilayer graphene, which are labelled as A1, B1, A2 and B2, the Hamiltonian H for bilayer graphene is given by

$$H = \begin{pmatrix} \varepsilon_{A1} & -\gamma_0 f(\mathbf{k}) & \gamma_4 f(\mathbf{k}) & -\gamma_3 f^*(\mathbf{k}) \\ -\gamma_0 f^*(\mathbf{k}) & \varepsilon_{B1} & \gamma_1 & \gamma_4 f(\mathbf{k}) \\ \gamma_4 f^*(\mathbf{k}) & \gamma_1 & \varepsilon_{A2} & -\gamma_0 f(\mathbf{k}) \\ -\gamma_3 f(\mathbf{k}) & \gamma_4 f^*(\mathbf{k}) & -\gamma_0 f^*(\mathbf{k}) & \varepsilon_{B2} \end{pmatrix}, \tag{2.4}$$

where its matrix elements are defined by $H_{jk} = \langle \phi_j | H | \phi_k \rangle$ and the function $f(\mathbf{k})$ describes the in-plane hopping. As in monolayer graphene, the parameter γ_0 describes the nearest neighbour hopping within a single layer. The parameter γ_1 describes the coupling between the pairs of orbitals on the atoms $B1$-$A2$, γ_3 describes the interlayer coupling between the orbitals of the atoms $A1$-$B2$, and γ_4 describes the interaction between atom orbitals $A1$-$A2$ or $B1$-$B2$[1].

According to this model, there are four energy bands in bilayer graphene corresponding to the $2p_z$-orbitals on each of the four atoms in the unit cell. Moreover, at low energies ($|E| \leq \gamma_1$) these bands are obtained by solving the eigenvalue equation $H\psi = E\psi$, with H being the Hamiltonian (2.4). As mentioned before, the low-energy excitations in bilayer graphene arise around the points K and K'. Thus, in the following discussion we will pay attention to this relevant region.

Effective Hamiltonian around the K points

In order to describe the properties of low energies electrons in bilayer graphene around the K-points, a momentum around these points must be defined as follows

$$\mathbf{p} = \hbar(\mathbf{k} - \mathbf{K}). \tag{2.5}$$

Therefore, by expanding in powers of the momentum the function $f(\mathbf{k})$ becomes approximately $f(\mathbf{k}) \approx -\sqrt{3}a(p_x - ip_y)/2\hbar$. Defining $\pi := p_x + ip_y$, $\pi^\dagger := p_x - ip_y$, the Hamiltonian of equation (2.4) is reduced to

$$H = \begin{pmatrix} \varepsilon_{A1} & v_0\pi^\dagger & -v_4\pi^\dagger & v_3\pi \\ v_0\pi & \varepsilon_{B1} & \gamma_1 & -v_4\pi^\dagger \\ -v_4\pi & \gamma_1 & \varepsilon_{A2} & v_0\pi^\dagger \\ v_3\pi^\dagger & -v_4\pi & v_0\pi & \varepsilon_{B2} \end{pmatrix}, \tag{2.6}$$

where $v_j = \sqrt{3}a\gamma_j/2\hbar$, $j = 0,3,4$ are the effective velocities. In order to obtain an analytical solution for the energy bands, the matrix elements containing the hopping parameters γ_3 and γ_4 will be made equal to zero, thus the expressions for the four energy bands become [20]:

$$E_\pm^l = \pm\frac{1}{2}\gamma_1\left(1 - \sqrt{1 + 4\frac{v_0^2|\mathbf{p}|^2}{\gamma_1^2}}\right), \tag{2.7}$$

$$E_\pm^h = \pm\frac{1}{2}\gamma_1\left(1 + \sqrt{1 + 4\frac{v_0^2|\mathbf{p}|^2}{\gamma_1^2}}\right), \tag{2.8}$$

where $|\mathbf{p}| = \left(p_x^2 + p_y^2\right)^{1/2}$. The energies $E_\pm^l$ represent the low-energy bands related to the orbitals on the non-dimer sites $A1$, $B2$ while the energies $E_\pm^h$ correspond to the high-energy bands resulting of the strong interlayer coupling between the atoms $A2$, $B1$ on the dimer sites. These bands can be plotted in reciprocal space (see figure 2.4), where it can be seen that at zero energy around the K points the two low-energy bands touch to each other, whereas the high-energy bands are split away by an energy of the order of $\gamma_1 \approx 0.4$eV.

[1] The values of the parameters γ_j, $j = 0,1,3,4$ are: $\gamma_0 = 3.16$eV, $\gamma_1 = 0.381$eV, $\gamma_3 = 0.38$eV, $\gamma_4 = 0.14$eV [19].

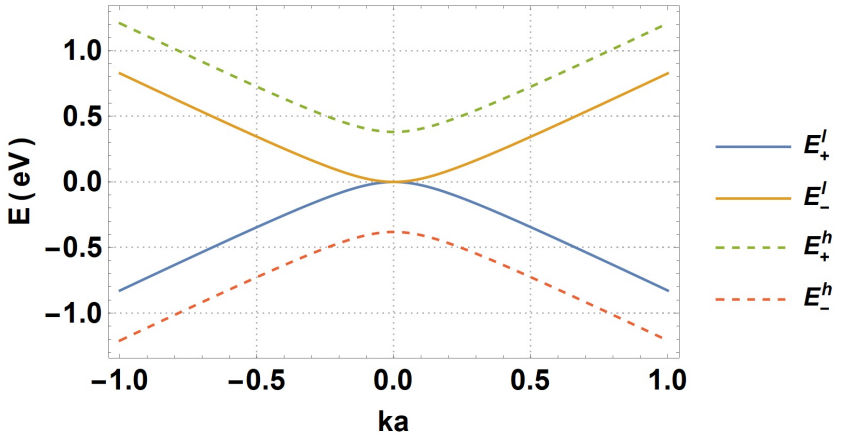

Figure 2.4: Low-energy bands for the bilayer graphene in the reciprocal space around a K-point

Note that for large momentum the bilayer graphene has a linear dispersion relation $E_\pm^l \approx v_0|\mathbf{p}|$ while for small momentum the low energy bands can be approximated by a quadratic dispersion relation $E_\pm^l \approx |\mathbf{p}|^2/2m^*$, with $m^* = \gamma_1/2v_0^2$ being an effective mass.

Then, at low energies it is possible to derive an effective two-band Hamiltonian describing the orbitals on the non-dimer sites $A1$, $B2$, by dropping the components in the Hamiltonian (2.6) related to the orbitals on the dimer sites $A1$, $B2$. The general procedure is explained in [19] and applied to bilayer graphene. Thus, an effective Hamiltonian is obtained as an expansion leading to several terms; however, at low energies $|E| \ll \gamma_1$ the only relevant term is

$$H_{\text{eff}} = \frac{1}{2m^*}\begin{pmatrix} 0 & (\pi^\dagger)^2 \\ (\pi)^2 & 0 \end{pmatrix}, \tag{2.9}$$

where $\pi = p_x + ip_y$, $\pi^\dagger = p_x - ip_y$. The solutions to this Hamiltonian are massive chiral electrons with a quadratic dispersion. It is interesting to note its similarity with the Dirac-like Hamiltonian of monolayer graphene H_{MG} given by

$$H_{\text{MG}} = v_0\begin{pmatrix} 0 & \pi^\dagger \\ \pi & 0 \end{pmatrix}, \tag{2.10}$$

thus, while in H_{MG} the terms of its anti-diagonal are linear, for the bilayer graphene the terms are quadratic in the π-momentum. The reason for this difference lies in the fact that the effective jump between non-dimer atoms $A1$ and $B2$ is carried out via the dimer sites, *i.e.*, through the atoms $B1$ and $A2$.

2.3 Interaction with a magnetic field

A common approach to describe the band structure of metals and semiconductors consists of studying its Landau levels through magneto-optics or magneto-transport measurements [14]. For a conventional

two-dimensional semiconductor, the Landau levels are given by

$$E_n = \hbar\omega_c\left(n+\frac{1}{2}\right), \qquad n = 0,1,2,\ldots \tag{2.11}$$

where $\omega_c = eB/mc$ is the cyclotron frequency for massive charge particles with a quadratic dispersion relation. Since the electron density is changed, there is a step in the Hall conductivity when a Landau level crosses the Fermi level.

The experimental study of monolayer graphene interacting with magnetic fields has attracted the interest in many branches of physics due to its interesting features. One of these is the discovering of the anomalous (half-integer) quantum Hall effect, which has been used to demonstrate and explain the chiral nature of the Dirac-like massless quasiparticles with a linear dispersion relation in monolayer graphene [5].

The problem of monolayer graphene placed in a magnetic field was studied in detail in several works [1, 4] were its energy spectrum was derived. In particular, for a constant homogeneous magnetic field which is orthogonal to the monolayer surface, the vector potential in the Landau gauge can be chosen as $\mathbf{A} = (0, B_0 x, 0)$, obtaining the corresponding Landau levels in monolayer graphene as

$$E_n = \pm\hbar\omega_c\sqrt{n}, \qquad n = 0,1,2,\ldots, \tag{2.12}$$

where $\omega_c = \sqrt{2}v_0/\ell_B$ is the cyclotron frequency, with $[\mathrm{s}]^{-1}$ dimensions and $\ell_B = \sqrt{c\hbar/eB}$ is the magnetic length. Moreover, this problem was addressed in [7] by considering different magnetic field profiles, thus obtaining its energy spectrum and eigenfunctions by using supersymmetry techniques.

2.3.1 Landau levels in bilayer graphene

This work will consider the bilayer graphene placed in a constant homogeneous magnetic field perpendicular to the bilayer surface ($\mathbf{B} = B_0\hat{e}_z$). According to the minimal coupling rule [2], where the momentum $\mathbf{p}$ is replaced by $\mathbf{p} - \frac{q}{c}\mathbf{A}$, the interaction of the bilayer graphene electrons of charge $q = -e$ and effective mass m^* with the field is described by Hamiltonian (2.9), namely,

$$H_{\text{eff}} = \frac{1}{2m^*}\begin{pmatrix} 0 & \left[(p_x+\frac{e}{c}A_x) - i(p_y+\frac{e}{c}A_y)\right]^2 \\ \left[(p_x+\frac{e}{c}A_x) + i(p_y+\frac{e}{c}A_y)\right]^2 & 0 \end{pmatrix}. \tag{2.13}$$

The vector potential is $\mathbf{A} = B_0 x\hat{e}_y$ in the Landau gauge, such that $\mathbf{B} = \nabla\times\mathbf{A} = B_0\hat{e}_z$; therefore, the above Hamiltonian becomes

$$H_{\text{eff}} = \frac{1}{2m^*}\begin{pmatrix} 0 & \left[p_x - i(p_y+\frac{eB_0}{c}x)\right]^2 \\ \left[p_x + i(p_y+\frac{eB_0}{c}x)\right]^2 & 0 \end{pmatrix}. \tag{2.14}$$

It is convenient to introduce the following scalar operators, which naturally appear in equation (2.14):

$$A^{\pm} := \sqrt{\frac{c}{2\hbar eB_0}}\left[p_x \pm i\left(p_y+\frac{eB_0}{c}x\right)\right], \qquad N := A^+A^-, \tag{2.15}$$

such that $A^- = (A^+)^\dagger$. They satisfy the following commutation relations:

$$[A^-, A^+] = I, \qquad [N, A^\pm] = \pm A^\pm, \tag{2.16}$$

where I is the identity operator. Therefore, the operator set $\{A^\pm, N, I\}$ generates the well-known Heisenberg (or boson) algebra, with N being the corresponding number operator.

By defining the new coordinate $\xi := \sqrt{\frac{\omega}{2}}\left(x + \frac{2k}{\omega}\right)$, where $\omega = 2eB_0/c\hbar$ is a constant with dimensions of $[\text{length}]^{-2}$, the operators $A^\pm$ can be rewritten as follows

$$A^\pm = \pm\frac{i}{\sqrt{2}}\left(\xi \mp \frac{d}{d\xi}\right). \tag{2.17}$$

Therefore, the time-independent Dirac-type equation for the H_{eff} in equation (2.14) becomes

$$H_{\text{eff}}\Psi(\xi, y) = \hbar\omega_c^* \begin{pmatrix} 0 & (A^-)^2 \\ (A^+)^2 & 0 \end{pmatrix} \Psi(\xi, y) = E\Psi(\xi, y), \tag{2.18}$$

where $\omega_c^* = eB_0/m^*c$ is the cyclotron frequency for non-relativistic electrons with effective mass m^*.

Taking into account the translational invariance along y-direction, the two-component spinor is proposed as

$$\Psi(\xi, y) = \exp(iky) \begin{pmatrix} \psi^+(\xi) \\ \psi^-(\xi) \end{pmatrix}, \tag{2.19}$$

where k is the wave number in y-direction and $\psi^\pm(\xi)$ describes the electron amplitudes associated to the A1 and B2 sites respectively. Then, equation (2.18) yields the next two coupled equations:

$$(A^+)^2\psi^+(\xi) = \varepsilon\,\psi^-(\xi), \tag{2.20}$$

$$(A^-)^2\psi^-(\xi) = \varepsilon\,\psi^+(\xi), \tag{2.21}$$

where $\varepsilon := E/\hbar\omega_c^*$. To decouple the previous system, let us calculate $H_{\text{eff}}^2\Psi(\xi, y) = E^2\Psi(\xi, y)$ so that

$$H_+\psi^+(\xi) = \varepsilon^2\,\psi^+(\xi), \qquad H_+ := (A^-)^2(A^+)^2, \tag{2.22}$$

$$H_-\psi^-(\xi) = \varepsilon^2\,\psi^-(\xi), \qquad H_- := (A^+)^2(A^-)^2. \tag{2.23}$$

Note that, equations (2.20)–(2.23) represent an example of a pair of supersymmetric partner Hamiltonians H_+ and H_-, which are connected by the second order intertwining operators $(A^\pm)^2$. Furthermore, since $[A^-, A^+] = I$ it is possible to express the scalar Hamiltonians H_+ and H_- in terms of the number operator N as follows

$$H_+ = (N+2)(N+I), \qquad H_- = N(N-I). \tag{2.24}$$

In a similar way as for the harmonic oscillator, operators $A^\pm$ satisfy equation (2.16) and are considered creation and annihilation operators. Moreover, since N and $H_\pm$ commute, it is possible to look for simultaneous eigenfunctions of all of them. Thus, we can say that these states have a boson number of excitations n determined by the eigenvalues of N.

If in equations (2.22)-(2.23) we take

$$\psi^{+}(\xi) := \psi_{n-2}(\xi), \quad \psi^{-}(\xi) := \psi_{n}(\xi), \tag{2.25}$$

with $\psi_n(\xi) = \langle \xi | n \rangle$ being the eigenfunctions of the shifted harmonic oscillator Hamiltonian, and use equation (2.24), it is obtained that $\varepsilon^2 = n(n-1)$. Therefore, the eigenvalues of the Hamiltonian H_{eff} in equation (2.14) become

$$E_n^{\pm} = \pm\hbar\omega_c^* \sqrt{n(n-1)}, \qquad n = 0,1,2,\ldots, \tag{2.26}$$

where the plus (minus) sign characterizes the energy of electrons (holes).

On the other hand, the ground state eigenfunction $\psi_0(\xi)$ is characterized by

$$A^{-}\psi_0(\xi) = 0. \tag{2.27}$$

It is possible to obtain the excited states eigenfunctions by applying n-times the creation operator A^{+}:

$$\psi_n(\xi) = \frac{1}{\sqrt{n!}}(A^{+})^n \psi_0(\xi). \tag{2.28}$$

After some calculations, and returning to the x variable, it is found that the normalized eigenfunctions $\psi_n(x)$, for $n = 0,1,2,\ldots$ turn out to be

$$\psi_n(x) = \sqrt{\frac{1}{2^n n!}\left(\frac{\omega}{2\pi}\right)^{1/2}} H_n\left[\sqrt{\frac{\omega}{2}}\left(x + \frac{2k}{\omega}\right)\right] \exp\left(-\frac{\omega}{4}\left(x+\frac{2k}{\omega}\right)^2\right), \ \omega = \frac{2m^*}{\hbar}\omega_c^*. \tag{2.29}$$

Therefore, the Landau states $\Psi_n(x,y)$ will be written in the form (see [21]):

$$\Psi_n^{\pm}(x,y) = \frac{\exp(iky)}{\sqrt{2^{(1-\delta_{n0}-\delta_{n1})}}} \begin{pmatrix} (1-\delta_{n0}-\delta_{n1})\,\psi_{n-2}(x) \\ \pm\psi_n(x) \end{pmatrix}, \quad n = 0,1,\ldots \tag{2.30}$$

We should note that $E_0^{\pm} = E_1^{\pm} = 0$, *i.e.*, the ground state energy has a fourfold degeneracy (a double degeneracy due to electrons and the same degeneracy due the holes). On the other hand, the levels $E_n^{\pm}$ for $n \geq 2$ are non-degenerate.

2.3.2 Probability and current densities for the Landau states in bilayer graphene

Probability density

The probability density $\rho(\mathbf{r})$ is defined in the usual way and for the Landau states $\Psi_n^{\pm}(x,y)$ it will be denoted as $\rho_n(x)$, which in the present case can be written in compact form as follows

$$\rho_n(x) = \left(\Psi_n^{\pm}(x,y)\right)^{\dagger}\Psi_n^{\pm}(x,y) = \frac{(1-\delta_{n0}-\delta_{n1})|\psi_{n-2}(x)|^2 + |\psi_n(x)|^2}{2^{(1-\delta_{n0}-\delta_{n1})}}, \quad n = 0,1,2,\ldots \tag{2.31}$$

Note that, although the wave function $\Psi_n^{\pm}(x,y)$ depends explicitly on x and y, the associated probability density is independent of y due to the translation symmetry along this direction; in addition, it will be time-independent for stationary states. Figure 2.5 shows the probability density of equation (2.31) for several Landau states.

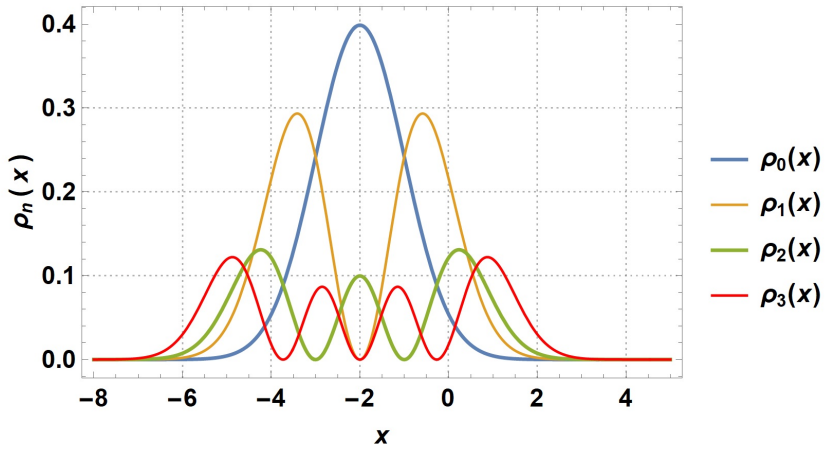

Figure 2.5: Probability density $\rho_n(x)$ for the first four Landau states $\Psi_n^{\pm}(x,y)$ in bilayer graphene.

Current density

Concerning the current density **J** for electrons in bilayer graphene, the appropriate expression in the free case ($B_0 = 0$) was derived in [23], obtaining that the components J_k of such a current take the form

$$J_k[\Psi] = \frac{\hbar}{m^*}\,\mathrm{Im}\left(\Psi^\dagger\, j_k\,\Psi\right). \tag{2.32}$$

In the case of Cartesian coordinates, *i.e.*, for $k = x, y$, the current density operators (j_x, j_y) are given by

$$j_x = \frac{i}{\hbar}\begin{pmatrix} 0 & p^- \\ p^+ & 0 \end{pmatrix}, \qquad j_y = \frac{1}{\hbar}\begin{pmatrix} 0 & p^- \\ -p^+ & 0 \end{pmatrix}, \qquad p^\pm = p_x \pm i p_y. \tag{2.33}$$

The previous expressions for the current density operators are no longer valid for the bilayer Hamiltonian (2.14) for the case when there is a constant magnetic field perpendicular to the bilayer graphene surface, $\mathbf{B} = B_0\hat{e}_z$, described by a potential in the Landau gauge. Thus, we must consider that

$$\frac{\partial \rho}{\partial t} + \frac{i}{\hbar}\left[\Psi^\dagger\left(H_{\mathrm{eff}}\Psi\right) - \left(H_{\mathrm{eff}}\Psi\right)^\dagger\Psi\right] = 0. \tag{2.34}$$

After a somewhat long calculation it is possible to arrive at a continuity equation,

$$\frac{\partial J_x}{\partial x} + \frac{\partial J_y}{\partial y} + \frac{\partial \rho}{\partial t} = 0, \tag{2.35}$$

where the correct expression for j_x, j_y in equation (2.32) is

$$j_x = \frac{i}{\hbar}\begin{pmatrix} 0 & \pi^- \\ \pi^+ & 0 \end{pmatrix}, \qquad j_y = \frac{1}{\hbar}\begin{pmatrix} 0 & \pi^- \\ -\pi^+ & 0 \end{pmatrix}, \tag{2.36}$$

i.e., the momentum operators $p^\pm$ in equation (2.33) for the free case must be replaced, according to the minimal coupling rule, as follows:

$$p^- \to \pi^- = p^- - \frac{ieB_0}{c}x, \qquad p^+ \to \pi^+ = p^+ + \frac{ieB_0}{c}x. \tag{2.37}$$

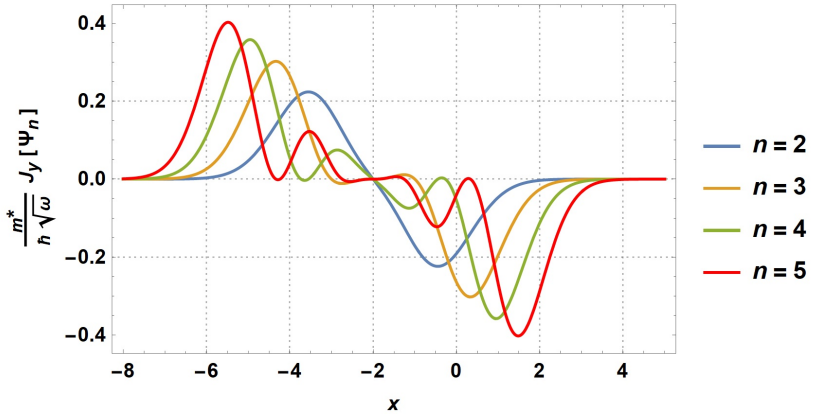

Figure 2.6: Current density $J_y[\Psi_n^+]$ for some Landau states in bilayer graphene.

Thus, the current density for bilayer graphene is gauge invariant.

Let $\theta^\pm$ be the creation and annihilation operators for the functions $\psi_n(x)$ defined as follows

$$\theta^\pm := \frac{1}{\sqrt{2}}\left(\xi \mp \frac{d}{d\xi}\right), \tag{2.38}$$

such that $\theta^\pm = \mp iA^\pm$. Thus, the action onto the states $\psi_n(x)$ is given by

$$\theta^- \psi_n = \sqrt{n}\psi_{n-1},$$

$$\theta^+ \psi_n = \sqrt{n+1}\psi_{n+1}. \tag{2.39}$$

Thus, the current density operators (j_x, j_y) can be rewritten as follows:

$$j_x = \sqrt{\omega}\begin{pmatrix} 0 & \theta^- \\ -\theta^+ & 0 \end{pmatrix}, \qquad j_y = -i\sqrt{\omega}\begin{pmatrix} 0 & \theta^- \\ \theta^+ & 0 \end{pmatrix}. \tag{2.40}$$

Therefore, by applying these operators onto the states $\Psi_n^\pm(x,y)$ the components of the current density can be obtained as follows

$$J_x[\Psi_n^\pm(x,y)] = \pm\frac{\hbar\sqrt{\omega}}{m^*}\frac{(1-\delta_{n0}-\delta_{n1})}{2^{(1-\delta_{n0}-\delta_{n1})}}\mathrm{Im}\left[\sqrt{n}\psi_{n-2}^*(x)\psi_{n-1}(x) + \sqrt{n-1}\psi_n^*(x)\psi_{n-1}(x)\right], \tag{2.41}$$

$$J_y[\Psi_n^\pm(x,y)] = \mp\frac{\hbar\sqrt{\omega}}{m^*}\frac{(1-\delta_{n0}-\delta_{n1})}{2^{(1-\delta_{n0}-\delta_{n1})}}\mathrm{Im}\left[i\left(\sqrt{n}\psi_{n-2}^*(x)\psi_{n-1}(x) + \sqrt{n-1}\psi_n^*(x)\psi_{n-1}(x)\right)\right]. \tag{2.42}$$

Note that the functions $\psi_n(x)$ defined in equation (2.29) are real, such that $\psi_n(x) = \psi_n^*(x)$. Thus, according to equation (2.32) the x-component of the current density for bilayer graphene given in equation (2.41) always disappear for all n, while the y-component in equation (2.42) remains non-null for the Landau states with $n \geq 2$ and only depends on x, *i.e.*,

$$J_x[\Psi_n^\pm] = 0 \quad \forall\ n, \qquad\qquad J_y[\Psi_n^\pm] \neq 0, \quad n \geq 2. \tag{2.43}$$

Figure 2.6 shows the current density (2.42) in y-direction for some Landau states $\Psi_n^+(x,y)$.

Chapter 3

Coherent states

In 1900, Max Planck introduced for the first time the concept of quantization to explain black-body radiation [27]. The revolutionary idea that the exchange of energy between radiation and matter takes place in a discrete way, through quantum units of energy, was the first breakthrough that gave rise to quantum mechanics, a probabilistic and indeterministic theory describing the microscopic world [27]. Since then, quantum mechanics has become the basis of modern physics and has been used in different branches, giving place to many theoretical and technological developments.

Nevertheless, the efforts to establish a connection between quantum and classical theories continue, and they have contributed to the emergence of different semi-classical approaches. One of them is the so-called coherent states (CS), which were proposed by Erwin Schrödinger in 1926 for the harmonic oscillator [28] as quantum states that minimize the Heisenberg uncertainty relation, such that they mimic their classical counterparts through the time evolution of the expected values of the position and momentum operators [29, 36].

One of the most successful applications of CS happened in the early 1960s, when Glauber, Klauder and Sudarshan used them to describe coherent electromagnetic radiation [30–35], giving place to a new area in physics called nowadays quantum optics. The CS can be generalized, *i.e.*, defined appropriately in order to describe other systems in different areas of physics, as condensed matter, particle, nuclear and atomic physics, among others [24–26, 29]. In this way, the generalized coherent states $|z\rangle$ can be defined as follows [29]:

- They are eigenvectors of an annihilation operator a with complex eigenvalue z:

$$a|z\rangle = z|z\rangle, \qquad z \in \mathbb{C}. \tag{3.1}$$

  Note that, the CS defined in this way are generally referred to as Barut-Girardello coherent states [37, 38], and it is precisely this definition that will be used along this work.

- They are obtained from the ground state of the system $|0\rangle$ by acting an unitary operator, defined by $D(z) := \exp\left[\frac{1}{\sqrt{\hbar}}\left(za^\dagger - z^* a\right)\right]$. Thus:

$$|z\rangle = D(z)|0\rangle = \exp\left[\frac{1}{\sqrt{\hbar}}\left(za^\dagger - z^* a\right)\right]|0\rangle. \tag{3.2}$$

$D(z)$ is called the displacement operator, thus the above equation means that the CS $|z\rangle$ is just a displaced version of the fundamental state $|0\rangle$ of the system. This generalization was pushed forward by Gilmore and Perelemov [39, 40].

- They minimize the Heisenberg inequality

$$\langle \Delta Q\rangle \langle \Delta P\rangle = \frac{1}{2}\hbar, \tag{3.3}$$

where $\langle \Delta B\rangle := \left[\langle z|B^2|z\rangle - \langle z|B|z\rangle\right]^{1/2}$. Thus, the CS are quantum states with minimal uncertainty, such that they evolve following the classical trajectories of the harmonic oscillator, which was the original motivation of Schrödinger for proposing such states.

These CS definitions are equivalent for the harmonic oscillator and they are called canonical coherent states. So, in general for a system whose Hamiltonian is linear in the operators $\{a, a^\dagger, N, I\}$, if the initial state $(t = 0)$ is a coherent state then the evolved state will be also a coherent state which will follow the classical trajectory. Since the mean square deviations ΔQ and ΔP are equal and constant, the wave packet will not be deformed along such evolution. These are the reasons for the CS to be sometimes called also quasi-classical states, since they supply a natural framework to analyze the connection between quantum and classical mechanics [29, 36].

3.1 Bilayer graphene coherent states

Bilayer graphene in a static magnetic field has been described in the above chapter, and in the standard approach this problem can be solved exactly for a constant homogeneous magnetic filed, leading to the Landau levels and the associated eigenfunctions, which are different from the monolayer graphene ones.

With this in mind, it seems natural to explore the possibility of generating the bilayer graphene coherent states (BGCS). This alternative semi-classical approach was implemented in [50], where they were built as eigenstates of an appropriate annihilation operator. We briefly describe the construction of these states in the remainder of this chapter.

3.1.1 Annihilation and creation operators

First of all, it is necessary to determine an appropriate annihilation operator $\mathbf{A}^-$ for the Hamiltonian (2.14), which can be proposed as follows

$$\mathbf{A}^- := \begin{pmatrix} f_3(N)\theta^- & 0 \\ 0 & f(N+I)\theta^- \end{pmatrix}, \tag{3.4}$$

where the operators $\theta^\pm$ are given in equation (2.38), and f, f_3 are two auxiliary real functions.

Note that

$$\mathbf{A}^-\Psi_n^\pm(x,y) = \frac{\exp(iky)}{\sqrt{2}} \begin{pmatrix} \sqrt{n-2}\, f_3(n-3)\, \psi_{n-3}(x) \\ \pm\sqrt{n}\, f(n)\, \psi_{n-1}(x) \end{pmatrix}. \tag{3.5}$$

In order to ensure that $\mathbf{A}^-\Psi_n^\pm(x,y) = c_n\Psi_{n-1}^\pm(x,y)$, the functions f, f_3 must fulfill

$$\sqrt{n-2} f_3(n-3) = \sqrt{n} f(n) =: c_n. \tag{3.6}$$

Thus, the explicit expression for the annihilation operator $\mathbf{A}^-$ becomes

$$\mathbf{A}^- = \begin{pmatrix} \frac{\sqrt{N+3I}}{\sqrt{N+I}} f(N+3I)\theta^- & 0 \\ 0 & f(N+I)\theta^- \end{pmatrix}. \tag{3.7}$$

Meanwhile, the creation operator $\mathbf{A}^+$ is just the Hermitian conjugate of $\mathbf{A}^-$, *i.e.*,

$$\mathbf{A}^+ = \begin{pmatrix} \theta^+ \frac{\sqrt{N+3I}}{\sqrt{N+I}} f(N+3I) & 0 \\ 0 & \theta^+ f(N+I) \end{pmatrix}, \tag{3.8}$$

such that

$$\begin{aligned} \mathbf{A}^+\Psi_0^\pm(x,y) =& f(1)\Psi_1^\pm(x,y), \\ \mathbf{A}^+\Psi_1^\pm(x,y) =& \sqrt{2}f(2)\exp(iky)\begin{pmatrix} 0 \\ \pm\psi_2(x) \end{pmatrix}, \\ \mathbf{A}^+\Psi_n^\pm(x,y) =& \sqrt{n+1}f(n+1)\Psi_{n+1}^\pm(x,y), \quad n=2,3,\ldots \end{aligned} \tag{3.9}$$

3.1.2 Barut-Girardello coherent states

As mentioned before, the bilayer graphene CS can be constructed as eigenstates $\Psi_\alpha(x,y)$ of the annihilation operator $\mathbf{A}^-$ of equation (3.7) with complex eigenvalue α, namely,

$$\mathbf{A}^-\Psi_\alpha(x,y) = \alpha\Psi_\alpha(x,y), \qquad \alpha \in \mathbb{C}. \tag{3.10}$$

By expressing now the states $\Psi_\alpha(x,y)$ as a linear combination of the eigenstates with positive energy $\Psi_n^+(x,y)$ in equation (2.30),

$$\Psi_\alpha(x,y) = \sum_{n=0}^{\infty} a_n\Psi_n^+(x,y) = \exp(iky)\left[a_0\begin{pmatrix} 0 \\ \psi_0(x) \end{pmatrix} + a_1\begin{pmatrix} 0 \\ \psi_1(x) \end{pmatrix} + \sum_{n=2}^{\infty}\frac{a_n}{\sqrt{2}}\begin{pmatrix} \psi_{n-2}(x) \\ \psi_n(x) \end{pmatrix}\right], \tag{3.11}$$

and substituting this expression in (3.10) we obtain a recurrence relationship for the coefficients a_n,

$$\begin{aligned} a_1 =& \frac{\alpha a_0}{f(1)}, \\ a_2 =& \frac{\alpha a_1}{f(2)}, \\ a_{n+1} =& \frac{\alpha}{\sqrt{n+1}f(n+1)}a_n, \quad n=2,3,\ldots \end{aligned} \tag{3.12}$$

Three different cases can be identified.

1. Coherent states when $f(1)\neq 0$ and $f(2)\neq 0$

Suppose that $f(n)\neq 0 \ \forall n\in\mathbb{N}$, so that the coefficients a_n become

$$a_n = \frac{\sqrt{2}\alpha^n}{\sqrt{n!\,[f(n)]!}}a_0, \qquad n=2,3,\ldots \tag{3.13}$$

where, for any function $q(s)$ such that $s \in \mathbb{N}$, the generalized factorial function is defined by

$$[q(s)]! := \begin{cases} 1 & \text{for} \quad s = 0, \\ q(1)\cdots q(s) & \text{for} \quad s > 0. \end{cases} \tag{3.14}$$

Thus, the Barut-Girardello coherent states in this case are

$$\begin{aligned} \Psi_\alpha(x,y) = &\left[1 + \frac{|\alpha|^2}{f(1)^2} + 2\sum_{n=2}^{\infty} \frac{|\alpha|^{2n}}{n!\,([f(n)]!)^2}\right]^{-\frac{1}{2}} \\ &\times \left[\Psi_0^+(x,y) + \frac{\alpha}{f(1)}\Psi_1^+(x,y) + \sqrt{2}\sum_{n=2}^{\infty} \frac{\alpha^n}{\sqrt{n!}\,[f(n)]!}\Psi_n^+(x,y)\right]. \end{aligned} \tag{3.15}$$

Note that the states (3.15) were normalized using the free coefficient a_0.

2. Coherent states when $f(1) = 0$ and $f(2) \neq 0$

If $f(2) \neq 0$ the free parameter becomes a_1. The recurrence relationship for the coefficients a_n is now

$$a_{n+1} = \frac{\sqrt{2}\alpha^n}{\sqrt{(n+1)!\,[g(n)]!}} a_1, \;\; n = 1,2,\ldots \tag{3.16}$$

where $g(n) := f(n+1)$. Substituting this result in equation (3.11), the normalized coherent states are

$$\Psi_\alpha(x,y) = \left[1 + 2\sum_{n=1}^{\infty} \frac{|\alpha|^{2n}}{(n+1)!\,([g(n)]!)^2}\right]^{-\frac{1}{2}} \left[\Psi_1^+(x,y) + \sqrt{2}\sum_{n=1}^{\infty} \frac{\alpha^n}{\sqrt{(n+1)!\,[g(n)]!}}\Psi_{n+1}^+(x,y)\right]. \tag{3.17}$$

3. Coherent states when $f(1) = 0$ and $f(2) = 0$

On the other hand, if $f(2) = 0$ it must happen that $a_1 = 0$ so that a_2 is now the free parameter. By defining $h(n) := f(n+2)\ \forall\ n \in \mathbb{N}$, the normalized coherent states turn out to be

$$\Psi_\alpha(x,y) = \left[\sum_{n=0}^{\infty} \frac{|\alpha|^{2n}}{(n+2)!\,([h(n)]!)^2}\right]^{-\frac{1}{2}} \sum_{n=0}^{\infty} \frac{\alpha^{n-2}}{\sqrt{(n+2)!\,[h(n)]!}}\Psi_{n+2}^+(x,y). \tag{3.18}$$

Equations (3.15), (3.17) and (3.18) contain three different sets of BGCS, all of them depending on the particular choice of the function $f(n)$. Note that these BGCS look similar to the monolayer graphene coherent states (MGCS) derived in [22].

Several physical quantities, as the Heisenberg uncertainty relation, probability and current densities as well as mean energy value were computed an analyzed in detail for these families of BGCS in [50]. In this work we will just describe the time evolution of such states.

3.2 Time evolution

Wave packet dynamics has been explored since the early days of quantum mechanics, and then explored in several areas in physics and chemistry [52]. Starting from Schrödinger and his derivation of the CS for the harmonic oscillator, up to the development of experimental techniques in atomic physics using Rydberg atoms [53, 54], the studies on the connection between the quantum and classical descriptions of nature through time evolving wave packets have attracted the interest of the scientific community.

This research can be come quite complex due to quantum interference; however, several types of periodicity can arise depending on the structure of the energy spectrum [55]. In particular, it is well known that the time stability of the canonical coherent states comes from the fact that the energy levels of the harmonic oscillator are equally spaced [46]. In general, this stability does not arise for quantum systems without equally spaced energy levels [47–49].

In this section, we describe the time evolution of the BGCS. In general, the evolution of a quantum state is obtained by acting the unitary time evolution operator $U(t,t_0)$ as follows [27]:

$$|\Psi(t)\rangle = U(t,t_0)|\Psi(t_0)\rangle, \qquad t > t_0. \tag{3.19}$$

In particular, for time-independent Hamiltonians the evolution operator has the simple form $U(t,t_0) = \exp\left[-\frac{i}{\hbar}(t-t_0)H\right]$; therefore, the evolved quantum state is given by

$$|\Psi(t)\rangle = \exp\left[-\frac{i}{\hbar}(t-t_0)\,H\right]|\Psi(t_0)\rangle. \tag{3.20}$$

3.2.1 Evolution of bilayer graphene coherent states

As mentioned before, the three sets of BGCS derived in equations (3.15), (3.17) and (3.18) depend on the particular choice of the function $f(n)$, $g(n)$ or $h(n)$; therefore, in order to compute their time evolution a specific choice of $f(n)$ will be taken for each family of BGCS.

1. Evolution of BGCS when $f(1) \neq 0$ and $f(2) \neq 0$

First of all, let us make the particular choice $f(N) := I$ so that the BGCS of equation (3.15) reduce to

$$\Psi_\alpha(x,y) = \frac{1}{\sqrt{2\exp(\zeta^2)-\zeta^2-1}}\left[\Psi_0^+(x,y) + \alpha\Psi_1^+(x,y) + \sqrt{2}\sum_{n=2}^{\infty}\frac{\alpha^n}{\sqrt{n!}}\Psi_n^+(x,y)\right], \tag{3.21}$$

where $\alpha = \zeta\exp(i\varphi)$. We calculate now their time evolution for $t_0 = 0$ through equation (3.20), leading to

$$\Psi_\alpha(x,y;t) = \frac{1}{\sqrt{2\exp(\zeta^2)-\zeta^2-1}}\left\{\Psi_0^+(x,y) + \alpha\Psi_1^+(x,y) + \sum_{n=2}^{\infty}\frac{\sqrt{2}\alpha^n}{\sqrt{n!}}\exp\left[-i\sqrt{n(n-1)}\,\omega_c^* t\right]\Psi_n^+(x,y)\right\}. \tag{3.22}$$

2. Evolution of BGCS when $f(1)=0$ and $f(2)\neq 0$

Let us choose now $f(N+I):=g(N):=\frac{\sqrt{N}}{\sqrt{N+I}}$, so that $f(n+1)\neq 0\ \forall\ n=1,2,\ldots$. Then, the coherent states of equation (3.17) become

$$\Psi_\alpha(x,y)=\frac{1}{\sqrt{2\exp(\zeta^2)-1}}\left[\Psi_1^+(x,y)+\sqrt{2}\sum_{n=1}^{\infty}\frac{\alpha^n}{\sqrt{n!}}\Psi_{n+1}^+(x,y)\right]. \tag{3.23}$$

For these states the time evolution turns out to be

$$\Psi_\alpha(x,y;t)=\frac{1}{\sqrt{2\exp(\zeta^2)-1}}\left\{\Psi_1^+(x,y)+\sum_{n=2}^{\infty}\frac{\sqrt{2}\alpha^{n-1}}{\sqrt{(n-1)!}}\exp\left[-i\sqrt{n(n-1)}\,\omega_c^* t\right]\Psi_n^+(x,y)\right\}. \tag{3.24}$$

3. Evolution of BGCS when $f(1)=0$ and $f(2)=0$

Finally, let us take $f(N+2)=h(N)=\frac{N\sqrt{N+I}}{\sqrt{N+2}}$, thus the coherent states of equation (3.18) reduces to

$$\Psi_\alpha(x,y)=\frac{1}{\sqrt{{}_0F_2(1,2;\zeta^2)}}\left[\sum_{n=0}^{\infty}\frac{\alpha^n}{n!\sqrt{(n+1)!}}\Psi_{n+2}^+(x,y)\right], \tag{3.25}$$

were ${}_pF_q$ is the generalized hypergeometric function defined by

$${}_pF_q(a_1,\ldots,a_p,b_1\ldots,b_q;x)=\frac{\Gamma(b_1)\cdots\Gamma(b_q)}{\Gamma(a_1)\cdots\Gamma(a_p)}\sum_{n=0}^{\infty}\frac{\Gamma(a_1+n)\cdots\Gamma(a_p+n)}{\Gamma(b_1+n)\cdots\Gamma(b_q+n)}\frac{x^n}{n!}. \tag{3.26}$$

The time evolution for the BGCS of equation (3.25) is

$$\Psi_\alpha(x,y;t)=\frac{1}{\sqrt{{}_0F_2(1,2;\zeta^2)}}\sum_{n=2}^{\infty}\frac{\alpha^{n-2}}{(n-2)!\sqrt{(n-1)!}}\exp\left[-i\sqrt{n(n-1)}\,\omega_c^* t\right]\Psi_n^+(x,y). \tag{3.27}$$

The probability densities for the evolving states (3.22), (3.24) and (3.27) are shown in figures 3.1, 3.2 and 3.3, respectively.

Discussion

As can be seen from equation (2.26), the Landau levels for bilayer graphene are not equidistant. However, starting from a certain integer ($n\gtrsim 2$ approximately) this spectrum is practically lineal, stabilizing in time those BGCS for which the contribution of the eigenstates $\Psi_0^+(x,y)$ and $\Psi_1^+(x,y)$ can be neglected when compared with the contribution of all other eigenstates, *i.e.*, with $|\alpha|\gg 1$. This can be seen clearly in figure 3.3(a), where the BGCS (3.27) are stable in time, with the same period as the auxiliary harmonic oscillator ($\tau\simeq 2\pi/\omega_c^*$). For the other two examples, equations (3.22) and (3.24), the coherent states could involve in a non-trivial way the eigenstates $\Psi_0^+(x,y)$, $\Psi_1^+(x,y)$ or both, thus making their time evolution being in general not stable (see figures 3.1(a) and 3.2(a)).

Despite the first two sets of BGCS of equations (3.22) and (3.24) do not have always the period $2\pi/\omega_c^*$, a way to find a possible approximate period τ for these states was proposed in [50]. First of all. Note that, τ is closely related to the associated mean energy value and to the eigenvalues bounding

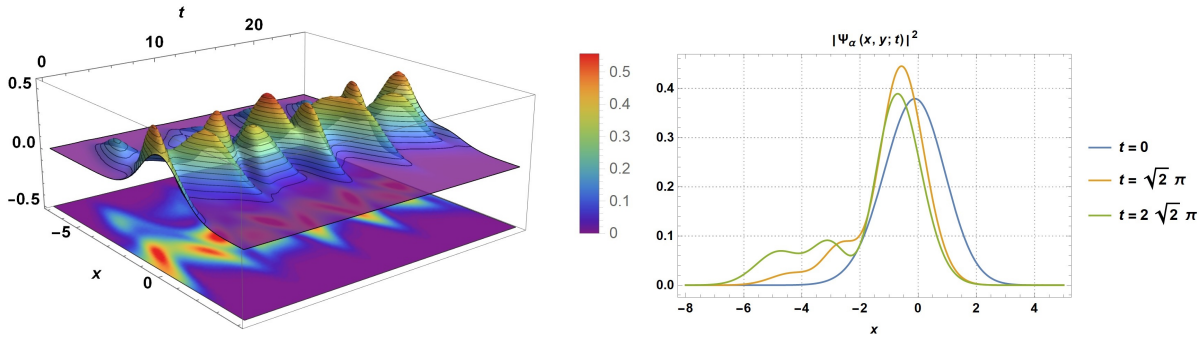

(a) (b)

Figure 3.1: (a) Probability density $|\Psi_\alpha(x,y;t)|^2$ for the BGCS of equation (3.22) with $f(n)=1$, $\zeta=1$, $\varphi=0$ and $\omega_c^*=1$. (b) Probability density $|\Psi_\alpha(x,y;t)|^2$ for some fixed times (the suggested approximate period and some of its multiples). The blue, orange and green lines correspond to $t=\left\{0,\sqrt{2}\pi,2\sqrt{2}\pi\right\}$, respectively.

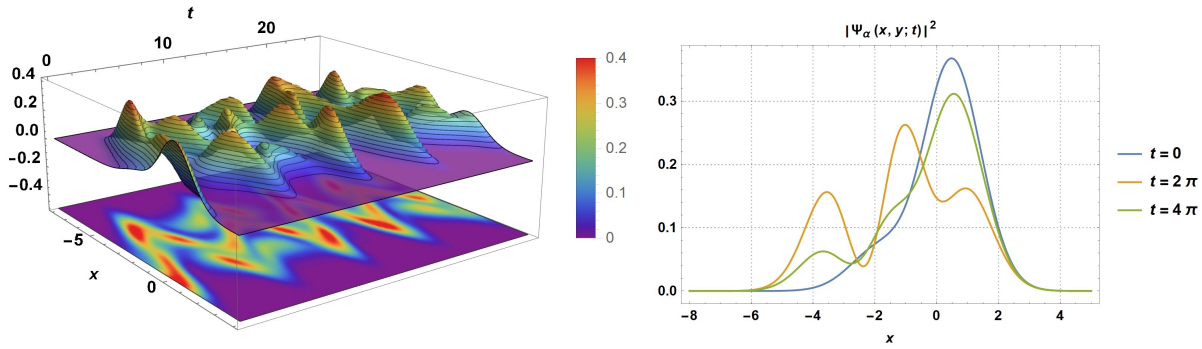

(a) (b)

Figure 3.2: (a) Probability density $|\Psi_\alpha(x,y;t)|^2$ for the BGCS of equation (3.24) with $f(n)=\sqrt{n-1}/\sqrt{n}$, $\zeta=1$, $\varphi=0$ and $\omega_c^*=1$. (b) Probability density $|\Psi_\alpha(x,y;t)|^2$ for some fixed times (the suggested approximate period and some of its multiples). The blue, orange and green lines correspond to $t=\{0,2\pi,4\pi\}$, respectively.

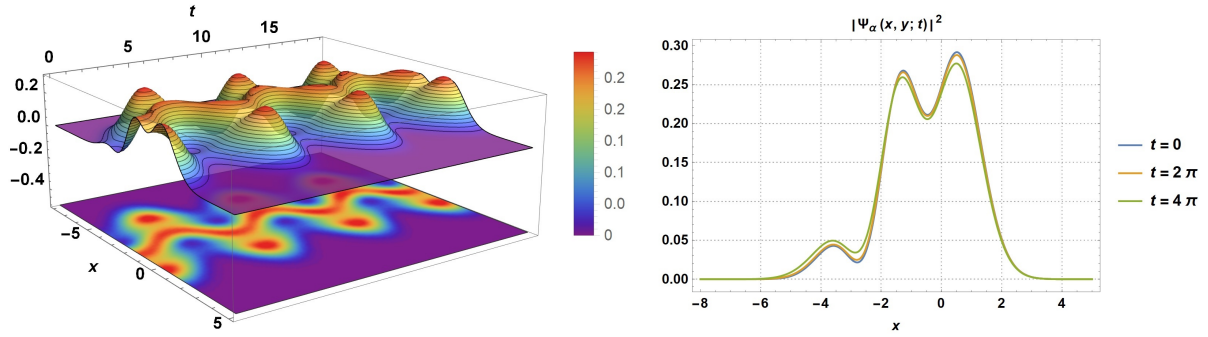

(a) (b)

Figure 3.3: (a) Probability density $|\Psi_\alpha(x,y;t)|^2$ for the BGCS of equation (3.27) with $f(n) = (n-2)\sqrt{n-1}/\sqrt{n}$, $\zeta = 1$, $\varphi = 0$ and $\omega_c^* = 1$. (b) Probability density $|\Psi_\alpha(x,y;t)|^2$ for some fixed times (the suggested approximate period and some of its multiples). The blue, orange and green lines correspond to $t = \{0, 2\pi, 4\pi\}$, respectively.

this average for a given α. Hence, by setting α first $\langle H_{\text{eff}}\rangle_\alpha$ must be calculated, then the interval in which it lies must be determined, bounded by two consecutive proper energies E_{j+1} and E_j, *i.e.*, $E_j < \langle H_{\text{eff}}\rangle_\alpha < E_{j+1}$. Finally, the next expression for the possible approximate period for the time-evolution of the BGCS can be proposed

$$\tau = \frac{2\pi\hbar}{E_{j+1} - E_j}. \tag{3.28}$$

Recall that the quantity $\langle H_{\text{eff}}\rangle_\alpha$ is calculated as:

$$\langle H_{\text{eff}}\rangle_\alpha = \langle \Psi_\alpha(x,y)|H_{\text{eff}}|\Psi_\alpha(x,y)\rangle, \tag{3.29}$$

i.e., it is the mean value of the effective Hamiltonian (2.14) in the states $\Psi_\alpha(x,y)$.

For states (3.22) with $|\alpha| = 1$ (such that $0 < \langle H_{\text{eff}}\rangle_\alpha = 0.76\hbar\omega_c^* < E_2$), we obtain an approximate period $\tau \simeq \sqrt{2}\pi/\omega_c^*$, and for states (3.24) such that $E_2 < \langle H_{\text{eff}}\rangle_\alpha = 1.56\hbar\omega_c^* < E_3$ it is obtained $\tau \simeq 2\pi/\omega_c^*$. In figures 3.1(b) and 3.2(b) we have plotted the probability density at such a τ, and some of its multiples in each case.

3.2.2 Revival structure of bilayer graphene and autocorrelation function

The phenomena of collapse and revival emerge naturally when exploring the wave-packet dynamics of quantum physical systems. This revival structure is relevant for a variety of problems since it allows to study the classical limit of a quantum-mechanical system. There are different types of revival structures and they share the property of exhibiting an initial periodicity followed by a sequence of collapses and subsequent revivals [52, 53, 55].

Time scales

To analyze the possible existence of this phenomenon in bilayer graphene, the so-called time scales can be explored by studying the energy spectrum. First, consider a Taylor series expansion of the energy E_n

in the variable n around the mean value $\overline{n}$:

$$E_n \simeq E_{\overline{n}} + E'_{\overline{n}}(n-\overline{n}) + \frac{1}{2}E''_{\overline{n}}(n-\overline{n})^2 + \frac{1}{6}E'''_{\overline{n}}(n-\overline{n})^3 + \cdots, \tag{3.30}$$

where $E'_{\overline{n}} = (\mathrm{d}E_n/\mathrm{d}n)_{n=\overline{n}}$. Each derivative term in equation (3.30) defines a time scale that depends on the value of $\overline{n}$ as follows [52,53]:

$$T_{\mathrm{cl}} := \frac{2\pi\hbar}{|E'_{\overline{n}}|}, \qquad T_{\mathrm{rev}} := \frac{2\pi\hbar}{\frac{1}{2}|E''_{\overline{n}}|}, \qquad T_{\mathrm{sr}} := \frac{2\pi\hbar}{\frac{1}{6}|E'''_{\overline{n}}|}. \tag{3.31}$$

The first time scale T_{cl} is related with the period of classical motion. The second period T_{rev} is associated with the quantum revival scale, *i.e.*, the time scale in which the probability density almost recovers its initial shape after spreading and collapsing. Finally, the third time scale T_{sr} is called super-revival time.

Therefore, the phase factor $\exp(-iE_nt/\hbar)$ involved in the time evolution of the BGCS can be expressed in terms of these time scales as follows:

$$\exp(-iE_nt/\hbar) = \exp\left[-\frac{iE_{\overline{n}}t}{\hbar} - \frac{2\pi i(n-\overline{n})t}{T_{\mathrm{cl}}} - \frac{2\pi i(n-\overline{n})^2t}{T_{\mathrm{rev}}} - \frac{2\pi i(n-\overline{n})^3t}{T_{\mathrm{sr}}} + \cdots\right]. \tag{3.32}$$

Consequently, the time evolution of BGCS is governed by these three time scales, which are controlled by the dependence of the energy on the quantum number n. The term containing $iE_{\overline{n}}t/\hbar$ in equation (3.32) is n-independent, being unimportant for the expansion of $\Psi_\alpha(x,y;t)$.

In order to explore the time evolution of the BGCS, the time scales may be computed through equations (3.30) and (3.31). Before doing that, the probability distribution of the occupation number $P_\alpha(n) = |\langle\Psi_n^+|\Psi_\alpha\rangle|^2$ must be calculated to determine the mean value $\overline{n}$.

For the BGCS of equation (3.21) the probability distribution of the occupation number becomes

$$P_\alpha(n) = |\langle\Psi_n^+|\Psi_\alpha\rangle|^2 = \frac{1}{2\exp(|\alpha|^2) - |\alpha|^2 - 1} \times \begin{cases} 1 & \text{for} \quad n=0, \\ |\alpha|^2 & \text{for} \quad n=1, \\ \dfrac{2|\alpha|^{2n}}{n!} & \text{for} \quad n\geq 2, \end{cases} \tag{3.33}$$

where $|\alpha|^2 = \zeta^2$.

The probability distribution $P_\alpha(n)$ for the states of equation (3.23) is given by

$$P_\alpha(n) = \frac{1}{2\exp(|\alpha|^2) - 1} \times \begin{cases} 1 & \text{for} \quad n=1, \\ \dfrac{2|\alpha|^{2(n-1)}}{(n-1)!} & \text{for} \quad n\geq 2. \end{cases} \tag{3.34}$$

Finally, for the BGCS of equation (3.25) the probability distribution $P_\alpha(n)$ turns out to be

$$P_\alpha(n) = \frac{1}{{}_0F_2(1,2;r^2)}\left(\frac{|\alpha|^{2(n-2)}}{(n-1)![(n-2)!]^2}\right), \qquad \text{for} \qquad n\geq 2. \tag{3.35}$$

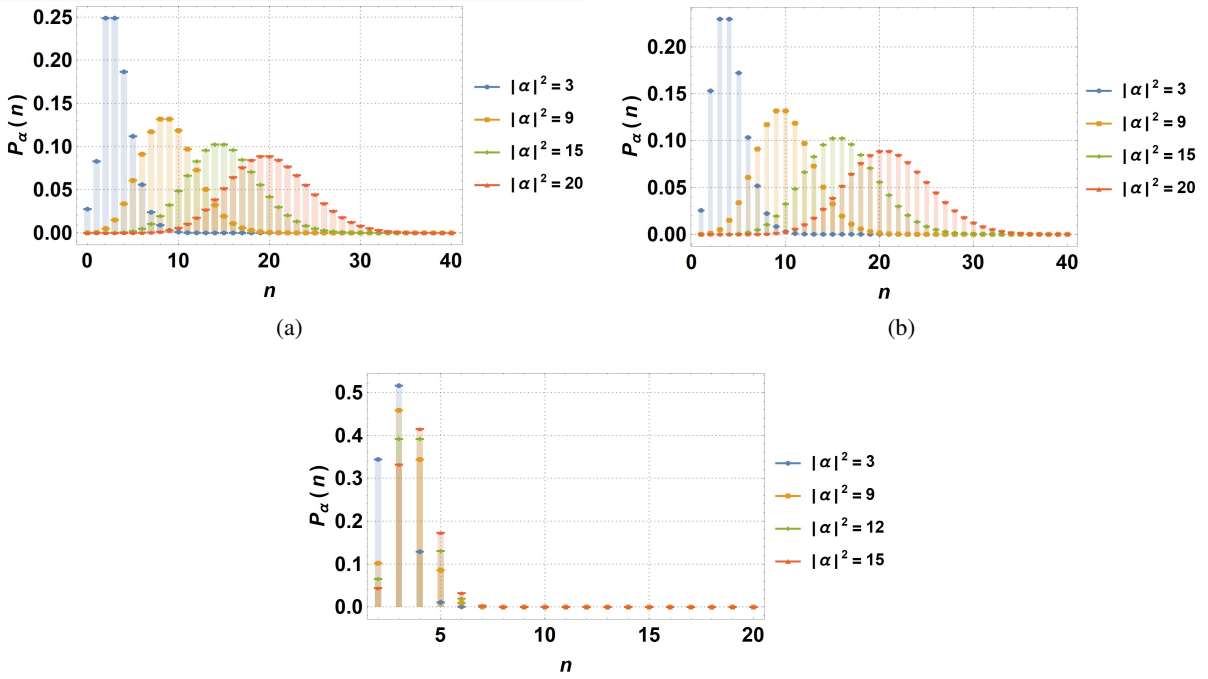

Figure 3.4: Probability distribution of occupation number $P_\alpha(n)$ for the three sets of BGCS. Subfigures (a), (b) and (c) correspond to the BGCS in equations (3.21), (3.23) and (3.25), respectively.

These distributions are shown in figure 3.4. Note that for the first two sets of BGCS $P_\alpha(n)$ follows a Poisson-like distribution centered approximately around $|\alpha|^2$ (see figures 3.4(a) and 3.4(b)). Thus, for the BGCS (3.21) and (3.23) the distribution $P_\alpha(n)$ has a mean at $\overline{n} \approx |\alpha|^2$, as in the canonical coherent states (see [46]). Meanwhile, for the last set this is no longer true.

In order to illustrate the bilayer graphene time scales, we have chosen a typical value of $\overline{n} = 9$, and from the expressions for the periods in equation (3.31) we can find the time scales of most interest for our study:

$$T_{\rm cl} \simeq \frac{2\pi}{\omega_c^*}, \quad T_{\rm rev} \simeq \frac{9775\pi}{\omega_c^*}, \quad T_{\rm sr} \simeq \frac{82800\pi}{\omega_c^*}. \tag{3.36}$$

As can be seen, for $\overline{n} = 9$ the first time scale is $T_{\rm cl} \simeq 2\pi/\omega_c^*$, *i.e.*, the classical period of motion for our BGCS is similar to the period of evolution of the harmonic oscillator. However, the other time scales $T_{\rm rev}$ and $T_{\rm sr}$ take very large values. This is the reason to conclude that the wave packets of the previously derived BGCS do not collapse, thus they cannot have revivals, as it happens for the canonical coherent states.

Autocorrelation function

A useful tool to analyze the dynamics of a quantum system is the autocorrelation function, which supplies a qualitative way to know how long a quantum state persists at two different times, and it is defined as

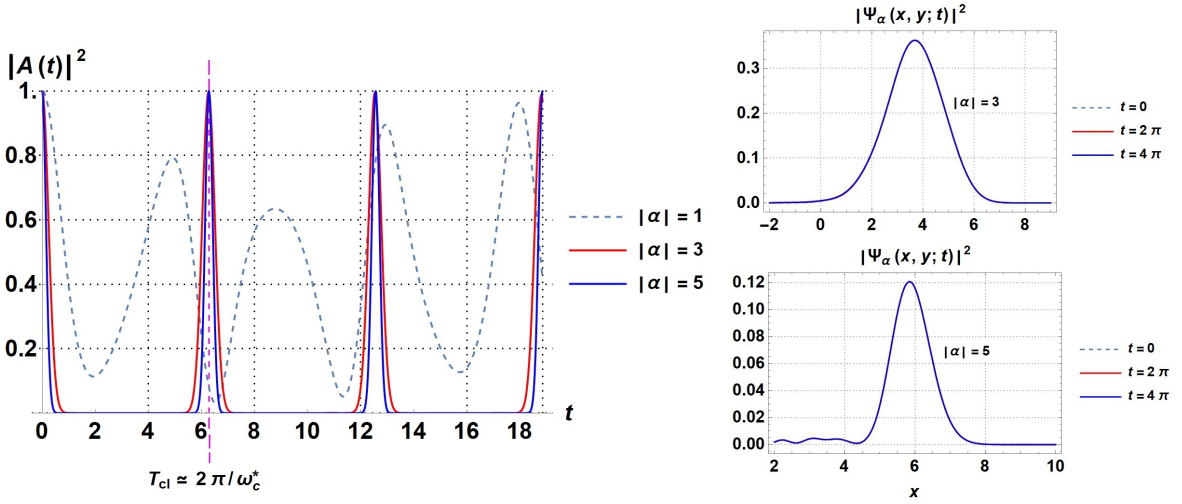

Figure 3.5: Left: Modulus squared $|A(t)|^2$ of the autocorrelation function for the BGCS (3.21) with several values of $|\alpha|$. Right: Probability densities $|\Psi_\alpha(x,y;t)|^2$ for $|\alpha| = 3$, $|\alpha| = 5$ and several fixed times, multiples of the classical period $T_{\rm cl} \simeq 2\pi/\omega_c^*$. The values $\varphi = 0$ and $\omega_c^* = 1$ were taken.

follows

$$A(t) := \langle \Psi(\mathbf{r},0)|\Psi(\mathbf{r},t)\rangle = \int_{-\infty}^{\infty} \Psi^\dagger(\mathbf{r},0)\Psi(\mathbf{r},t)d\mathbf{r}. \tag{3.37}$$

Through the modulus squared $|A(t)|^2$ of this function it is possible to illustrate the different types of revival structures that a given quantum system could have. Let us point out that $|A(t)|^2$ is bounded between 0 and 1. When the modulus squared of the autocorrelation function is close to or equal to one, $|A(t)|^2 \simeq 1$, the quantum state $\Psi(\mathbf{r},t)$ approximately matches with the initial state $\Psi(\mathbf{r},0)$. On the other hand, if $|A(t)|^2 \simeq 0$ the evolved state is far from the initial one.

The autocorrelation function for the BGCS (3.21) becomes

$$A(t) = \frac{1}{2\exp(\zeta^2) - \zeta^2 - 1}\left\{1 + |\alpha|^2 + 2\sum_{n=2}^{\infty}\frac{|\alpha|^{2n}}{n!}\exp\left[-i\sqrt{n(n-1)}\,\omega_c^* t\right]\right\}. \tag{3.38}$$

The modulus squared $|A(t)|^2$ of such autocorrelation function is shown in figure 3.5 for different values of $|\alpha|$.

The autocorrelation function for the second set of BGCS (3.23) turns out to be

$$A(t) = \frac{1}{2\exp(\zeta^2) - 1}\left\{1 + 2\sum_{n=2}^{\infty}\frac{|\alpha|^{2(n-1)}}{(n-1)!}\exp\left[-i\sqrt{n(n-1)}\,\omega_c^* t\right]\right\}. \tag{3.39}$$

The modulus squared $|A(t)|^2$ of such autocorrelation function is shown in figure 3.6 for different values of $|\alpha|$.

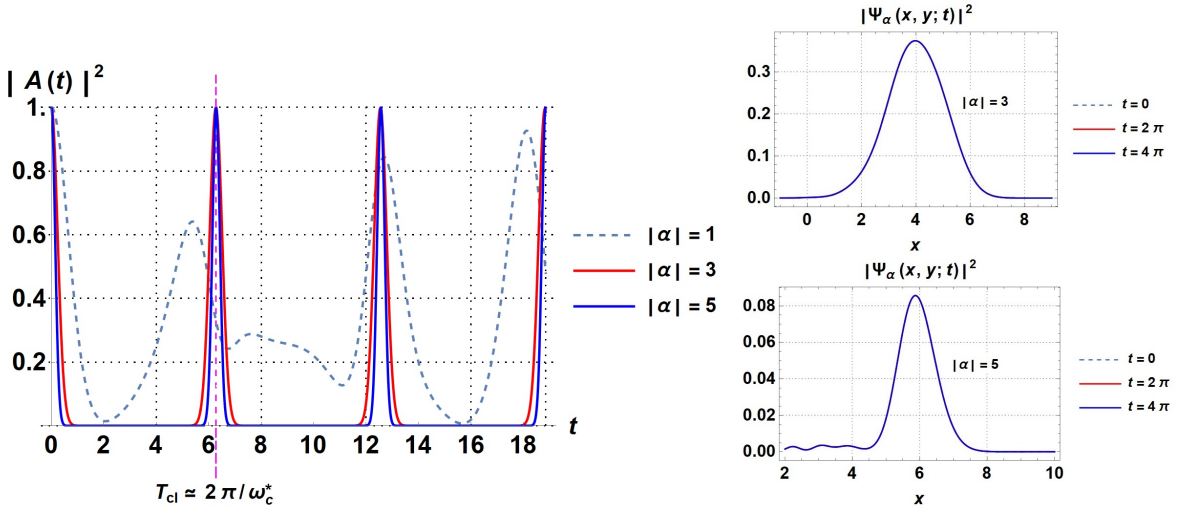

Figure 3.6: Left: Modulus squared $|A(t)|^2$ of the autocorrelation function for the BGCS (3.23) with several values of $|\alpha|$. Right: Probability densities $|\Psi_\alpha(x,y;t)|^2$ for $|\alpha| = 3$, $|\alpha| = 5$ and several fixed times, multiples of the classical period $T_{\rm cl} \simeq 2\pi/\omega_c^*$. The values $\varphi = 0$ and $\omega_c^* = 1$ were taken.

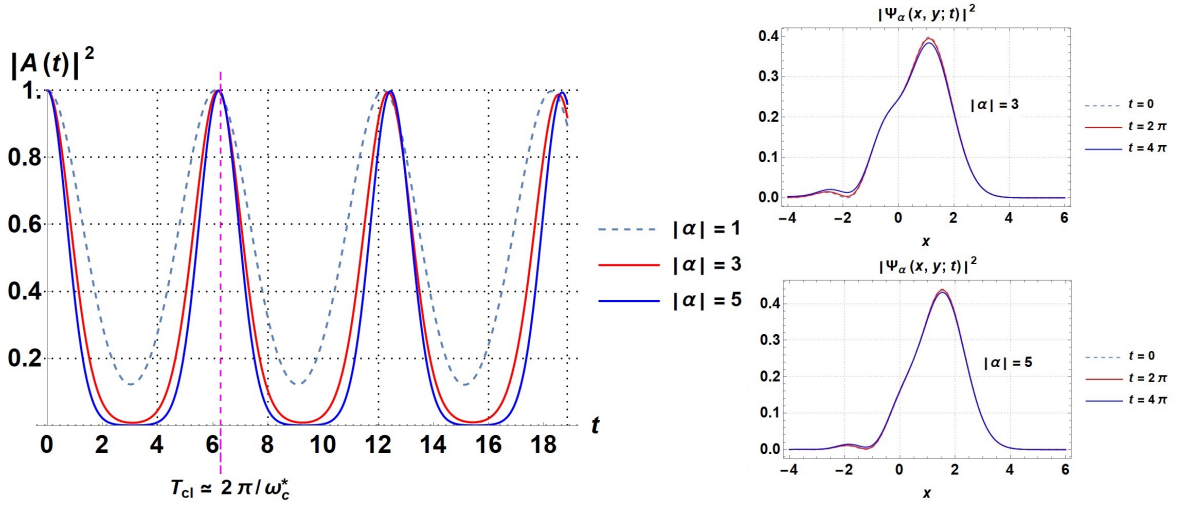

Figure 3.7: Left: Modulus squared $|A(t)|^2$ of the autocorrelation function for the BGCS (3.25) with several values of $|\alpha|$. Right: Probability densities $|\Psi_\alpha(x,y;t)|^2$ for $|\alpha| = 3$, $|\alpha| = 5$ and several fixed times, multiples of the classical period $T_{\rm cl} \simeq 2\pi/\omega_c^*$. The values $\varphi = 0$ and $\omega_c^* = 1$ were taken.

Finally, the autocorrelation function $A(t)$ for the last set of BGCS (3.25) is given by

$$A(t) = \frac{1}{{}_0F_2(1,2;r^2)} \sum_{n=2}^{\infty} \frac{|\alpha|^{2(n-2)}}{[(n-2)!]^2(n-1)!} \exp\left[-i\omega_c^* \sqrt{n(n-1)}\, t\right], \tag{3.40}$$

whose modulus squared is shown in the figure 3.7.

As can be seen, the modulus squared $|A(t)|^2$ of the autocorrelation function has approximately the same behavior for the three families of BGCS, *i.e.*, for $|\alpha| \geq 3$ the function $|A(t)|^2$ is practically equal to one for times equal to the classic time $T_{\text{cl}} \simeq 2\pi/\omega_c^*$ and its multiplies. Moreover, it has an oscillatory behavior and disappears for times different from T_{cl} (see figures 3.5-3.7). Therefore, the three evolved sets of BGCS $\Psi_\alpha(\mathbf{r};t)$ are recovered approximately at T_{cl} and its multiplies.

Chapter 4

Multiphoton coherent states for bilayer graphene

4.1 Multiphoton coherent states

As mentioned before, the CS can be generalized, *i.e.*, defined appropriately in order to describe different systems. The so-called multiphoton coherent states (MCS) are generalizations of the CS, defined as eigenstates of a generalized or deformed annihilation operator $a_g^- := (a^-)^k$ with complex eigenvalues $\tilde{z}$ [56–58]:

$$a_g^- |\tilde{z}\rangle_k = \tilde{z}|\tilde{z}\rangle_k, \qquad \tilde{z} \in \mathbb{C}. \tag{4.1}$$

The generalized ladder operators a_g^-, $a_g^+ := (a_g^-)^\dagger$ and the harmonic oscillator Hamiltonian generate an algebraic structure called polynomial Heisenberg algebra, in which the Hilbert space $\mathscr{H}$ with basis vectors $|n\rangle$ is decomposed as a direct sum of k orthogonal subspaces $\mathscr{H}_j$ [60–63]:

$$\mathscr{H} = \oplus_{j=0}^{k-1} \mathscr{H}_j. \tag{4.2}$$

As a consequence, the MCS $|\tilde{z}\rangle_k$ can be constructed on each subspace $\mathscr{H}_j$ using equation (4.1) by expressing them as superpositions of the Fock states $|kn+j\rangle$ as follows (see [64])

$$|\tilde{z}\rangle_k = c_j^k \sum_{n=0}^{\infty} \frac{\tilde{z}^n}{\sqrt{(kn+j)!}} |kn+j\rangle, \qquad j = 0, \ldots, k-1, \tag{4.3}$$

with c_j^k being normalization constants.

The BGCS were derived in the previous chapter , and their time evolution was explored. In order to extend and generalize this treatment, in this chapter the multiphoton coherent states for electrons in bilayer graphene will be constructed as eigenstates of a generalized annihilation operator, analyzing as well some physical quantities associated to them [65].

4.1.1 Generalized annihilation operator $\mathbf{A}_\mathbf{g}^-$

Consider first a generalized annihilation operator $\mathbf{A}_g^-$ defined as follows

$$\mathbf{A}_g^- := (\mathbf{A}^-)^k, \qquad k \in Z^+. \tag{4.4}$$

Using the expression of $\mathbf{A}^-$ given in equation (3.7), the operator $\mathbf{A}_g^-$ turns out to be

$$\mathbf{A}_g^- = \begin{pmatrix} \prod_{m=0}^{k-1} f_3(N+mI)(\theta^-)^k & 0 \\ 0 & \prod_{m=1}^{k} f(N+mI)(\theta^-)^k \end{pmatrix}, \tag{4.5}$$

where, f, f_3 will be used to ensure that

$$\mathbf{A}_g^- \Psi_n^{\pm}(x,y) = c_n^k \Psi_{n-k}^{\pm}(x,y), \tag{4.6}$$

with c_n^k being coefficients to determine later, and $\{\Psi_n^{\pm}(x,y)\}_{n=0}^{\infty}$ are the Landau states of the bilayer graphene effective Hamiltonian (2.30).

By applying $\mathbf{A}_g^-$ onto the eigenstates $\Psi_n^{\pm}(x,y)$, in order to satisfy equation (4.6), the functions f, f_3 must fulfil the following constraint,

$$\sqrt{(n-2)\cdots[n-(k+1)]}f_3(n-3)\cdots f_3(n-(k+2)) = \sqrt{n\cdots[n-(k-1)]}f(n)\cdots f(n-(k-1)). \tag{4.7}$$

Consequently, the generalized annihilation operator $\mathbf{A}_g^-$ can be rewritten as follows

$$\mathbf{A}_g^- = \begin{pmatrix} \frac{\sqrt{(N+3I)\cdots(N+(k+2)I)}}{\sqrt{(N+I)\cdots(N+kI)}} \prod_{m=3}^{k+2} f(N+mI)(\theta^-)^k & 0 \\ 0 & \prod_{m=1}^{k} f(N+mI)(\theta^-)^k \end{pmatrix}, \tag{4.8}$$

thus the coefficients c_n^k can easily be determined,

$$\mathbf{A}_g^- \Psi_n^{\pm}(x,y) = \begin{cases} 0 & \text{for} \quad n = 0,1,\ldots,k-1, \\ \sqrt{\frac{(1+\delta_{k1})\,n!}{2}}\,[f(n)]!\,\Psi_0^{\pm}(x,y) & \text{for} \quad n = k, \\ \frac{\sqrt{n!}}{\sqrt{2}}\frac{[f(n)]!}{f(1)}\Psi_1^{\pm}(x,y) & \text{for} \quad n = k+1, \\ \sqrt{\frac{n!}{(n-k)!}}\frac{[f(n)]!}{[f(n-k)]!}\Psi_{n-k}^{\pm}(x,y) & \text{for} \quad n = k+2, k+3,\ldots, \end{cases} \tag{4.9}$$

where δ_{ij} is the Kronecker delta and $[f(n)]!$ is calculated according to equation (3.14).

4.1.2 Bilayer graphene MCS as eigenstates of $\mathbf{A}_g^-$

The bilayer graphene MCS (BGMCS) can be constructed as eigenstates $\Psi_{\tilde{\alpha}}^k(x,y)$ of the generalized annihilation operator $\mathbf{A}_g^-$ of equation (4.8) with complex eigenvalue $\tilde{\alpha}$,

$$\mathbf{A}_g^- \Psi_{\tilde{\alpha}}^k(x,y) = \tilde{\alpha}\Psi_{\tilde{\alpha}}^k(x,y), \qquad \tilde{\alpha} \in \mathbb{C}, \tag{4.10}$$

where states $\Psi^k_{\tilde{\alpha}}(x,y)$ are expressed as linear combinations of $\{\Psi^+_n(x,y)\}^{\infty}_{n=0}$, *i.e.*,

$$\Psi^k_{\tilde{\alpha}}(x,y) = \sum_{n=0}^{\infty} C^k_n \Psi^+_n(x,y). \tag{4.11}$$

From equations (4.9) - (4.11), and using the linear independence of the states $\{\Psi^+_n(x,y)\}^{\infty}_{n=0}$, two recurrence relationships for the coefficients C^k_n are obtained, which after some work lead to

$$C^k_k = \frac{\sqrt{2}\,\tilde{\alpha}}{\sqrt{(1+\delta_{k1})\,k!\,[f(k)]!}} C^k_0, \tag{4.12}$$

$$C^k_{n+k} = \sqrt{\frac{2^{\delta_{n1}} n!}{(n+k)!}} \frac{[f(n)]!\,\tilde{\alpha}}{[f(n+k)]!} C^k_n, \quad n = 1,2,\ldots \tag{4.13}$$

Note that there are k free parameters, $\{C^k_0, C^k_1, \ldots, C^k_{k-1}\} = \left\{C^k_j\right\}^{k-1}_{j=0}$, thus k independent sets of BGMCS can be constructed, all of them depending on the choice of $f(n)$.

First of all, suppose that $f(n) \neq 0 \quad \forall \quad n = 1,2,\ldots$ In particular, equations (4.12) and (4.13) for $k = 1$ lead to

$$C^1_1 = \frac{\tilde{\alpha}}{f(1)} C^1_0, \qquad C^1_{n+1} = \sqrt{\frac{2^{\delta_{n1}}}{(n+1)}} \frac{\tilde{\alpha}}{f(n+1)} C^1_n, \quad n = 1,2,\ldots, \tag{4.14}$$

with C^1_0 being the only free parameter. Since these recurrence relationships are the same as the ones obtained in equation (3.12), the BGMCS for $k = 1$ and $j = 0$ become

$$\Psi^1_{\tilde{\alpha}}(x,y) = C^1_0 \left[\Psi^+_0(x,y) + \sum_{n=1}^{\infty} \frac{\sqrt{2^{1-\delta_{n1}}}\,\tilde{\alpha}^n}{\sqrt{n!}\,[f(n)]!} \Psi^+_n(x,y)\right], \tag{4.15}$$

where C^1_0 will be used for normalizing them. These states are identical to the BGCS of equation (3.15) with $\tilde{\alpha} = \alpha$, *i.e.*, for $k = 1$ the BGCS are recovered.

On the other hand, for $k > 1$, k independent relations arise from equations (4.12), (4.13),

$$C^k_{kn+j} = \frac{\left[\sqrt{2}\delta_{j0} + \sqrt{(\delta_{j1}+j)!}\right]\,[f(j)]!\,\tilde{\alpha}^n}{\sqrt{(kn+j)!}\,[f(kn+j)]!} C^k_j, \quad n = 1,2,\ldots, \tag{4.16}$$

where $j = \{0,1,2,\ldots,k-1\}$. Thus, from equations (4.11) and (4.16) the BGMCS turn out to be

$$\Psi^k_{\tilde{\alpha}}(x,y) = C^k_j \left[\Psi^+_j(x,y) + \sum_{n=1}^{\infty} \frac{\left[\sqrt{2}\delta_{j0} + \sqrt{(\delta_{j1}+j)!}\right]\,[f(j)]!\,\tilde{\alpha}^n}{\sqrt{(kn+j)!}\,[f(kn+j)]!} \Psi^+_{kn+j}(x,y)\right]. \tag{4.17}$$

The parameters C^k_j will be used for normalizing the BGMCS, which in general depend on the values of the pair $\{k,j\}$. Therefore, it is natural to redefine these states as $\Psi^k_{\tilde{\alpha}}(x,y) := \Psi^{k,j}_{\tilde{\alpha}}(x,y)$. In this context, k is used to indicate the order and j represents the family of the BGMCS. This notation will be used from now on.

Some important explicit expressions of the states $\Psi^{k,j}_{\tilde{\alpha}}(x,y)$ will be written next.

Case $k=2$

For $k=2$ the index j can take two values, $\{0,1\}$, thus two sets of BGMCS will be obtained:

$$\Psi_{\tilde{\alpha}}^{2,0}(x,y)=\left[1+\sum_{n=1}^{\infty}\frac{2|\tilde{\alpha}|^{2n}}{(2n)![[f(2n)]!]^2}\right]^{-1/2}\left[\Psi_0^+ +\sum_{n=1}^{\infty}\frac{\sqrt{2}\tilde{\alpha}^n}{\sqrt{(2n)!}\,[f(2n)]!}\Psi_{2n}^+\right], \tag{4.18}$$

$$\Psi_{\tilde{\alpha}}^{2,1}(x,y)=\left[1+\sum_{n=1}^{\infty}\frac{2[f(1)]^2|\tilde{\alpha}|^{2n}}{(2n+1)![[f(2n+1)]!]^2}\right]^{-1/2}\left[\Psi_1^+ +\sum_{n=1}^{\infty}\frac{\sqrt{2}f(1)\tilde{\alpha}^n}{\sqrt{(2n+1)!}\,[f(2n+1)]!}\Psi_{2n+1}^+\right]. \tag{4.19}$$

These states can also be obtained as even and odd superpositions of bilayer graphene coherent states, which has been recently implemented for the particular case when $f(n)=1$ in [68].

Case $k=3$

On the other hand, for $k=3$ the index j can take three values, $\{0,1,2\}$, thus three sets of BGMCS are obtained:

$$\Psi_{\tilde{\alpha}}^{3,0}(x,y)=\left[1+\sum_{n=1}^{\infty}\frac{2|\tilde{\alpha}|^{2n}}{(3n)![[f(3n)]!]^2}\right]^{-1/2}\left[\Psi_0^+ +\sum_{n=1}^{\infty}\frac{\sqrt{2}\tilde{\alpha}^n}{\sqrt{(3n)!}\,[f(3n)]!}\Psi_{3n}^+\right], \tag{4.20}$$

$$\Psi_{\tilde{\alpha}}^{3,1}(x,y)=\left[1+\sum_{n=1}^{\infty}\frac{2[f(1)]^2|\tilde{\alpha}|^{2n}}{(3n+1)![[f(3n+1)]!]^2}\right]^{-1/2}\left[\Psi_1^+ +\sum_{n=1}^{\infty}\frac{\sqrt{2}f(1)\tilde{\alpha}^n}{\sqrt{(3n+1)!}\,[f(3n+1)]!}\Psi_{3n+1}^+\right], \tag{4.21}$$

$$\Psi_{\tilde{\alpha}}^{3,2}(x,y)=\left[1+\sum_{n=1}^{\infty}\frac{2[f(1)f(2)]^2|\tilde{\alpha}|^{2n}}{(3n+2)![[f(3n+2)]!]^2}\right]^{-1/2}\left[\Psi_2^+ +\sum_{n=1}^{\infty}\frac{\sqrt{2}f(1)f(2)\tilde{\alpha}^n}{\sqrt{(3n+2)!}\,[f(3n+2)]!}\Psi_{3n+2}^+\right]. \tag{4.22}$$

Additional sets of BGMCS could be written explicitly, all of them depending on the particular choice of $f(n)$ and the parameters $\{k,j\}$. In order to analyze the electrons behavior in bilayer graphene, several physical quantities for the states $\Psi_{\tilde{\alpha}}^{k,j}(x,y)$ will be computed in the following sections.

4.2 Physical quantities for the BGMCS

The BGMCS belong to the Hilbert space $\mathscr{H}$, thus several physical quantities can be calculated in order to describe the system behavior in such approach.

4.2.1 Heisenberg uncertainty relation

An important physical quantities useful to characterize a quantum state is the Heisenberg uncertainty relation (HUR). In order to obtain this quantity for the BGMCS, the following matrix operators $\hat{S}_\ell$ and their squares are defined as follows [69]:

$$\hat{S}_\ell=\hat{s}_\ell\otimes\hat{1}, \qquad \hat{S}_\ell^2=\hat{s}_\ell^2\otimes\hat{1}, \tag{4.23}$$

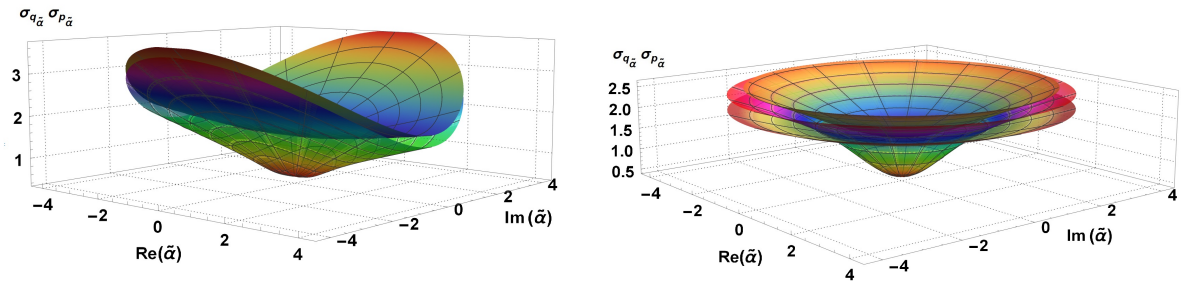

(a) (b)

Figure 4.1: Heisenberg uncertainty product $\sigma_{\hat{q}_{\tilde{\alpha}}}\sigma_{\hat{p}_{\tilde{\alpha}}}$ as function of $\tilde{\alpha}$ for the BGMCS with $f(n)=1$ and: (a) $k=2$, $j=0,1$; (b) $k=3$, $j=0,1,2$.

where

$$\hat{s}_\ell = \frac{1}{\sqrt{2}i^\ell}\left[\theta^- + (-1)^\ell \theta^+\right], \tag{4.24}$$

$$\hat{s}_\ell^2 = \frac{1}{2}\left\{2N + I + (-1)^\ell\left[(\theta^-)^2 + (\theta^+)^2\right]\right\}, \tag{4.25}$$

with $\ell = 0,1$, such that $\langle \hat{S}_\ell\rangle|_{\ell=0} = \langle q\rangle$ and $\langle \hat{S}_\ell\rangle|_{\ell=1} = \langle p\rangle$ (similarly for their squares). The mean values of the operators $\hat{S}_\ell$ and their squares turn out to be $\langle \hat{S}_\ell\rangle = 0$ for all k and

$$\begin{aligned}\langle \hat{S}_\ell^2\rangle =& |C_j^k|^2\left\{\frac{(1-\delta_{j0}-\delta_{j1})^2(2j-3)+2j+1}{2^{1-\delta_{j0}-\delta_{j1}}} + \left(\frac{[f(j)]!\left[\sqrt{2}\delta_{j0}+\sqrt{(\delta_{j1}+j)!}\right]}{[f(kn+j)]!}\right)^2\right.\\ &\times\sum_{n=1}^{\infty}\frac{|\tilde{\alpha}|^{2n}(2kn+2j-1)}{(kn+j)!} + (-1)^\ell 2\,\mathrm{Re}(\tilde{\alpha})\left[\frac{[f(j)]!}{[f(kn+j)]!\sqrt{2^{1-\delta_{j0}-\delta_{j1}}\,j!}}+\right.\\ &\left.\left.+\left(\frac{[f(j)]!}{[f(kn+j)]!}\right)^2\left(\sum_{n=1}^{\infty}\frac{|\tilde{\alpha}|^{2n}}{(kn+j)!}+\sum_{n=1}^{\infty}\frac{|\tilde{\alpha}|^{2n}}{\sqrt{(kn+j+2)!(kn+j-2)!}}\right)\right]\delta_{k2}\right\}.\end{aligned} \tag{4.26}$$

The standard deviation for $\hat{S}_\ell$ will be found through

$$\sigma_{\hat{S}_\ell} = \sqrt{\langle \hat{S}_\ell^2\rangle - \langle \hat{S}_\ell\rangle^2}, \tag{4.27}$$

thus, the HUR for the BGMCS fulfills

$$(\sigma_q)_{\tilde{\alpha}}\,(\sigma_p)_{\tilde{\alpha}} \geq \frac{1}{2}. \tag{4.28}$$

For the eigenstates $\Psi_n^+(x,y)$, the resulting uncertainty relations are:

$$(\sigma_q)_0\,(\sigma_p)_0 = \frac{1}{2}, \qquad n=0,$$

$$(\sigma_q)_1\,(\sigma_p)_1 = \frac{3}{2}, \qquad n=1,$$

$$(\sigma_q)_n(\sigma_p)_n = n - \frac{1}{2} \geq \frac{1}{2}, \qquad n = 2,3,\ldots$$

Figures 4.1(a) and 4.1(b) show the resulting Heisenberg uncertainty product $\sigma_{q_{\tilde{\alpha}}}\sigma_{p_{\tilde{\alpha}}}$ as function of $\tilde{\alpha}$ for $f(n) = 1$ and the two k-values $k = \{2,3\}$, respectively.

4.2.2 Probability density

The probability density $\rho_{\tilde{\alpha}}^{k,j}(x) = (\Psi_{\tilde{\alpha}}^{k,j}(x,y))^{\dagger}\Psi_{\tilde{\alpha}}^{k,j}(x,y)$ for the BGMCS of equation (4.17) is

$$\begin{aligned}\rho_{\tilde{\alpha}}^{k,j}(x) = |C_j^k|^2 \Bigg\{ & \frac{(1-\delta_{j0}-\delta_{j1})^2|\psi_{j-2}|^2 + |\psi_j|^2}{\sqrt{2^{1-\delta_{j0}-\delta_{j1}}}} + \frac{[\sqrt{2}\delta_{j0} + \sqrt{(\delta_{j1}+j)!}]}{\sqrt{2^{2-\delta_{j0}-\delta_{j1}}}} \Bigg[\sum_{n=1}^{\infty} \frac{\tilde{\zeta}^n \cos(n\tilde{\varphi})}{\sqrt{(kn+j)!}} \\ & \times \frac{[f(j)]!}{[f(kn+j)]!} \left((1-\delta_{j0}-\delta_{j1})\psi_{kn+j-2}\psi_{j-2}^* + \psi_{kn+j}\psi_j^* \right) + \sum_{n'=1}^{\infty} \frac{\tilde{\zeta}^{n'}\cos(n'\tilde{\varphi})}{\sqrt{(kn'+j)!}} \frac{[f(j)]!}{[f(kn'+j)]!} \\ & \times \left((1-\delta_{j0}-\delta_{j1})\psi_{kn'+j-2}^*\psi_{j-2} + \psi_{kn'+j}^*\psi_j \right) \Bigg] + \frac{[\sqrt{2}\delta_{j0} + \sqrt{(\delta_{j1}+j)!}]^2}{2} \sum_{n=1}^{\infty}\sum_{n'=1}^{\infty} \frac{\tilde{\zeta}^{n+n'}\cos[(n-n')\tilde{\varphi}]}{\sqrt{(kn+j)!(kn'+j)!}} \\ & \times \frac{[[f(j)]!]^2(\psi_{kn+j-2}\psi_{kn'+j-2}^* + \psi_{kn+j}\psi_{kn'+j}^*)}{[f(kn+j)]![f(kn'+j)]!} \Bigg\},\end{aligned} \tag{4.29}$$

where the polar form $\tilde{\alpha} = \tilde{\zeta}\exp(i\tilde{\varphi}) = \tilde{\zeta}(\cos\tilde{\varphi} + i\sin\tilde{\varphi})$ has been used. Some graphs of $\rho_{\tilde{\alpha}}^{k,j}(x)$ for $f(n) = 1$, $k = 2$ and $k = 3$ are shown in figures 4.2(a)-4.2(e).

4.2.3 Mean energy value

We calculate the expected value of the Hamiltonian to characterize the energy of the system. Thus, the mean energy value $\langle H_{\text{eff}}\rangle_{\tilde{\alpha}}$ for states $\Psi_{\tilde{\alpha}}^{k,j}(x,y)$ is obtained through

$$\langle H_{\text{eff}}\rangle_{\tilde{\alpha}}^{k,j} = \langle \Psi_{\tilde{\alpha}}^{k,j} | H_{\text{eff}} | \Psi_{\tilde{\alpha}}^{k,j}\rangle, \tag{4.30}$$

with H_{eff} being the bilayer graphene Hamiltonian (2.14). Performing the calculation with the states $\Psi_{\tilde{\alpha}}^{k,j}(x,y)$ in equation (4.17), we obtain

$$\langle H_{\text{eff}}\rangle_{\tilde{\alpha}}^{k,j} = |C_j^k|^2\hbar\omega_c^* \left[\sqrt{j(j-1)} + \left(\sqrt{2}\delta_{j0} + \sqrt{(\delta_{j1}+j)!} \right)^2 \sum_{n=1}^{\infty} \frac{[f(j)]!^2 \sqrt{(kn+j)(kn+j-1)}}{[f(kn+j)]!^2 (kn+j)!} |\tilde{\alpha}|^{2n} \right]. \tag{4.31}$$

This quantity will be useful later on to analyze the time evolution of the BGMCS in terms of the approximate period τ, in the same way as in equation (3.28). Figures 4.3-4.4 show the mean energy value (4.31) as function of $|\tilde{\alpha}| = \tilde{\zeta}$ for the BGMCS with $f(n) = 1$ and the two k-values $k = \{2,3\}$.

Discussion

Several physical quantities have been calculated previously when the system is in a BGMCS. As can be seen in figures 4.1(a) and 4.1(b), the corresponding Heisenberg uncertainty relation acquires a minimum when $\tilde{\alpha} \to 0$ which depends on the eigenstate $\Psi_j^+(x,y)$ with minimum energy eigenvalue involved in the

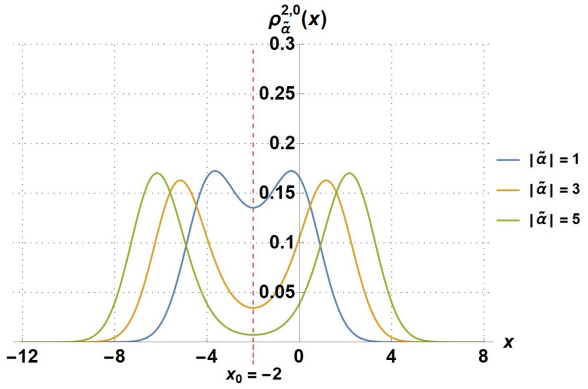

(a) $k = 2$, $j = 0$

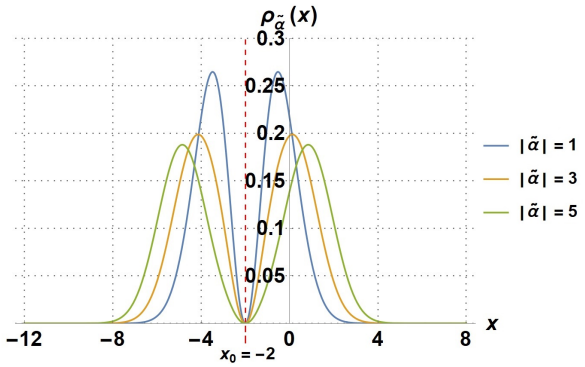

(b) $k = 2$, $j = 1$

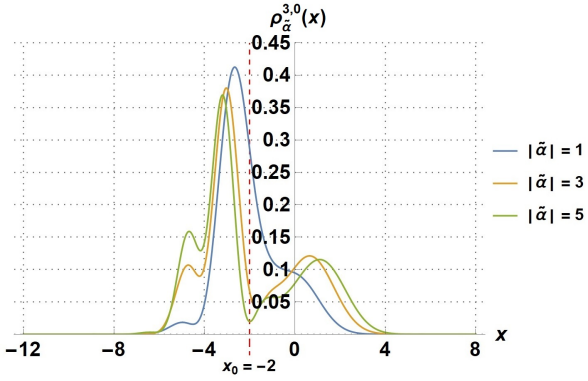

(c) $k = 3$, $j = 0$

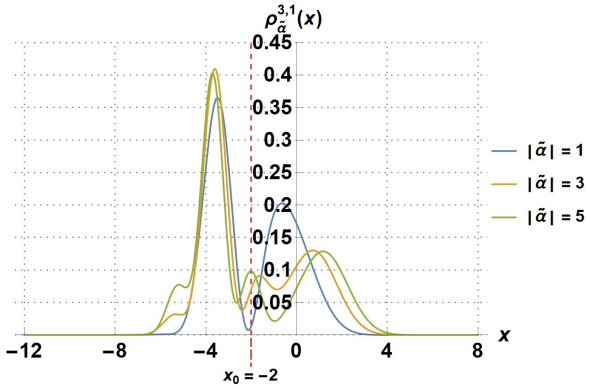

(d) $k = 3$, $j = 1$

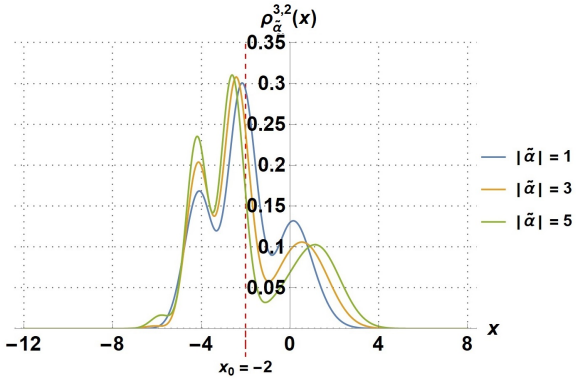

(e) $k = 3$, $j = 2$

Figure 4.2: Probability density $\rho_{\tilde{\alpha}}^{k,j}(x)$ for the BGMCS with $f(n) = 1$, $\omega_c^* = 1$, $k = 2$, $k = 3$ and different values of $\tilde{\zeta} = |\tilde{\alpha}|$ with $\tilde{\varphi} = 0$.

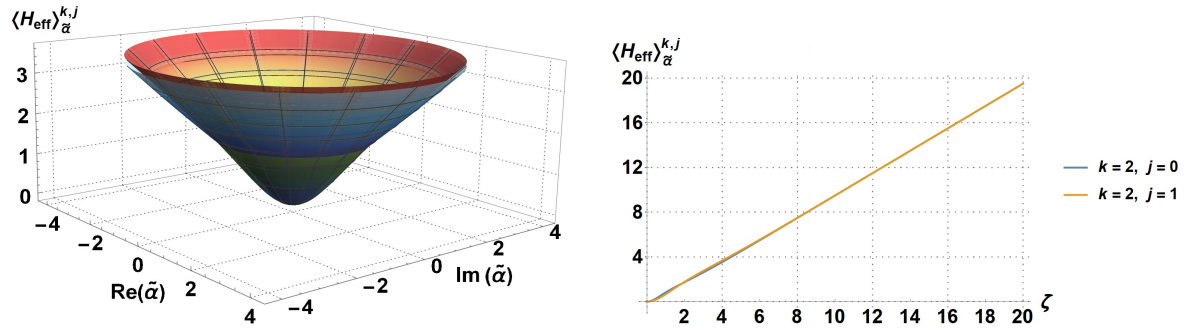

(a) (b)

Figure 4.3: Mean energy value $\langle H_{\text{eff}}\rangle_{\tilde{\alpha}}^{k,j}$ for the BGMCS with $f(n)=1$, $k=2$, $j=\{0,1\}$ and $\hbar\omega_c^*=1$.

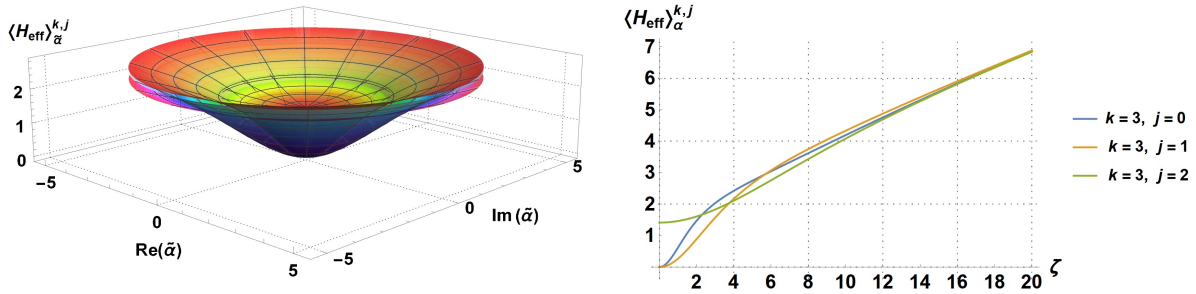

(a) (b)

Figure 4.4: Mean energy value $\langle H_{\text{eff}}\rangle_{\tilde{\alpha}}^{k,j}$ for the BGMCS with $f(n)=1$, $k=3$, $j=\{0,1,2\}$ and $\hbar\omega_c^*=1$.

linear decomposition. Thus, for the states $\Psi_{\tilde{\alpha}}^{k,j}(x,y)$ with $k=2$, $j=0$ and $k=3$, $j=0$ the HUR achieves the minimum value $1/2$, while for the other three cases ($k=2$, $j=1$; $k=3$, $j=1$; and $k=3$, $j=2$) this quantity tends to $3/2$ when $\tilde{\alpha}$ goes to zero. This two values are the same values taken for the states $\Psi_n^+(x,y)$ with $n=0,1,2,3$.

On the other hand, the probability density for the BGMCS shows an oscillatory behavior around the point $x_0=-2k/\omega_c^*$, which is similar to what happens for the BGCS [50]. Moreover, this behavior becomes more pronounced as $\tilde{\zeta}$ increases and $\rho_{\tilde{\alpha}}^{k,j}(x)$ extends along x-direction (see figures 4.2(a)-4.2(e)). Therefore, by choosing a specific $\tilde{\alpha}$ it is possible to find the electrons in a given region with the highest probability.

Finally, figures 4.3(b)-4.4(b) indicate that the mean energy value for the BGMCS is a continuous function of $|\tilde{\alpha}|$ whose behavior above a certain $|\tilde{\alpha}|$ is approximately linear. Moreover, when $|\tilde{\alpha}|\to 0$ the asymptotic value of $\langle H_{\text{eff}}\rangle_{\tilde{\alpha}}^{k,j}$ is different for each set $\Psi_{\tilde{\alpha}}^{k,j}(x,y)$, since in this limit the BGMCS tend to the state Ψ_j^+ with minimum energy eigenvalue involved in the linear decomposition, which is different for different j (see equations (4.18-4.22)).

4.3 Evolution of the BGMCS

The time evolution operator $U(t)=\exp(-iH_{\text{eff}}t/\hbar)$ acting on the states $\Psi^{k,j}_{\tilde{\alpha}}(x,y)$ of equation (4.17) will induce the corresponding dynamical behavior. Thus, the evolved state is given by:

$$\begin{aligned}\Psi^{k,j}_{\tilde{\alpha}}(x,y;t) =& C^k_j\left[\mathrm{e}^{-i\sqrt{j(j-1)}\,\omega_c^* t}\Psi^+_j+\sum_{n=1}^{\infty}\frac{\left[\sqrt{2}\delta_{j0}+\sqrt{(\delta_{j1}+j)!}\right]\,[f(j)]!\,\tilde{\alpha}^n}{\sqrt{(kn+j)!}\,[f(kn+j)]!}\right.\\ &\left.\times\mathrm{e}^{-i\sqrt{(kn+j)(kn+j-1)}\,\omega_c^* t}\Psi^+_{kn+j}\right].\end{aligned} \tag{4.32}$$

The evolved probability density for the BGMCS with $\tilde{\alpha}=\tilde{\zeta}\exp^{i\tilde{\varphi}}$ becomes

$$\begin{aligned}\rho_{\tilde{\alpha}}(x,t) =& |C^k_j|^2\left\{\frac{(1-\delta_{j0}-\delta_{j1})^2|\psi_{j-2}|^2+|\psi_j|^2}{\sqrt{2^{1-\delta_{j0}-\delta_{j1}}}}+\frac{[\sqrt{2}\delta_{j0}+\sqrt{(\delta_{j1}+j)!}]^2}{2}\sum_{n=1}^{\infty}\sum_{n'=1}^{\infty}\frac{\tilde{\zeta}^{n+n'}}{\sqrt{(kn+j)!(kn'+j)!}}\right.\\
&\times\frac{[[f(j)]!]^2}{[f(kn'+j)]![f(kn+j)]!}\cos[(\sqrt{(kn+j)(kn+j-1)}-\sqrt{(kn'+j)(kn'+j-1)})\,\omega_c^* t-(n-n')\tilde{\varphi}]\\
&\times(\psi_{kn+j-2}\psi^*_{kn'+j-2}+\psi_{kn+j}\psi^*_{kn'+j})+\frac{[\sqrt{2}\delta_{j0}+\sqrt{(\delta_{j1}+j)!}]}{\sqrt{2^{2-\delta_{j0}-\delta_{j1}}}}\left[\sum_{n'=1}^{\infty}\frac{\tilde{\zeta}^{n'}}{\sqrt{(kn'+j)!}}\frac{[f(j)]!}{[f(kn'+j)]!}\right.\\
&\times\cos[(\sqrt{(kn'+j)(kn'+j-1)}-\sqrt{j(j-1)})\,\omega_c^* t-n'\tilde{\varphi}]\,((1-\delta_{j0}-\delta_{j1})\psi^*_{kn'+j-2}\psi_{j-2}+\psi^*_{kn'+j}\psi_j)\\
&+\sum_{n=1}^{\infty}\frac{\tilde{\zeta}^n}{\sqrt{(kn+j)!}}\frac{[f(j)]!}{[f(kn+j)]!}\cos[(\sqrt{(kn+j)(kn+j-1)}-\sqrt{j(j-1)})\,\omega_c^* t-n\tilde{\varphi}]((1-\delta_{j0}-\delta_{j1})\\
&\left.\left.\times\psi_{kn+j-2}\psi^*_{j-2}+\psi_{kn+j}\psi^*_j)\right]\right\}.\end{aligned} \tag{4.33}$$

In figures 4.5-4.9 the evolved probability densities (4.33) are shown, with $f(n)=1$ and the two values $k=\{2,3\}$.

Discussion

Similar to the BGCS derived previously, the BGMCS will be stable in time if the contribution of the first two energy eigenstates $\Psi^+_0(x,y)$ and $\Psi^+_1(x,y)$ is either null or small compared with the contribution of all other eigenstates. Such behavior can be seen in figure 4.9, where the evolved BGMCS for $k=3$ and $j=2$ are stable in time, with a period $\tau\simeq 2\pi/3\omega_c^*$. Moreover, as $|\tilde{\alpha}|$ grows ($|\tilde{\alpha}|\to\infty$) this condition is also fulfilled, thus the BGMCS in practice are stable in time for all k and j, with a period $\tau\simeq 2\pi/k\omega_c^*$.

However, if the contribution of the states $\Psi^+_0(x,y)$ and $\Psi^+_1(x,y)$ is non-trivial compared with all other contributions, the states $\Psi^{k,j}_{\tilde{\alpha}}(x,y)$ will be only approximately stable in time, *i.e.*, only for some values of t the probability density looks similar to what it was at $t=0$ (see figures 4.5-4.8). To explain this evolution, an approximate period τ can be calculated, as obtained previously for the BGCS (3.28). Thus, by setting $\tilde{\alpha}$ the mean energy value is computed first, then the interval in which it lies is determined, which is bounded by two energies E_{kn+j+k} and E_{kn+j} such that $E_{kn+j}<\langle H_{\text{eff}}\rangle^{k,j}_{\tilde{\alpha}}<E_{kn+j+k}$. Thus, the possible approximate period is obtained

$$\tau=\frac{2\pi\hbar}{E_{kn+j+k}-E_{kn+j}}. \tag{4.34}$$

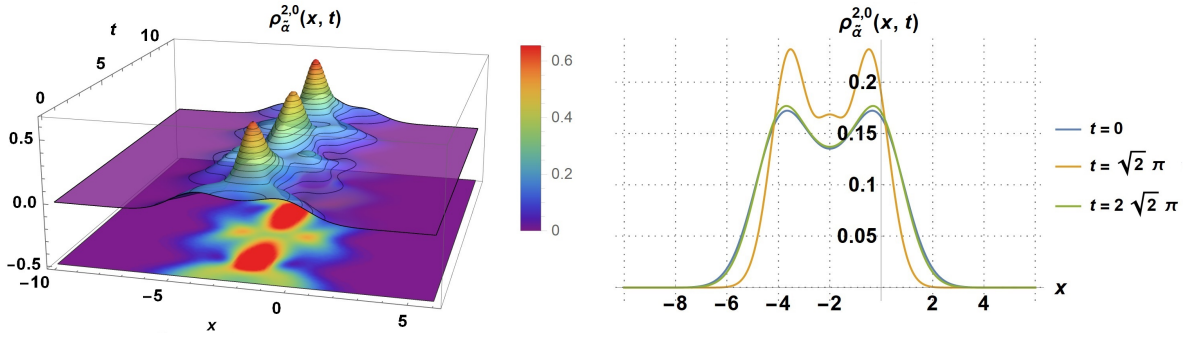

(a) (b)

Figure 4.5: Left: Probability density $\rho_{\tilde{\alpha}}^{k,j}(x,t)$ for the BGMCS with $f(n)=1$, $k=2$ and $j=0$. Right: Probability density at some fixed times (suggested approximate period $\tau \simeq \sqrt{2}\pi$ and some of its multiples). The values $|\tilde{\alpha}|=1$, $\theta=0$ and $\omega_c^*=1$ were taken.

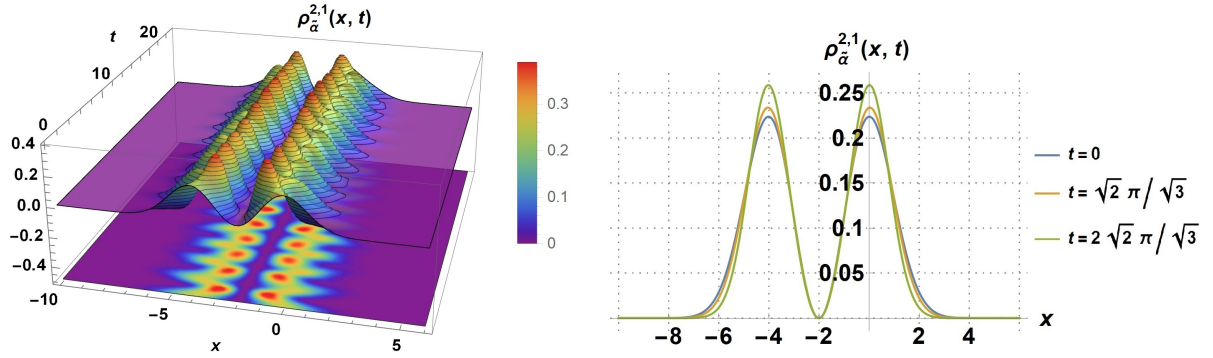

(a) (b)

Figure 4.6: Left: Probability density $\rho_{\tilde{\alpha}}^{k,j}(x,t)$ for the BGMCS with $f(n)=1$, $k=2$ and $j=1$. Right: Probability density at some fixed times (suggested approximate period $\tau \simeq \sqrt{2}\pi/\sqrt{3}$ and some of its multiples). The values $|\tilde{\alpha}|=1$, $\theta=0$ and $\omega_c^*=1$ were taken.

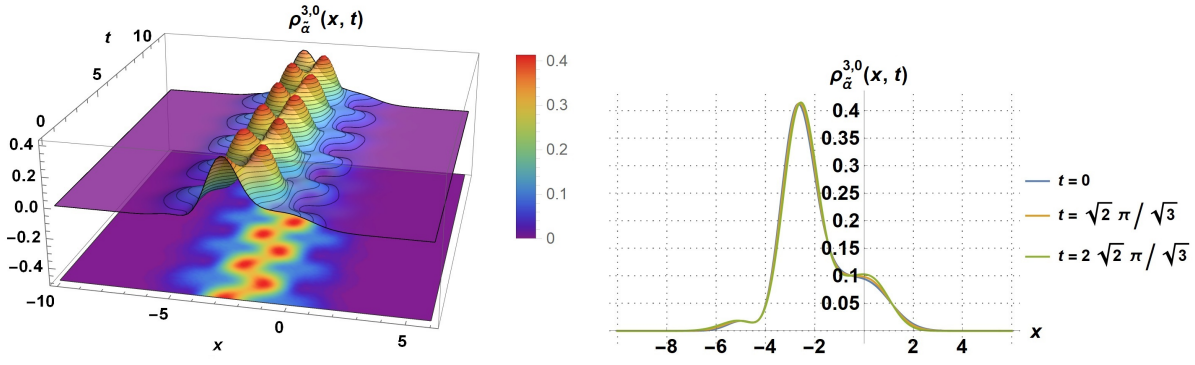

(a) (b)

Figure 4.7: Left: Probability density $\rho_{\tilde{\alpha}}^{k,j}(x,t)$ for the BGMCS with $f(n)=1$, $k=3$ and $j=0$. Right: Probability density at some fixed times (suggested approximate period $\tau \simeq \sqrt{2}\pi/\sqrt{3}$ and some of its multiples). The values $|\tilde{\alpha}|=1$, $\theta=0$ and $\omega_c^*=1$ were taken.

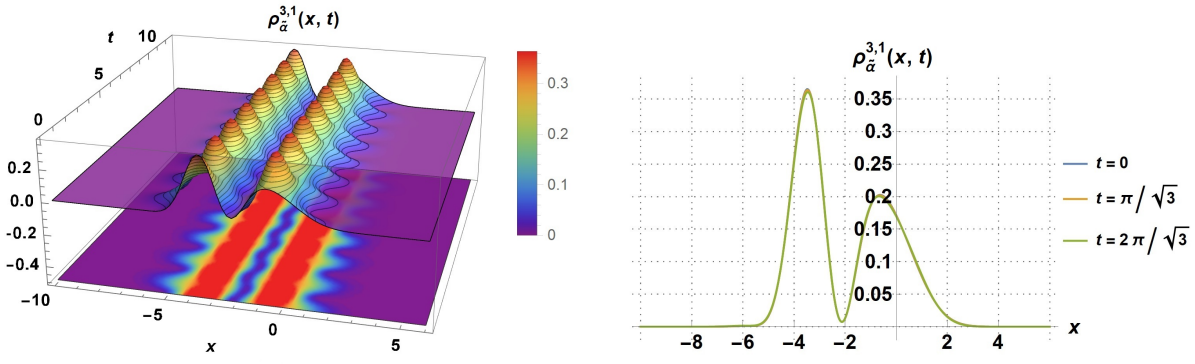

(a) (b)

Figure 4.8: Left: Probability density $\rho_{\tilde{\alpha}}^{k,j}(x,t)$ for the BGMCS with $f(n)=1$, $k=3$ and $j=1$. Right: Probability density at some fixed times (suggested approximate period $\tau \simeq \pi/\sqrt{3}$ and some of its multiples). The values $|\tilde{\alpha}|=1$, $\theta=0$ and $\omega_c^*=1$ were taken.

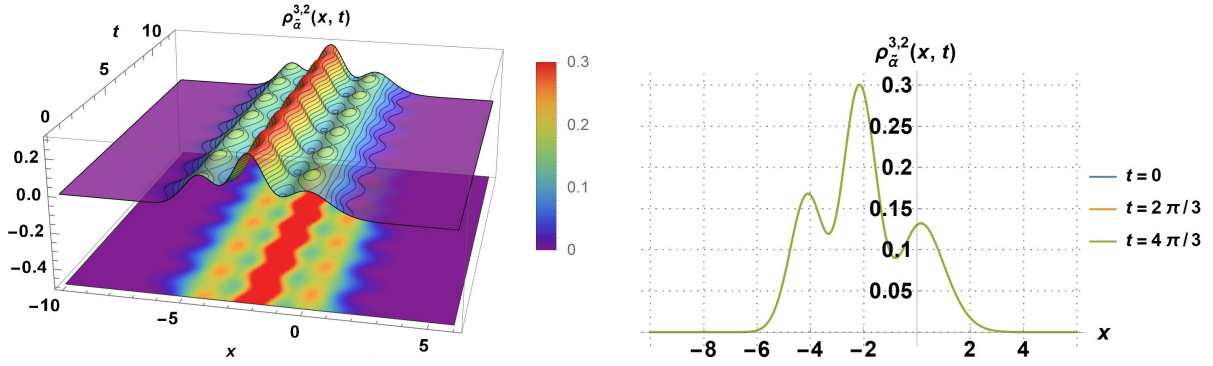

(a) (b)

Figure 4.9: Left: Probability density $\rho_{\tilde{\alpha}}^{k,j}(x,t)$ for the BGMCS with $f(n)=1$, $k=3$ and $j=2$. Right: Probability density at some fixed times (suggested approximate period $\tau \simeq 2\pi/3$ and some of its multiples). The values $|\tilde{\alpha}|=1$, $\theta=0$ and $\omega_c^*=1$ were taken.

As an example, the approximate period τ for the BGMCS (4.32) with $|\tilde{\alpha}|=1$, $k=2$ and $k=3$ has been obtained. Figures 4.5-4.9 show their probability density $\rho_{\tilde{\alpha}}^{k,j}(x,t)$ evaluated at τ and some of its multiples.

4.3.1 Revival structure and autocorrelation function for the BGMCS

To analyze further the dynamics of the BGMCS, the time scales and autocorrelation function $A(t)$ will be computed, as in equations (3.31) and (3.37), respectively. For $\overline{n}=9$, the most interesting time scale for our study corresponds to the classical period T_{cl}, given by

$$T_{\mathrm{cl}} = \frac{4\pi\sqrt{(3k+j)(3k+j-1)}}{k(6k+2j-1)\omega_c^*}. \tag{4.35}$$

According to equations (4.35), for the BGMCS with $k=2$ the classical period is $T_{\mathrm{cl}} \simeq \pi/\omega_c^*$ for both values of j, while in the case with $k=3$ we obtain that $T_{\mathrm{cl}} \simeq 2\pi/3\omega_c^*$ for $j=0,1,2$. The other time scales are not relevant because they are too large.

On the other hand, using equations (4.17) and (4.32) the autocorrelation function for the BGMCS becomes

$$A(t) = |C_j^k|^2 \left[\mathrm{e}^{-i\sqrt{j(j-1)}\,\omega_c^* t} + \sum_{n=1}^{\infty} \frac{\left[\sqrt{2}\delta_{j0} + \sqrt{(\delta_{j1}+j)!}\right]^2 [[f(j)]!]^2 |\tilde{\alpha}|^{2n}}{(kn+j)!\,[[f(kn+j)]!]^2} \mathrm{e}^{-i\sqrt{(kn+j)(kn+j-1)}\,\omega_c^* t} \right]. \tag{4.36}$$

In figures 4.10-4.14 the modulus squared $|A(t)|^2$ of the autocorrelation function for the BGMCS is shown for $k=2$ and $k=3$, with $\omega_c^*=1$, $f(n)=1$ and several values of $|\tilde{\alpha}|$.

This function supplies a qualitative way to know how long a BGMCS persists at two different times. More precisely, its modulus squared indicates how close the evolved state at time $t>0$ is to the initial

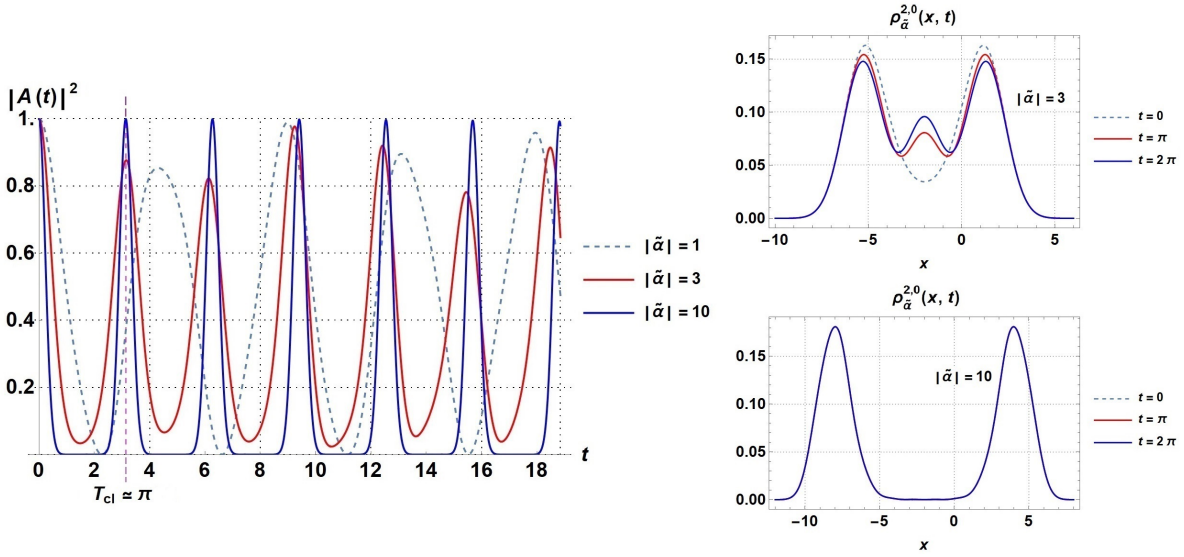

Figure 4.10: Left: Modulus squared $|A(t)|^2$ of the auto-correlation function for the BGMCS with several values of $|\tilde{\alpha}|$, $f(n)=1$, $k=2$ and $j=0$. Right: Probability density $\rho^{k,j}_{\tilde{\alpha}}(x,t)$ with $|\tilde{\alpha}|=3$ and $|\tilde{\alpha}|=10$ for several fixed times, multiples of the first time scale $T_{\rm cl}\simeq\pi$. The values $\tilde{\varphi}=0$ and $\omega_c^*=1$ were taken.

state at $t=0$. For the BGMCS with $k=2$ and $k=3$ $|A(t)|^2$ shows an oscillatory behavior, which depends on the value of $|\tilde{\alpha}|$ (see figures 4.10-4.14). If the modulus squared of the autocorrelation function is very close or equal to one, $|A(t)|^2\approx 1$, the states $\Psi^{k,j}_{\tilde{\alpha}}(x,y;t)$ and $\Psi^{k,j}_{\tilde{\alpha}}(x,y;0)$ are said to be almost completely correlated, *i.e.*, the BGMCS at $t=0$ is reconstructed at some $t>0$. In figures 4.10-4.14 the modulus squared of $A(t)$ is shown for several values of $|\tilde{\alpha}|$. From these plots it can be seen that for values of $|\tilde{\alpha}|\to\infty$ the modulus squared of $A(t)$ reaches approximately the value of one at $T_{\rm cl}$ for any family of BGMCS, *i.e.*, through this quantity it is possible to identify out the first time scale. In addition, the probability densities for some fixed times (the time scale $T_{\rm cl}$ and some multiples) are also plotted.

As it was pointed out before, the BGMCS are stable when the contribution of the states $\Psi^+_0(x,y)$ and $\Psi^+_1(x,y)$ is small compared to the eigenstates with $n\geq 2$, as the BGCS derived in chapter 3, and their period becomes the first time scale $T_{\rm cl}$ defined in equation (3.31). Moreover, in this regime the period of the BGMCS turns out to be a fraction of the period of the BGCS (see figures 4.15 and 4.16), *i.e.*, $T^{\rm BGMCS}_{\rm cl}=T^{\rm BGCS}_{\rm cl}/k=2\pi/k\omega_c^*$, turning them into non-classical states. This is similar to what happens for the multiphoton coherent states of the harmonic oscillator [59].

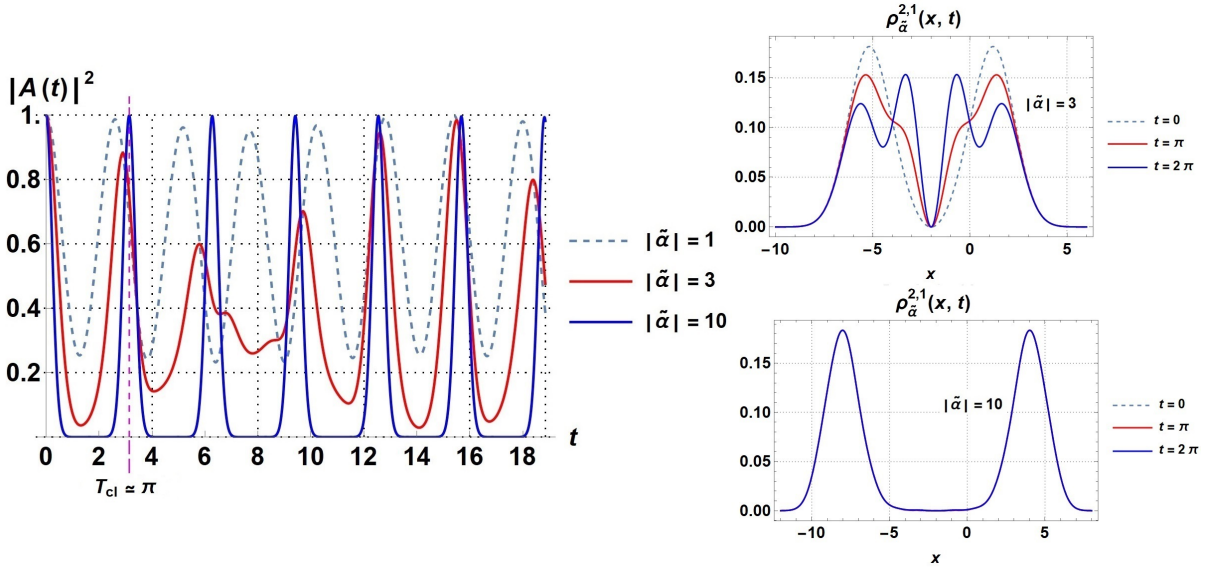

Figure 4.11: Left: Modulus squared $|A(t)|^2$ of the autocorrelation function for the BGMCS with several values of $|\tilde{\alpha}|$, $f(n)=1$, $k=2$ and $j=1$. Right: Probability density $\rho^{k,j}_{\tilde{\alpha}}(x,t)$ with $|\tilde{\alpha}|=3$ and $|\tilde{\alpha}|=10$ for several fixed times, multiples of the first time scale $T_{\rm cl}\simeq\pi$. The values $\tilde{\varphi}=0$ and $\omega_c^*=1$ were taken.

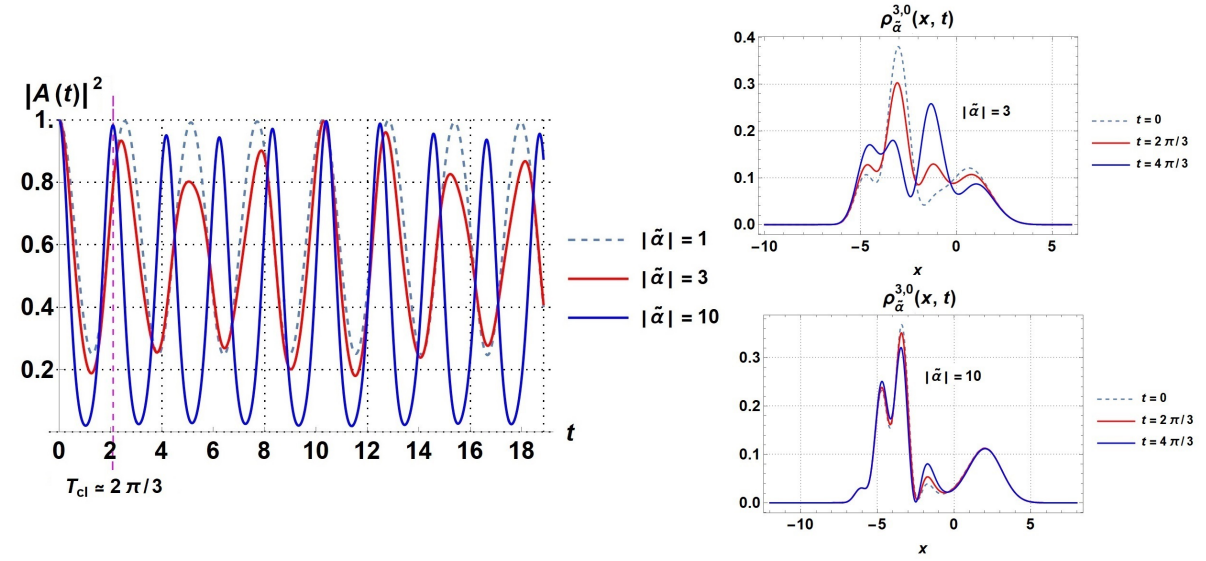

Figure 4.12: Left: Modulus squared $|A(t)|^2$ of the autocorrelation function for the BGMCS with several values of $|\tilde{\alpha}|$, $f(n)=1$, $k=3$ and $j=0$. Right: Probability density $\rho^{k,j}_{\tilde{\alpha}}(x,t)$ with $|\tilde{\alpha}|=3$ and $|\tilde{\alpha}|=10$ for several fixed times, multiples of the first time scale $T_{\rm cl}\simeq 2\pi/3$. The values $\tilde{\varphi}=0$ and $\omega_c^*=1$ were taken.

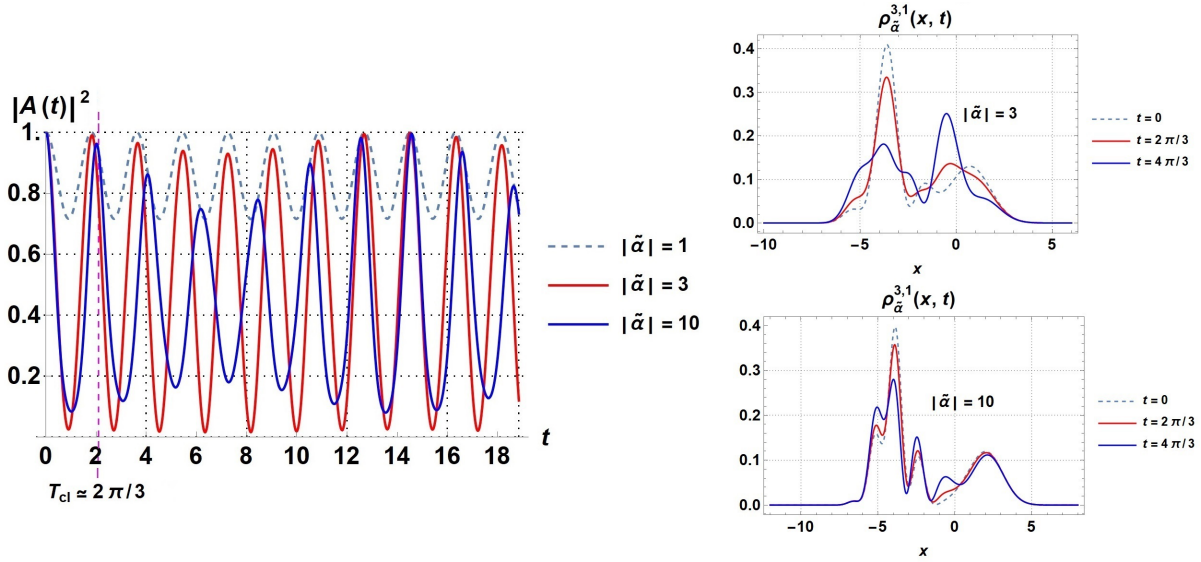

Figure 4.13: Left: Modulus squared $|A(t)|^2$ of the autocorrelation function for the BGMCS with several values of $|\tilde{\alpha}|$, $f(n) = 1$, $k = 3$ and $j = 1$. Right: Probability density $\rho^{k,j}_{\tilde{\alpha}}(x,t)$ with $|\tilde{\alpha}| = 3$ and $|\tilde{\alpha}| = 10$ for several fixed times, multiples of the first time scale $T_{\rm cl} \simeq 2\pi/3$. The values $\tilde{\varphi} = 0$ and $\omega_c^* = 1$ were taken.

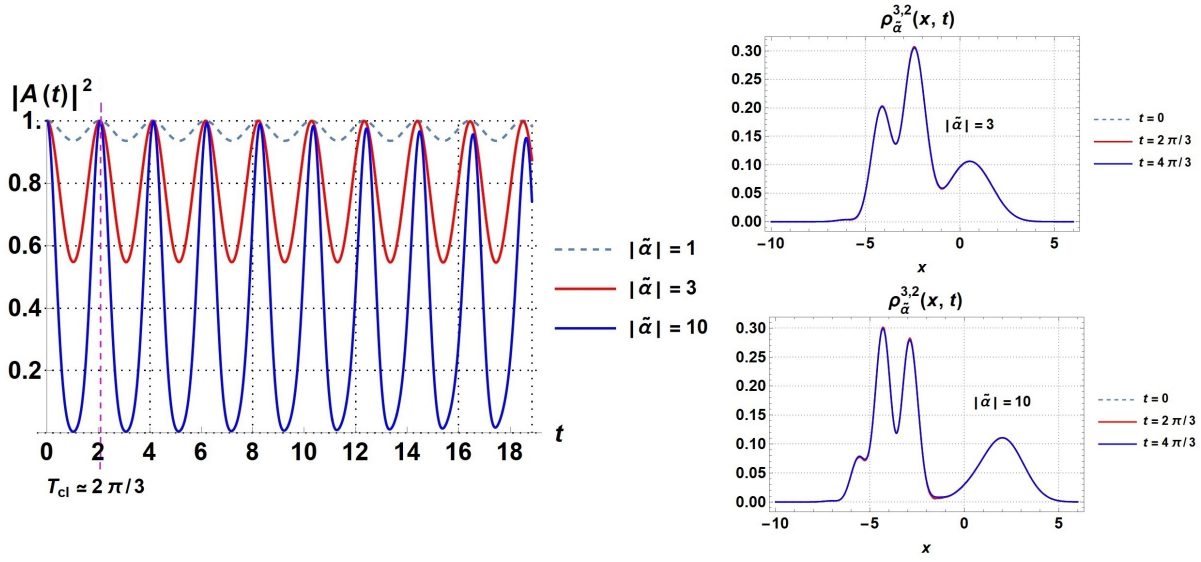

Figure 4.14: Left: Modulus squared $|A(t)|^2$ of the autocorrelation function for the BGMCS with several values of $|\tilde{\alpha}|$, $f(n) = 1$, $k = 3$ and $j = 2$. Right: Probability density $\rho^{k,j}_{\tilde{\alpha}}(x,t)$ with $|\tilde{\alpha}| = 3$ and $|\tilde{\alpha}| = 10$ for several fixed times, multiples of the first time scale $T_{\rm cl} \simeq 2\pi/3$. The values $\tilde{\varphi} = 0$ and $\omega_c^* = 1$ were taken.

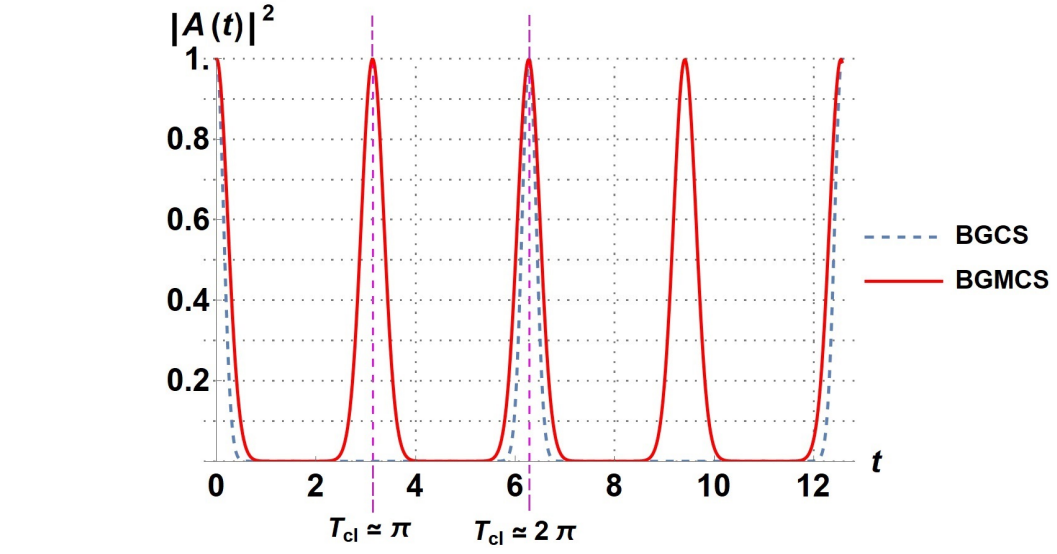

(a)

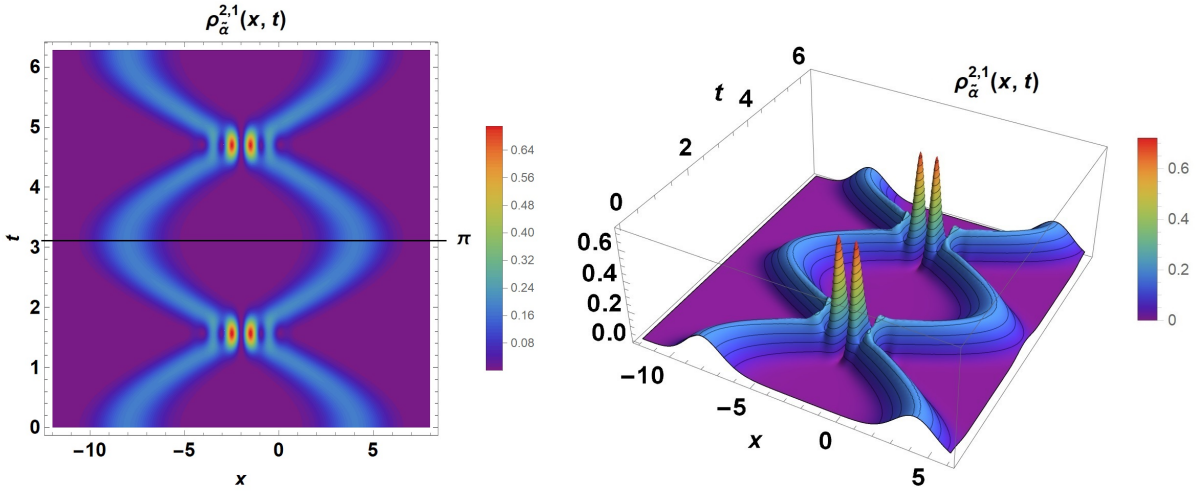

(b) (c)

Figure 4.15: (a) Modulus squared $|A(t)|^2$ of the autocorrelation function for the BGCS in (3.21) with $|\alpha| = 5$ and the BGMCS (4.19) with $|\tilde{\alpha}| = 10$. From $|A(t)|^2 \approx 1$ it can be identify the first time scale $T_{\rm cl}$ for both sets, being $T_{\rm cl}^{\rm BGCS} \simeq 2\pi$ for the BGCS and $T_{\rm cl}^{\rm BGMCS} \simeq \pi$ for the BGMCS. In (b) and (c) the probability density $\rho_{\tilde{\alpha}}^{k,j}(x,t)$ is plotted for the BGMCS with $f(n) = 1$, $|\tilde{\alpha}| = 10$, $k = 2$ and $j = 1$, in order to show the periodicity of this state and its period. The values $\tilde{\varphi} = 0$ and $\omega_c^* = 1$ were taken.

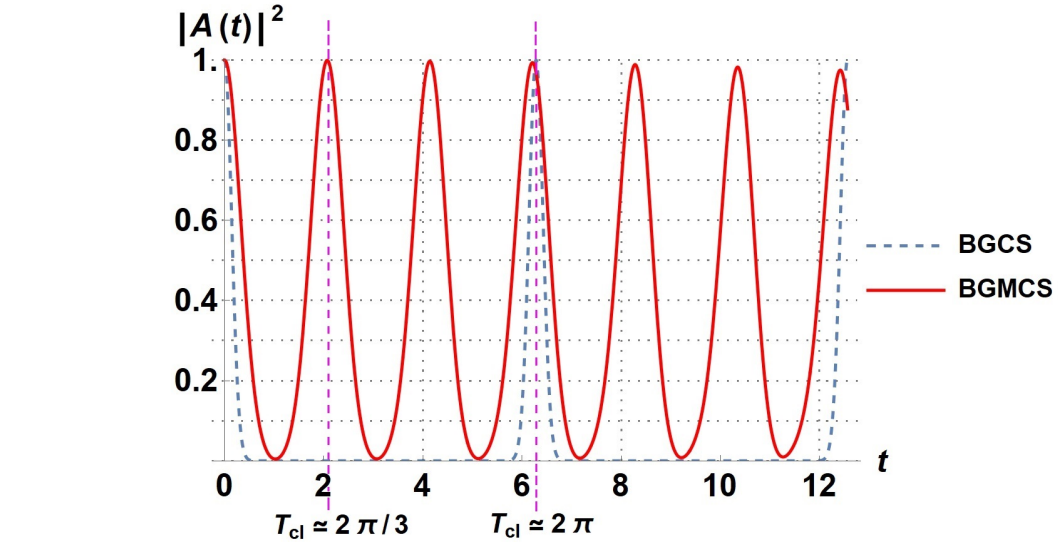

(a)

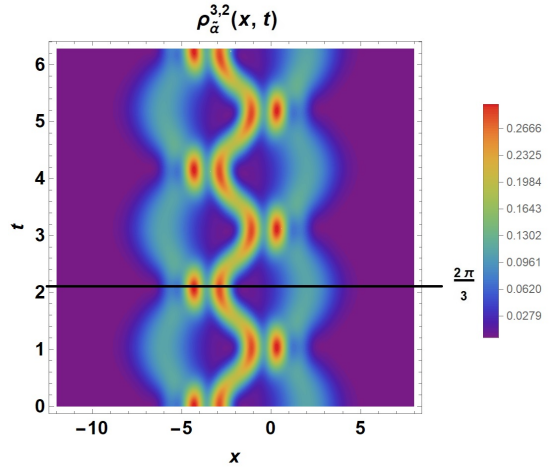

(b)

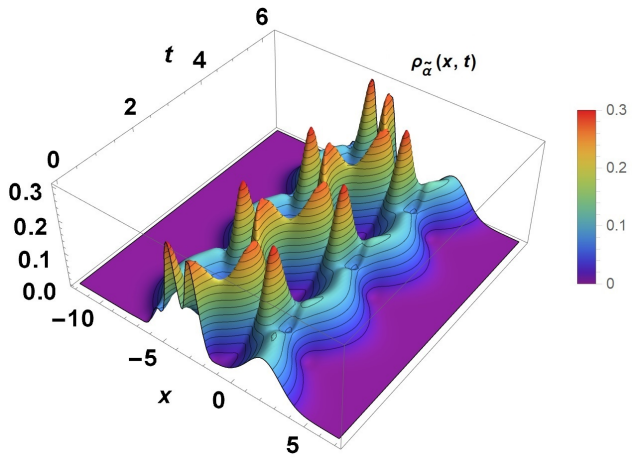

(c)

Figure 4.16: (a) Modulus squared absolute $|A(t)|^2$ of the autocorrelation function for the BGCS (3.21) with $|\alpha| = 5$ and the BGMCS (4.22) with $|\tilde{\alpha}| = 10$. From $|A(t)|^2 \approx 1$ it can be identify the first time scale T_{cl} for both sets, being $T_{\text{cl}}^{\text{BGCS}} \simeq 2\pi$ for the BGCS and $T_{\text{cl}}^{\text{BGMCS}} \simeq 2\pi/3$ for the BGMCS. In (b) and (c) the probability density $\rho_{\tilde{\alpha}}^{k,j}(x,t)$ is plotted for the BGMCS with $f(n) = 1$, $|\tilde{\alpha}| = 10$, $k = 3$ and $j = 2$, in order to show the periodicity of this state and its period. The values $\tilde{\varphi} = 0$ and $\omega_c^* = 1$ were taken.

Chapter 5

Polar coherent states for bilayer graphene

The main goal of this chapter is to complete the study of the bilayer graphene in a constant magnetic field, now using a symmetric gauge and polar coordinates, instead of the Landau gauge used in previous studies. Specifically, the current densities of bilayer graphene will be derived in detail and calculated for both the eigenstates of the system and for the radially symmetric coherent states, which will be also constructed in this chapter as eigenstates of an appropriate annihilation operator with a complex eigenvalue α^2 [70].

5.1 Bilayer graphene Hamiltonian in a symmetric gauge

As it is well known, the Hamiltonian characterizing the electronic behavior in a bilayer graphene structure placed on the x-y plane is given by equation (2.9). Now using the symmetric gauge, the vector potential is given by

$$\mathbf{A} = \left(-\frac{B_0}{2}y, \frac{B_0}{2}x, 0\right), \tag{5.1}$$

such that $\mathbf{B} = \nabla \times \mathbf{A} = (0,0,B_0)$. The bilayer graphene Hamiltonian of equation (2.9) will take now the following form after applying the minimal coupling rule

$$H_{\text{eff}} = \frac{1}{2m^*}\begin{pmatrix} 0 & \left[p_x - \frac{eB_0}{2c}y - i\left(p_y + \frac{eB_0}{2c}x\right)\right]^2 \\ \left[p_x - \frac{eB_0}{2c}y + i\left(p_y + \frac{eB_0}{2c}x\right)\right]^2 & 0 \end{pmatrix}. \tag{5.2}$$

Let us define the following scalar operators

$$\mathscr{A}^{\pm} := \sqrt{\frac{c}{2\hbar e B_0}}\left[p_x - \frac{eB_0}{2c}y \pm i\left(p_y + \frac{eB_0}{2c}x\right)\right], \tag{5.3}$$

which satisfy the commutation relations

$$[\mathscr{A}^-, \mathscr{A}^+] = \mathscr{I}, \qquad \mathscr{A}^- = (\mathscr{A}^+)^\dagger, \tag{5.4}$$

where $\mathscr{I}$ is the identity operator. Note that the set $\{\mathscr{A}^+, \mathscr{A}^-, \mathscr{I}\}$ generates a Heisenberg (or boson) algebra.

It is more convenient to work in polar coordinates since the system has rotational symmetry around the z-axis. Thus, changing to normalized polar coordinates (χ,θ) defined by

$$x = r\cos\theta, \quad y = r\sin\theta, \qquad \chi := \sqrt{\frac{m^*\omega_c^*}{2\hbar}}\, r, \tag{5.5}$$

where ω_c^* is the cyclotron frequency for non-relativistic electrons with effective mass m^*, the operators $\mathscr{A}^{\pm}$ in equation (5.3) are rewritten as follows,

$$\mathscr{A}^{\pm} = \frac{\pm i\exp(\pm i\theta)}{2}\left[\mp\partial_\chi - \frac{i}{\chi}\,\partial_\theta + \chi\right]. \tag{5.6}$$

Thus, the time-independent Dirac-type equation for Hamiltonian (5.2) becomes

$$H_{\text{eff}}\,\Psi(\chi,\theta) = \hbar\omega_c^*\begin{pmatrix} 0 & (\mathscr{A}^-)^2 \\ (\mathscr{A}^+)^2 & 0 \end{pmatrix}\Psi(\chi,\theta) = E\Psi(\chi,\theta). \tag{5.7}$$

As in the case of the Landau gauge, the eigenstates $\Psi(\chi,\theta)$ are the two-component spinors

$$\Psi(\chi,\theta) = \begin{pmatrix} \psi^a(\chi,\theta) \\ \psi^b(\chi,\theta) \end{pmatrix}, \tag{5.8}$$

which, when substituted in equation (5.7), generate the two coupled scalar equations

$$(\mathscr{A}^+)^2\psi^a(\chi,\theta) = \varepsilon\,\psi^b(\chi,\theta), \tag{5.9}$$

$$(\mathscr{A}^-)^2\psi^b(\chi,\theta) = \varepsilon\,\psi^a(\chi,\theta), \tag{5.10}$$

with $\varepsilon := E/\hbar\omega_c^*$. We square the effective Hamiltonian (5.7), to decouple the previous equations obtaining the following two eigenvalue equations

$$\mathscr{H}_1\psi^a(\chi,\theta) = \varepsilon^2\,\psi^a(\chi,\theta), \qquad \mathscr{H}_1 := (\mathscr{A}^-)^2(\mathscr{A}^+)^2, \tag{5.11}$$

$$\mathscr{H}_2\psi^b(\xi,\theta) = \varepsilon^2\,\psi^b(\xi,\theta), \qquad \mathscr{H}_2 := (\mathscr{A}^+)^2(\mathscr{A}^-)^2. \tag{5.12}$$

In the next section we address the explicit resolution of these two equations that will allow us to find the spectrum of the bilayer graphene Hamiltonian (5.7) in the symmetric gauge.

5.1.1 Algebraic treatment and basic symmetries of $\mathscr{H}_1$ and $\mathscr{H}_2$

Taking into account the rotational symmetry of the problem, as well as the definitions (5.11)–(5.12) of the two scalar Hamiltonians $\mathscr{H}_1$ and $\mathscr{H}_2$, we define the following auxiliary operators

$$\mathscr{L}_z := -i\,\partial_\theta, \qquad \mathscr{N} := \mathscr{A}^+\mathscr{A}^-, \tag{5.13}$$

related to the angular momentum operator along the z-direction and to the number operator of the boson algebra, respectively. It is easy to check that the following commutation relations hold

$$\left[\mathscr{L}_z,\mathscr{A}^{\pm}\right] = \pm\mathscr{A}^{\pm}, \qquad \left[\mathscr{N},\mathscr{A}^{\pm}\right] = \pm\mathscr{A}^{\pm}, \qquad [\mathscr{L}_z,\mathscr{N}] = 0. \tag{5.14}$$

From $[\mathscr{A}^-,\mathscr{A}^+] = \mathscr{I}$, it is possible to express the scalar Hamiltonians $\mathscr{H}_1$ and $\mathscr{H}_2$ in terms of the number operator $\mathscr{N}$ as in equation (2.24)

$$\mathscr{H}_1 = (\mathscr{N}+2\mathscr{I})(\mathscr{N}+\mathscr{I}), \qquad \mathscr{H}_2 = \mathscr{N}(\mathscr{N}-\mathscr{I}). \tag{5.15}$$

Moreover, the operators $\mathscr{L}_z$ and $\mathscr{N}$ defined in equation (5.13) satisfy the following commutation relations

$$[\mathscr{N},\mathscr{H}_{1,2}]=0, \qquad [\mathscr{L}_z,\mathscr{H}_{1,2}]=0, \tag{5.16}$$

i.e., they are symmetries of the scalar Hamiltonians $\mathscr{H}_{1,2}$.

On the other hand, we introduce two differential operators $\mathscr{B}^{\pm}$ of variables (χ,θ) as follows

$$\mathscr{B}^{\pm}:=\frac{\pm i\exp(\mp i\theta)}{2}\left[\mp\partial_\chi+\frac{i}{\chi}\,\partial_\theta+\chi\right], \tag{5.17}$$

which, together with the operators $\mathscr{A}^{\pm}$, close the following algebra

$$[\mathscr{B}^{-},\mathscr{B}^{+}]=\mathscr{I}, \qquad \left[\mathscr{A}^{\pm},\mathscr{B}^{\pm}\right]=\left[\mathscr{A}^{\pm},\mathscr{B}^{\mp}\right]=0. \tag{5.18}$$

The operators $\mathscr{B}^{\pm}$ satisfy the following commutation relations with the symmetries $\mathscr{L}_z$ and $\mathscr{N}$

$$\left[\mathscr{L}_z,\mathscr{B}^{\pm}\right]=\mp\mathscr{B}^{\pm}, \qquad \left[\mathscr{N},\mathscr{B}^{\pm}\right]=0. \tag{5.19}$$

Thus, we constructed two Heisenberg algebras, generated by $\mathscr{A}^{\pm}$ and $\mathscr{B}^{\pm}$, which are related by an inversion in the variable θ, *i.e.*,

$$\mathscr{B}^{\pm}=\mathscr{P}\mathscr{A}^{\pm}\mathscr{P}, \tag{5.20}$$

where $\mathscr{P}\psi(\chi,\theta)=\psi(\chi,-\theta)$.

In the same way as the definition of $\mathscr{N}$ is associated with operators $\mathscr{A}^{\pm}$, we can introduce another number operator $\mathscr{M}$ associated with operators $\mathscr{B}^{\pm}$, which fulfills

$$\mathscr{M}:=\mathscr{B}^{+}\mathscr{B}^{-} \quad\Longrightarrow\quad \left[\mathscr{M},\mathscr{B}^{\pm}\right]=\pm\mathscr{B}^{\pm}, \quad [\mathscr{M},\mathscr{H}_{1,2}]=0. \tag{5.21}$$

Therefore, we have arrived at three operators $\mathscr{L}_z,\mathscr{M},\mathscr{N}$ that commute to each other, and with $\mathscr{H}_{1,2}$, although they are not all independent, because

$$\mathscr{N}-\mathscr{M}=-i\partial_\theta=\mathscr{L}_z. \tag{5.22}$$

In this context, since $\mathscr{N}$, $\mathscr{L}_z$, $\mathscr{M}$ and $\mathscr{H}_{1,2}$ commute, it is possible to look for simultaneous eigenfunctions of all of them. Consequently, the eigenstates $\psi^{a,b}(\chi,\theta)$ of the scalar Hamiltonians $\mathscr{H}_{1,2}$ can be labeled by two positive integers n, $m\in\mathbb{Z}^{+}\cup\{0\}$, associated with the eigenvalues of the numbers operators $\mathscr{N}$ and $\mathscr{M}$, respectively. Thus, by defining $\psi^{a,b}:=\psi_{n,m}$ we obtain

$$\mathscr{N}\psi_{n,m}=n\psi_{n,m}, \qquad \mathscr{M}\psi_{n,m}=m\psi_{n,m}, \qquad \mathscr{L}_z\psi_{n,m}=(n-m)\psi_{n,m}, \qquad n,m=0,1,2,\ldots \tag{5.23}$$

with a well-defined value of the angular momentum $\ell_z=n-m$.

The eigenfunctions $\psi_{n,m}(\chi,\theta)$ can be obtained from the ground state $\psi_{0,0}$ by the successive action of the appropriate creation operators, *i.e.*,

$$\psi_{n,m}(\chi,\theta)=\frac{1}{\sqrt{m!\,n!}}(\mathscr{B}^{+})^m(\mathscr{A}^{+})^n\psi_{0,0}(\chi,\theta), \tag{5.24}$$

such that

$$\mathscr{B}^{-}\psi_{0,0} = \mathscr{A}^{-}\psi_{0,0} = 0. \tag{5.25}$$

Note that they lead to two separable differential equations in the variables χ and θ which can be explicitly solved to obtain

$$\psi_{0,0}(\chi,\theta) = C_{0,0}\exp\left(-\xi^2/2\right), \tag{5.26}$$

where $C_{0,0}$ is the corresponding normalization constant.

After some calculations, we find that the normalized eigenfunctions $\psi_{n,m}(\chi,\theta)$, $n,m = 0,1,2\ldots$, turn out to be

$$\psi_{n,m}(\chi,\theta) = \sqrt{\frac{m^*\omega_c^*}{2\pi\hbar}\frac{\min(n,m)!}{\max(n,m)!}}\, i^{n+m}(-1)^{\min(n,m)}\exp\left[-\frac{\chi^2}{2} - i(m-n)\theta\right]\chi^{|m-n|}L_{\min(n,m)}^{|m-n|}(\chi^2), \tag{5.27}$$

where $L_k^{\alpha}(x)$ are the associated Laguerre polynomials. Taking into account (5.15), the functions $\psi_{n,m}(\chi,\theta)$ are also eigenfunctions of the scalar Hamiltonians $\mathscr{H}_{1,2}$, *i.e.*,

$$\mathscr{H}_1\psi_{n,m} = (n+2)(n+1)\psi_{n,m}, \qquad \mathscr{H}_2\psi_{n,m} = n(n-1)\psi_{n,m}, \qquad n,m = 0,1,2,\ldots \tag{5.28}$$

Thus, the eigenfunctions $\psi_{n,m}$ can play the roles of both the upper component ψ^a, as well as the lower component ψ^b of the spinor $\Psi(\chi,\theta)$ in equation (5.8). Therefore, as in the case of the Landau gauge for $n \geq 2$ the solutions are [70]:

$$\Psi_{n,m}^{\pm}(\chi,\theta) := \frac{1}{\sqrt{2}}\begin{pmatrix}\psi_{n-2,m}(\chi,\theta)\\ \pm\psi_{n,m}(\chi,\theta)\end{pmatrix}, \quad E_n^{\pm} = \pm\hbar\omega_c\sqrt{n(n-1)}, \quad n = 2,3,\ldots, \tag{5.29}$$

and the fundamental zero-energy solutions with $n = 0,1$ are

$$\Psi_{0,m}^{\pm}(\chi,\theta) := \begin{pmatrix}0\\ \pm\psi_{0,m}(\chi,\theta)\end{pmatrix}, E_0^{\pm} = 0, \qquad \Psi_{1,m}^{\pm}(\chi,\theta) := \begin{pmatrix}0\\ \pm\psi_{1,m}(\chi,\theta)\end{pmatrix}, E_1^{\pm} = 0. \tag{5.30}$$

5.1.2 Probability and current densities for the energy eigenstates $\Psi_{n,m}^{\pm}(\chi,\theta)$

Probability density

The radial probability density $\rho_{n,m}(\chi,\theta)$ is defined in the usual way for eigenfunctions $\Psi_{n,m}^{\pm}(\chi,\theta)$. In the present case it can be written as follows

$$\rho_{n,m}(\chi) = \left(\Psi_{n,m}^{\pm}(\chi,\theta)\right)^{\dagger}\Psi_{n,m}^{\pm}(\chi,\theta) = \frac{(1-\delta_{n0}-\delta_{n1})|\psi_{n-2,m}(\chi,\theta)|^2 + |\psi_{n,m}(\chi,\theta)|^2}{2^{(1-\delta_{n0}-\delta_{n1})}}, \quad n = 0,1,2,\ldots \tag{5.31}$$

Taking into account equation (5.27), it is clear that this expression does not depend on the angular variable θ, and it is the same for positive and negative energy eigenfunctions $\Psi_{n,m}^{\pm}(\chi,\theta)$. Figure 5.1 shows the probability density (5.31) for $n = 2$ and several values of the index m. As m increases, the centrifugal force induces the density to move away from the origin. However, when the value of the angular momentum $\ell_z = n - m$ is equal to or close to zero, the probability density for the energy eigenstates of bilayer graphene is mainly centered at the origin. The radial symmetry of the magnitude under analysis is evident in the plots.

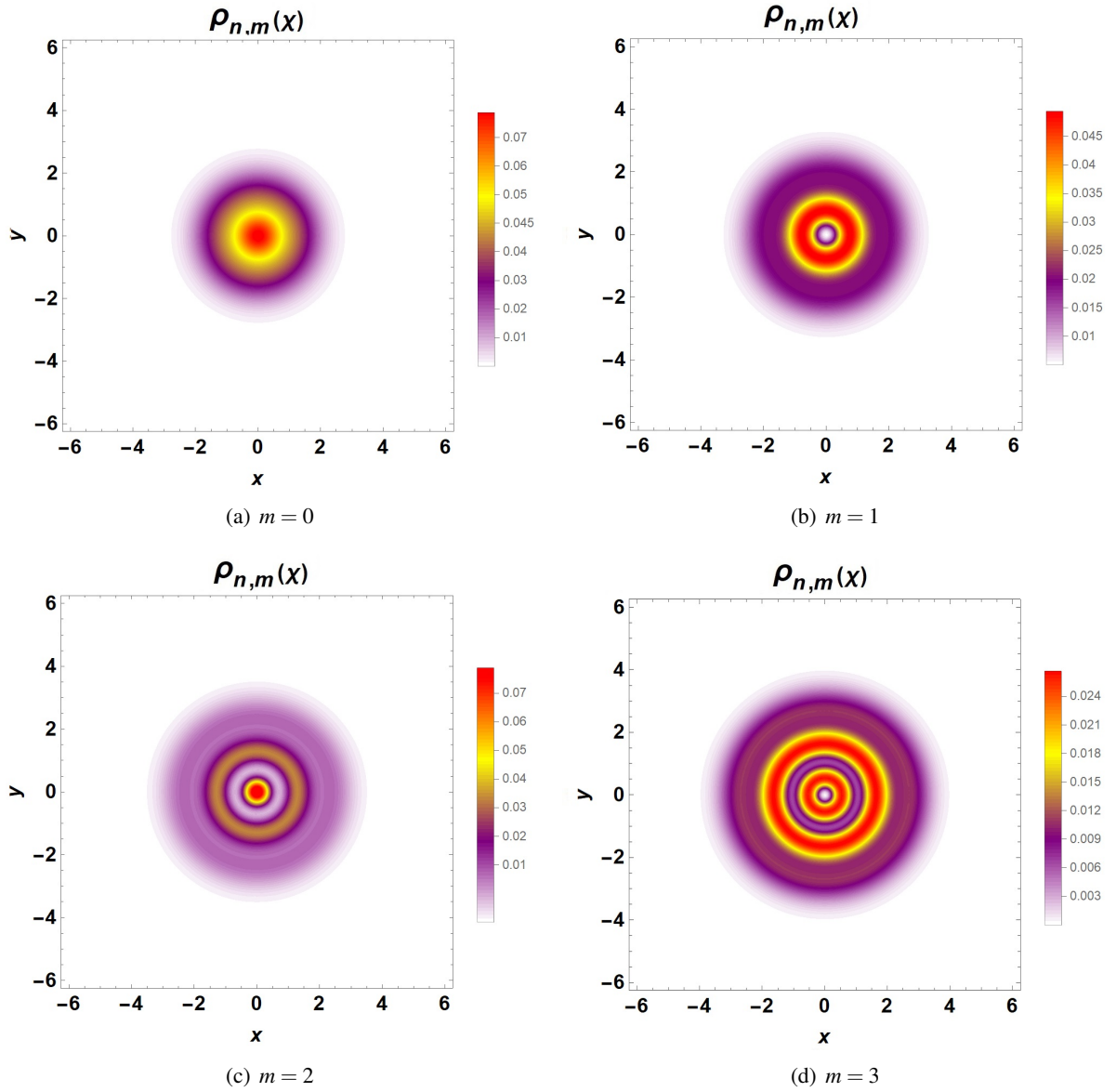

(a) $m = 0$ (b) $m = 1$

(c) $m = 2$ (d) $m = 3$

Figure 5.1: Probability density (5.31) for the eigenstates $\Psi^{\pm}_{n,m}(\chi,\theta)$ with for $n = 2$ and different values of m. The colors indicate the different values such a density can take.

Current density

In the polar coordinates of the present chapter, the components $k = \chi, \theta$ of the current density operator are denoted as (j_χ, j_θ). Remember that in polar coordinates the divergence of a generic vector field $\mathbf{V} = (V_\chi, V_\theta)$, which must be appear in the continuity equation (2.35), is given by

$$\nabla \cdot \mathbf{V} = \frac{1}{\chi}\frac{\partial}{\partial \chi}(\chi V_\chi) + \frac{1}{\chi}\frac{\partial}{\partial \theta}(V_\theta).$$

Then, the same procedure applied to Cartesian coordinates (2.32) leads to the components j_k of the current density in polar coordinates, given by

$$j_\chi = i\begin{pmatrix} 0 & e^{-i\theta}\mathscr{A}^- \\ e^{i\theta}\mathscr{A}^+ & 0 \end{pmatrix}, \qquad j_\theta = \begin{pmatrix} 0 & e^{-i\theta}\mathscr{A}^- \\ -e^{i\theta}\mathscr{A}^+ & 0 \end{pmatrix}, \tag{5.32}$$

where $\mathscr{A}^\pm$ are the operators in (5.6).

In this way, the radial and tangential current densities for the energy eigenstates of the bilayer graphene Hamiltonian can be calculated by applying the operators (5.32) to the states $\Psi^\pm_{n,m}(\chi,\theta)$. The main result is the following

$$J_\chi[\Psi^\pm_{n,m}] = 0, \qquad J_\theta(\xi)[\Psi^\pm_{n,m}] \neq 0, \qquad n \geq 2, \tag{5.33}$$

As can be seen, the radial current always disappears, while the tangential one remains non-zero and, in fact, depends only on the radius χ for each eigenspinor. To illustrate these results, figure 5.2 shows some plots of its behavior for $n = 2$ and different values of index m. It is important to emphasize that the results are independent of both the angular variable θ and the sign $(\pm)$ of the energy. However, states with angular momentum $\ell_z < 2$ produce an angular probability current with a strongly oscillating shape. This indicates the existence of rings in the bilayer graphene where the current density rotates either clockwise $(J_\theta < 0)$ or counterclockwise $(J_\theta > 0)$.

After studying both the symmetries and the various physical properties of the Hamiltonian eigenstates of bilayer graphene, in the next section we will go one step further, by calculating the coherent states that naturally appear for the bilayer graphene Hamiltonian and discussing how the symmetry operators can help us to interpret them.

5.2 Polar coherent states of bilayer graphene

We are going to construct the coherent states of the bilayer graphene Hamiltonian H_{eff} (5.2). We will adopt the standard approach in which the coherent states are eigenstates of an annihilation operator that must be chosen appropriately according with the system Hamiltonian. Thus, the coherent states $\Psi_\alpha(\chi,\theta)$, of the bilayer graphene Hamiltonian H_{eff} will be eigenstates of an annihilation operator $\mathbb{A}^-$, to be defined later, with a complex eigenvalue that depends on the complex number α. Since each energy eigenspinor $\Psi^\pm_{n,m}$ involves the scalar wave functions $\psi_{n,m}$ and $\psi_{n-2,m}$, it seems natural to define the operator $\mathbb{A}^-$ through its action onto the eigenstates $\Psi^\pm_{n,m}(\chi,\theta)$ of equations (5.29)–(5.30) as follows:

$$\mathbb{A}^-\Psi^\pm_{n,m}(\chi,\theta) = g(n)\,\Psi^\pm_{n-2,m}(\chi,\theta), \tag{5.34}$$

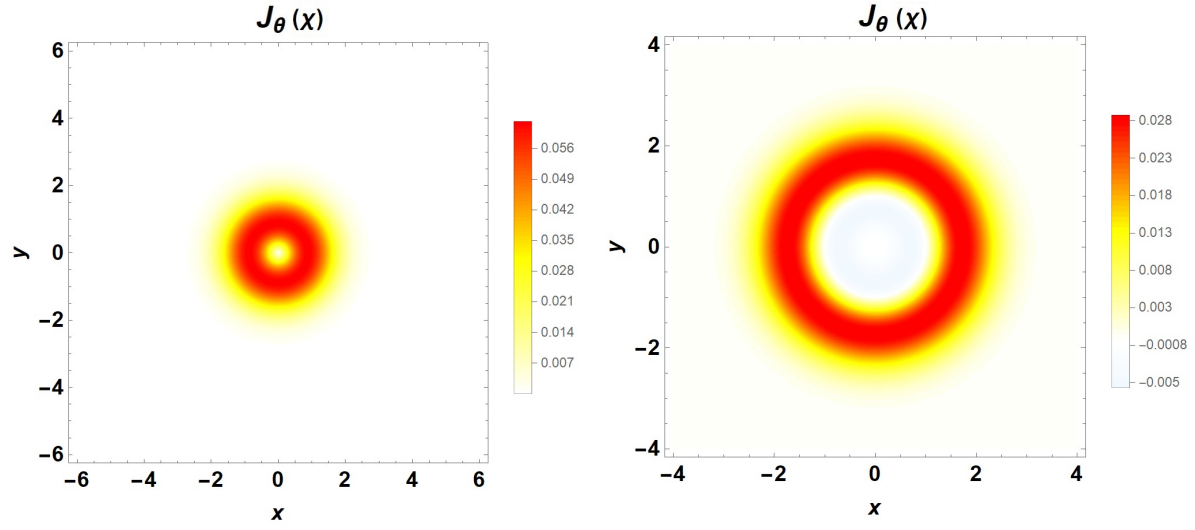

(a) $n = 2, m = 0$ (b) $n = 2, m = 1$

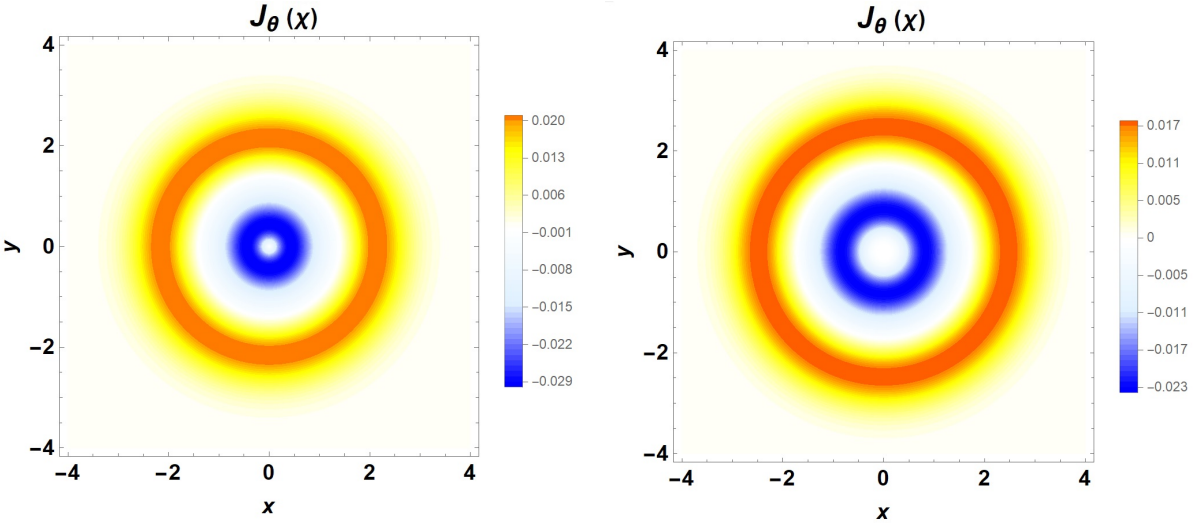

(c) $n = 2, m = 2$ (d) $n = 2, m = 3$

Figure 5.2: Current density $J_\theta(\chi)$ for the eigenstates $\Psi^{\pm}_{n,m}(\chi,\theta)$ with $n = 2$ and $m = 0,1,2,3$.

where $g(n)$ is a function to be determined. We will assume that our coherent state will have a constant value of the integer m in equation (5.34), thus we will add to it the corresponding subscript,

$$\mathbf{M}\Psi_{\alpha,m} = m\Psi_{\alpha,m},$$

where $\mathbf{M}$ is given by $\mathbf{M} = \mathscr{M}\,\mathbf{I}$.

Other options could have been chosen [41,45], *e.g.*, coherent states with a fixed angular momentum eigenvalue or with a given value of the energy. However, our purpose here is to show, as an example, how to apply the symmetry operators in the context of the bilayer graphene coherent states.

Due to the fact that the bilayer graphene Hamiltonian (5.7) involves squared scalar creation and annihilation operators $(\mathscr{A}^{\pm})^2$, which act onto the scalar components of $\Psi^{\pm}_{n,m}$, the eigenvalue of $\mathbb{A}^-$ when acting on the coherent state $\Psi^{\pm}_{\alpha,m}$ is taken to be α^2, instead of the usual α value (in other words, this choice is suggested by the "two-electron" character of the bilayer graphene Hamiltonian):

$$\mathbb{A}^-\,\Psi^{\pm}_{\alpha,m}(\chi,\theta) = \alpha^2\,\Psi^{\pm}_{\alpha,m}(\chi,\theta), \qquad \alpha\in\mathbb{C}. \tag{5.35}$$

After these considerations, a coherent state will have the following general decomposition

$$\Psi^{\pm}_{\alpha,m}(\chi,\theta) = \sum_{n=0}^{\infty} a_n \Psi^{\pm}_{n,m}(\chi,\theta), \tag{5.36}$$

with certain complex coefficients a_n. Note that the coherent states in equation (5.36) also include a sign $\pm$ to distinguish between states with positive or negative energy built from positive or negative energy eigenfunctions respectively. Plugging this expression in to equation (5.35) and using (5.34), we get

$$\sum_{n=0}^{\infty}\left(g(n+2)a_{n+2} - \alpha^2 a_{2n}\right)\Psi^{\pm}_{n,m}(\chi,\theta) = 0. \tag{5.37}$$

Given that the states $\Psi^{+}_{n,m}(\chi,\theta)\neq 0$, are linearly independent $\forall n$, from the above equation we arrive at two independent recurrence relations for the coefficients a_n in terms of the free coefficients $\{a_0,a_1\}$:

$$a_{2n} = \frac{\alpha^{2n}}{[g(2n)]!!}a_0, \quad a_{2n+1} = \frac{\alpha^{2n}}{[g(2n+1)]!!}a_1, \qquad n=0,1,2,\ldots, \tag{5.38}$$

where

$$[g(2n)]!! := \begin{cases} 1, & \text{for } n=0,\\ g(2)\cdots g(2n), & \text{for } n>0,\end{cases} \qquad [g(2n+1)]!! := \begin{cases} 1, & \text{for } n=0,\\ g(3)\cdots g(2n+1), & \text{for } n>0.\end{cases} \tag{5.39}$$

Among the several possibilities to choose the function $g(n)$, there is natural one, given the structure that these functions have in equation (5.39), *i.e.*, $g(n) = \sqrt{n(n-1)}$. With this choice, the two sets of normalized coherent states that arise by taking only odd or even indices, denoted respectively as $\Psi^{e\pm}_{\alpha,m}(\chi,\theta)$ and $\Psi^{o\pm}_{\alpha,m}(\chi,\theta)$, are given by

$$\Psi^{e\pm}_{\alpha,m}(\chi,\theta) = \frac{1}{\sqrt{\cosh(|\alpha|^2)}}\left[\Psi^{\pm}_{0,m}(\chi,\theta) + \sum_{n=1}^{\infty}\frac{\alpha^{2n}}{\sqrt{(2n)!}}\Psi^{\pm}_{2n,m}(\chi,\theta)\right], \tag{5.40}$$

$$\Psi^{o\pm}_{\alpha,m}(\chi,\theta) = \frac{1}{\sqrt{\sinh(|\alpha|^2)/|\alpha|^2}}\left[\Psi^{\pm}_{1,m}(\chi,\theta) + \sum_{n=1}^{\infty}\frac{\alpha^{2n}}{\sqrt{(2n+1)!}}\Psi^{\pm}_{2n+1,m}(\chi,\theta)\right], \tag{5.41}$$

where both, the explicit form of the eigenstates (5.29)–(5.30) and their normalization (5.27), have been taken into account.

5.2.1 Expectation values

An important point of a coherent state is the interpretation of the complex parameter α on which it depends in terms of its position (also in its momentum, but this will not be discussed here). Thus, we will start by finding the expectation value of χ^2 in one of the coherent states derived above. To do this we start by expressing χ^2 in terms of the scalar symmetry operators $\mathscr{A}^{\pm}$ and $\mathscr{B}^{\pm}$. From equations (5.6) and (5.17) we obtain

$$\chi^2 = (\mathscr{A}^+ - \mathscr{B}^-)(\mathscr{A}^- - \mathscr{B}^+). \tag{5.42}$$

Therefore, it is possible to calculate the expectation value of χ^2 for instance in the even and positive energy coherent states (5.40) as follows

$$\langle \chi^2 \rangle_{\alpha,m} = \langle \Psi^{e\pm}_{\alpha,m} | (\mathscr{A}^+ - \mathscr{B}^-)(\mathscr{A}^- - \mathscr{B}^+) \mathbf{I} | \Psi^{e\pm}_{\alpha,m} \rangle. \tag{5.43}$$

Note that exactly the same calculation can be done for the odd coherent states. Thus, after performing the integration over the spatial variables and simplifying, the expected value of χ^2 turns out to be

$$\langle \chi^2 \rangle^e_{\alpha,m} = \frac{1}{\cosh(|\alpha|^2)} \left[\sum_{n=1}^{\infty} \frac{|\alpha|^{4n}}{(2n)!}(2n-1) \right] + (m+1). \tag{5.44}$$

In particular, for $m = 0$ this expectation value becomes

$$\langle \chi^2 \rangle^e_{0,\alpha} = 1 + |\alpha|^2 \tanh(|\alpha|^2). \tag{5.45}$$

Thus, when $|\alpha| \gg 1$ the expected value $\langle \chi^2 \rangle$ tends to $|\alpha|^2$, consequently we can say that in this limit the radial coordinate χ is approximated by $|\alpha|$. Note that although the particular case with $m = 0$ has been taken, similar formulas apply for any m.

Similarly, in order to obtain information about the phase φ of the coherent state, with $\alpha = |\alpha| e^{i\varphi}$, we make use of the expression

$$-\chi^2 \exp(2i\theta) = \left(\mathscr{A}^+ - \mathscr{B}^- \right)^2. \tag{5.46}$$

Therefore, the expectation value of this quantity in the even coherent states $\Psi^{e\pm}_{\alpha,m}(\chi,\theta)$ for a fixed arbitrary m is

$$\langle -\chi^2 \exp(2i\theta) \rangle^{e\pm}_{\alpha,m} = \frac{(\alpha^*)^2}{\cosh(|\alpha|^2)} \left[\frac{1}{\sqrt{2}} + \frac{1}{2} \sum_{n=1}^{\infty} \frac{|\alpha|^{4n}}{(2n)!} + \frac{1}{2} \sum_{n=1}^{\infty} \frac{|\alpha|^{4n}}{\sqrt{(2n-2)!(2n+2)!}} \right]. \tag{5.47}$$

Using this expression and the previous result (5.44) we can substitute α^* by $\chi \exp(i\theta + \pi/2)$. Thus, it can be concluded that there is a relationship between the coordinate θ and the phase φ of the complex eigenvalue α given by $\theta + \pi/2 = -\varphi$.

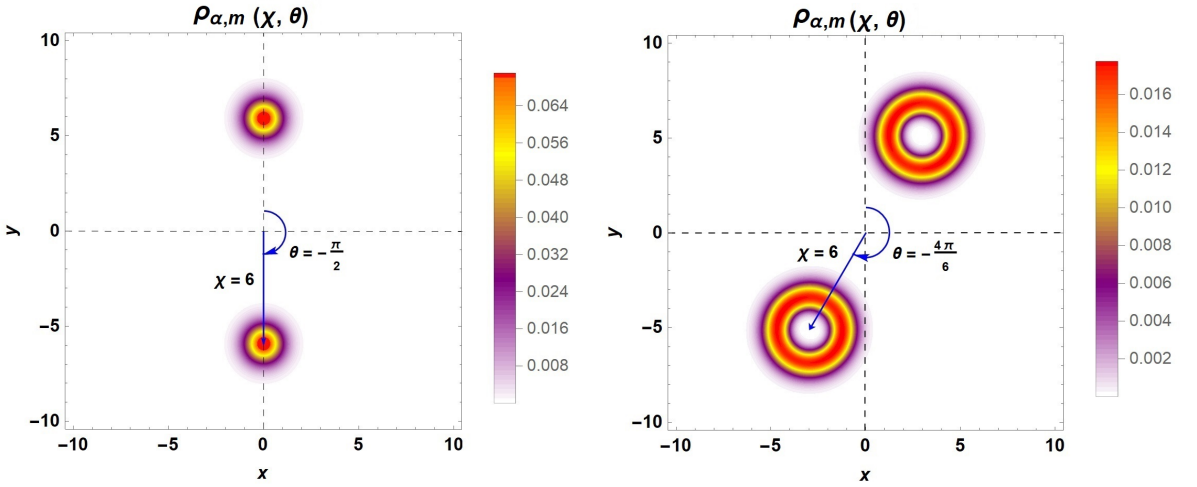

(a) $|\alpha| = 6,\ m = 0,\ \varphi = 0$ (b) $|\alpha| = 6,\ m = 3,\ \varphi = \pi/6$

Figure 5.3: Probability density for the even coherent states with $m = 0, 3$, and different values of α. To avoid too cumbersome notation, and since only even coherent states built with eigenstates of positive energy are shown, this probability density is denoted simply by $\rho_{\alpha,m}(\chi,\theta)$.

5.2.2 Probability and current densities

Probability density

The probability density for the coherent states (5.40)–(5.41) is calculated in the same way as for any other state, using equation (5.31). For example, for the even coherent state it turns out that

$$\rho^{e\pm}_{\alpha,m}(\chi,\theta) = \left(\Psi^{e\pm}_{\alpha,m}(\chi,\theta)\right)^{\dagger} \Psi^{e\pm}_{\alpha,m}(\chi,\theta). \tag{5.48}$$

To illustrate the structure of the probability densities for the even coherent states, the expression (5.48) is plotted in figure 5.3 for certain values of $\alpha = |\alpha|\exp(i\varphi)$ with $m = 0$ and $m = 3$. In addition, the results obtained above for the expectation values (see subsection 5.2.1) are as well illustrated. As we can see, for $|\alpha| \gg 1$ the value for the θ polar-coordinate of the position of the coherent state is related with the phase of the complex number α as $\theta = -\varphi - \pi/2$ and the χ-radial coordinate of such position matches the previous calculations in the same limit $\chi = |\alpha|$.

Current density

The current densities can be also calculated for the coherent states derived in this section, for which it is enough to use expression (5.32). In this case we restrict ourselves to the even coherent states $\Psi^{e\pm}_{\alpha,m}(\chi,\theta)$. The resulting algebraic expressions are too complicated and they do not supply much information on their own. What it is interesting is to analyze their plots, which illustrate better their physical meaning. Therefore, figure 5.4 shows the radial and angular current densities, denoted simply as J_χ and J_θ, in a sufficiently illustrative specific case. The most interesting feature is the behavior of the radial component J_χ of the density current. In plots (a) and (c) of figure 5.4 two separate regions are displayed with positive and negative values (red and blue colors). However, this feature is not present in the angular component

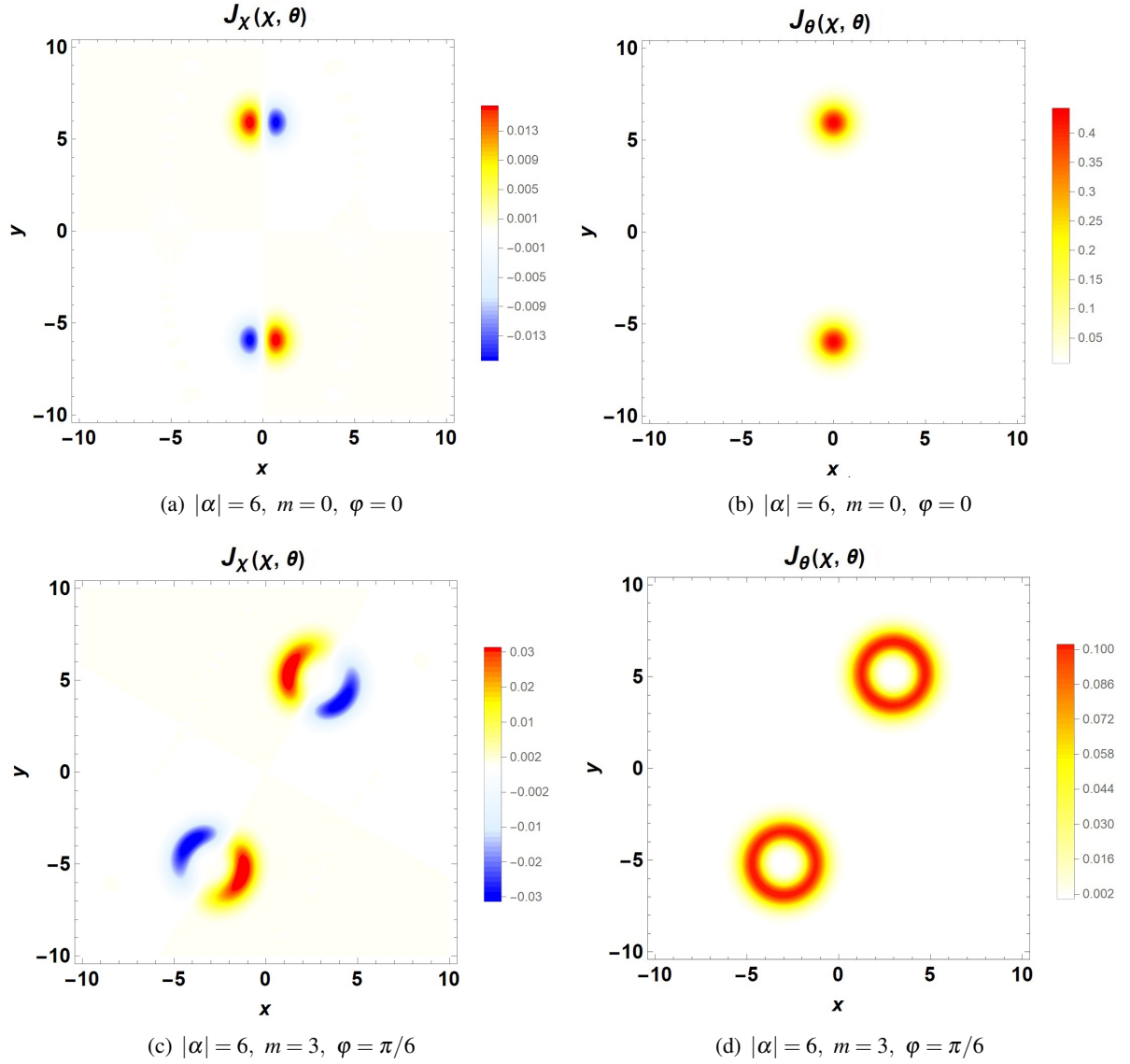

(a) $|\alpha| = 6,\ m = 0,\ \varphi = 0$ (b) $|\alpha| = 6,\ m = 0,\ \varphi = 0$

(c) $|\alpha| = 6,\ m = 3,\ \varphi = \pi/6$ (d) $|\alpha| = 6,\ m = 3,\ \varphi = \pi/6$

Figure 5.4: Radial current density $J_\chi(\chi,\theta)$ and angular current density $J_\theta(\chi,\theta)$ for the even coherent states with $m = 0, 3$, and different values of the complex number α.

J_θ of the current density. This rather strange behavior of J_χ can be explained by expression (5.32) for both components J_χ and J_θ. In these expressions there are two exponentials $e^{\pm i\theta}$ that cause this split into two parts. Bilayer graphene coherent states have this property only for the radial component J_χ. However, this is not specific of bilayer graphene, since it is also present in monolayer graphene or even in polar coherent states for non-relativistic systems in the plane.

Chapter 6

Conclusions

In this work, a detailed analysis of the interaction between electrons in bilayer graphene and a constant, homogeneous magnetic field perpendicular to its surface has been carried out. Starting from the effective Hamiltonian that characterizes this interaction, the energies and eigenfunctions of the system have been determined using the standard quantum-mechanical approach. A fundamental difference between monolayer and bilayer graphene has been identified in terms of nature of their electrons in the low energy regime. In particular, while in monolayer graphene the electrons behave as massless chiral particles with a linear dispersion relation, in bilayer graphene they behaves as chiral electrons with an effective mass m^* and a parabolic dispersion relation [19]. Moreover, when considering the interaction of monolayer and bilayer graphene with an external magnetic field, another significant difference (perhaps the most relevant one) arises, which is related with their energy spectrum or Landau levels. These levels clearly define the differences between the dynamics of each system when considering the time evolution.

In this way, with the aim of analyzing this quantum system through a different approach from the standard one, coherent states associated with this system have been constructed, which we call bilayer graphene coherent states (BGCS). These states have been derived as eigenstates of a matrix annihilation operator involving an arbitrary function f of the number operator N, thus it is possible to construct different sets of coherent states depending on the choice of such a function. These states were derived in our previous work [50], where we also analyzed their physical properties. However, this thesis focuses on the dynamics of the BGCS, thus we notice that, since the Landau levels for bilayer graphene are approximately equidistant for $n \gtrsim 2$, the time evolution is stable for BGCS such that their linear combination with $n \gtrsim 2$ approximates such a state (see figure 3.3), as the standard coherent states [46], with the same period as the involved harmonic oscillator ($\tau = 2\pi/\omega_c^*$). However, for BGCS where the relative contribution of the eigenstates $\Psi_0^+(x,y)$ and $\Psi_1^+(x,y)$ is significant, the time evolution turns out to be quasi-stable, as can be seen in figures 3.1 and 3.2. This work also presents a method for estimating the evolution period of such states (see equation (3.28)), which exhibit quasi-classical behavior (see figures 3.1(b)- 3.3(b)).

On the other hand, it is possible to analyze the so-called revival structure in quantum systems where a quasi-periodicity exists. This involves to study the motion of localized wave packets. Let us note that in most situations such wave packets expand and contract in a sequence of collapses and revivals [52,53]. Then, to study the revival structure for BGCS, the so-called time scales were calculated. It was found that starting from a certain value of $|\alpha|$, where α is the complex eigenvalue of the BGCS, the first time scale is related to the classical motion and has a value of $T_{\text{cl}} \simeq 2\pi/\omega_c^*$, similar to the evolution period of

the associated harmonic oscillator. Meanwhile, the subsequent time scales are related to the collapse and revival of these states and take much larger values, making them irrelevant for this study. Therefore, the BGCS evolve approximately like the standard coherent states and their wave packet does not show these revivals. This highlights the importance of studying the classical limit of quantum mechanical systems through these coherent sates. These facts for the BGCS are evident in our analysis of the autocorrelation function (see figures 3.5- 3.7).

In this study we expanded upon the concept of BGCS, by deriving the multiphoton coherent states for bilayer graphene (BGMCS). Based on the annihilation operator introduced in equation (3.7), an appropriate generalized annihilation operator was first defined as $\mathbf{A}_g^- := (A^-)^k$. Subsequently, the BGMCS were obtained as eigenstates of such an operator with complex eigenvalue. Moreover, in order to analyze the system some physical quantities were obtained for such states, including the Heisenberg uncertainty relation, probability density and mean energy value. It was found that in this approach the complex eigenvalue $\tilde{\alpha}$ plays an important role, since it defines the system initial conditions.

Once again, the time evolution of the BGMCS was studied, and it was observed that the behavior is similar to that found for the BGCS. This was expected since what determines the periodicity of a quantum system is its energy spectrum. However, it is worth to notice that when studying their time evolution through time scales, the evolution period of these states becomes a fraction of the classical evolution period previously derived for the BGCS, *i.e.*, $T_{\rm cl}^{\rm BGMCS} \simeq T_{\rm cl}^{\rm BGCS}/k \simeq 2\pi/k\omega_c^*$, turning them into non-classical states. The autocorrelation function of the BGMCS illustrated in figures 4.15 and 4.16 highlights this behavior. It is important to mention that this phenomenon is also observed in the multiphoton coherent states of the harmonic oscillator derived in [59]. Meanwhile, for the BGMCS where the states $\Psi_0^+(x,y)$ and $\Psi_1^+(x,y)$ are involved in a non-trivial way, only an approximate evolution period can be obtained through equation (4.34).

Finally, the same physical system was examined using a symmetric gauge instead of the Landau gauge [70]. This approach leads us to use polar coordinates, which opens up the possibility of discovering some information about the system that is different from what is found when working in Cartesian coordinates. Thus, certain symmetries of the system were identified, and a set of polar coherent states was generated for bilayer graphene. The use of polar coordinates allowed revealing, both graphically and analytically, an interpretation of the complex parameter α labelling the coherent states (see figure 5.3). An additional important element of this study is the first-time supply of an explicit expression for the polar coordinates components of the current density for bilayer graphene in a magnetic field. We have shown that these components have a covariant and gauge-independent nature. Particular attention has been given to the behavior of the radial component of the current density for our coherent state, which appears graphically separated into two regions of opposite sign (see figure 5.4).

In conclusion, it is worth noticing that recent developments are searching for ways to implement approaches to address different types of two-dimensional systems. For example, recent studies have explored the evolution of such systems in phase-space through the Wigner function (WF) [71, 72]. In particular, in [71] the coherent states for uniaxially strained graphene with non-equidistant Landau levels were derived and the corresponding WFs were evaluated. These time-dependent WFs for the coherent states exhibit fluctuations between the classical and quantum behavior, as well as a quasi-periodic motion with time. Moreover, the Wigner function constitutes a valuable tool for contrasting the quantum and classical behaviors of the BGCS and BGMCS.

6.1 Perspectives and published works

Based on the results of our study, we can foresee the following perspectives:

- It is possible to address the dynamics of these BGCS in phase space through the Wigner function. This could give us the chance to observe the quasi-classical behavior of the previously derived BGCS and make a comparison with the BGMCS.
- Since the current density is given in terms of the $\theta^{\pm}$ operators, we have the possibility to analyze the revivals of these bilayer graphene currents in the presence a magnetic field. Furthermore, it could be investigated whether the *zitterbewegung* phenomenon occurs in bilayer graphene, as in monolayer graphene [55], when considering a superposition of states with both positive and negative Landau levels. It should be noted that in this thesis we limit ourselves to consider only positive energies.

Finally, the published works where the results presented here can be found are:

- Fernández, D.J., and Martínez-Moreno, D.I. (2020). Bilayer graphene coherent states. *Eur. Phys. J. Plus*, **135**, 739.
- Fernández, D.J., and Martínez-Moreno, D.I. (2023). Multiphoton coherent states for bilayer graphene. *Phys. Scr.*, **98**, 045219.
- Martínez-Moreno, D.I., Negro, J., and Nieto, L.M. (2023). Polar coherent states in bilayer graphene under a constant uniform magnetic field. *arXiv:2307.01213*.

Bibliography

[1] Castro Neto, A. H., Guinea, F., Peres, N. M. R., Novoselov, K. S., and Geim, A. K. (2009). The electronic properties of graphene. *Rev. Mod. Phys.*, **81**(1), 109.

[2] Katsnelson, M. I., and Nijmegen, R. U. (2012). *Graphene: Carbon in two dimensions*. (Cambridge University Press: Cambridge).

[3] Wallace, P. R. (1947). The band theory of graphite. *Phys Rev.*, **71**, 622.

[4] Novoselov, K., Geim, A., Morozov, S., Jiang, D., Dubonos, S., Grigorieva, I., and Firsov, A. (2004). Electric field effect in atomically thin carbon films. *Science*, **306**, 666.

[5] Gusynin, V. P., and Sharapov, S. G. (2005). Unconventional integer quantum Hall Effect in graphene. *Phys. Rev. Lett.*, **95**, 146801.

[6] Peres, N. M. R., Guinea, F., and Castro Neto, A. H. (2006). Electronic properties of disordered two-dimensional carbon. *Phys. Rev. B*, **73**(12), 125411.

[7] Kuru, S., Negro, J., and Nieto, L. M. (2009). Exact analytic solutions for a Dirac electron moving in graphene under magnetic fields. *J. Phys.: Condens. Matter*, **21**, 455305.

[8] Midya, B., and Fernández, D. J. (2014). Dirac electron in graphene under supersymmetry generated magnetic fields. *J. Phys. A: Math. Theor.*, **47**(28), 285302.

[9] Naumis, G. G., Barraza-Lopez, S., Oliva-Leyva, M., and Terrones, H. (2017). Electronic and optical properties of strained graphene and other strained 2D materials: A review. *Rep Prog Phys.*, **80**(9), 096501.

[10] Contreras-Astorga, A., Correa, F., and Jakubský, V. (2020). Super-Klein tunneling of Dirac fermions through electrostatic gratings in graphene. *Phys. Rev. B*, **102**, 115429.

[11] Kittel, C. (2005). *Introduction to solid state physics* (John Wiley and Sons, Inc: New York).

[12] Fuchs, J.-N., and Goerbig, M. O. (2008). *Introduction to the physical properties of graphene, Lecture notes.*

[13] Cooper, D. R., D'Anjou, B., Ghattamaneni, N., Harack, B., Hilke, M., Horth, A., Majlis, N., Massicotte, M., Vandsburger, L., Whiteway, E., and Yu, V. (2012). Experimental review of graphene. *International Scholarly Research Notices*, **2012**, 501686.

[14] Rozhkov, A. V., Sboychakov, A. O., Rakhmanov, A. L., and Nori, F. (2016). Electronic properties of graphene-based bilayer systems. *Physics Reports*, **648**, 1-104.

[15] Liu, Z., Suenaga, K., Harris, P. J. F., and Iijima, S. (2009). Open and closed edges of graphene layers. *Phys. Rev. Lett.*, **102**(1), 015501.

[16] Cao, Y., Fatemi, V., Fang, S., Watanabe, K., Taniguchi, T., Kaxiras, E., and Jarillo-Herrero, P. (2018). Unconventional superconductivity in magic-angle graphene superlattices. *Nature*, **556**, 43-50.

[17] Cao, Y., Fatemi, V., Demir, A., Fang, S., Tomarken, S. L., Luo, J. Y., Sanchez-Yamagishi, J. D., Watanabe, K., Taniguchi, T., Kaxiras, E., Ashoori, R. C., and Jarillo-Herrero, P. (2018). Correlated insulator behaviour at half-filling in magic angle graphene superlattices. *Nature*, **556**, 80.

[18] McCann, E., Abergel, D., and Fal'ko, V. I. (2007). The low energy electronic band structure of bilayer graphene. Eur. Phys. J. Spec. Top., **148**, 91-109.

[19] McCann, E., and Koshino, M. (2013). The electronic properties of bilayer graphene. *Rep. Prog. Phys.*, **76**, 056503.

[20] McCann, E., and Fal'ko, V. I. (2006). Landau-level degeneracy and quantum hall effect in a graphite bilayer. *Phys. Rev. Lett.*, **96**, 086805.

[21] Fernández, D. J., García-Muñoz, J. D., and Ortiz-Campa, D. (2020). Electron in bilayer graphene with magnetic fields leading to shape invariant potentials. *J. Phys. A: Math. Theor.* **53**, 435202.

[22] Díaz-Bautista, E., and Fernández, D. J. (2017). Graphene coherent states. *Eur. Phys. J. Plus*, **132**, 499.

[23] Ferreira, A., Gomes, J. V., Nilsson, J., Mucciolo, E. R., Peres, N. M. R., and Castro Neto, A. H. (2011). Unified description of the dc conductivity of monolayer and bilayer graphene at finite densities based on resonant scatterers. *Phys. Rev. B*, **83**(16), 165402.

[24] Klauder J. and Skagerstam B. (1985) *Coherent states: Applications in physics and mathematical physics* (World Scientific: Singapore).

[25] Perelomov A. (1986) *Generalized coherent states and their applications* (Springer-Verlag: Berlin).

[26] Ali S. T., Antoine J. P. and Gazeau J. P. (2014) *Coherent states, wavelets and their generalizations* (Springer: New York).

[27] Zettili N. (2009) *Quantum Mechanics: Concepts and applications* (Wiley: Chichester).

[28] Schrödinger E. (1926). Der stetige Übergang von der Mikro- zur Makromechanik. *Naturwissenschaften* **14** 664.

[29] Gazeau J. P. (2009) *Coherent states in quantum physics* (Wiley-VHC: Berlin).

[30] Glauber R. J. (1963). Photon correlations. *Phys. Rev. Lett.*, **10**, 84.

[31] Glauber R. J. (1963). The quantum theory of optical coherence. *Phys. Rev.*, **130**, 2529.

[32] Glauber R. J. (1963). Coherent and incoherent states of the radiation field. *Phys. Rev.*, **131**, 2766.

[33] Klauder J. R. (1963). Continuous-representation theory. *J. Math. Phys.*, **4**, 1055.

[34] Klauder J. R. (1963). Continuous-representation theory. I. Postulates of continuous-representation theory. *J. Math. Phys.*, **4**, 1058.

[35] Sudarshan E. C. G. (1963). Equivalence of semiclassical and quantum mechanical descriptions of statistical light beams. *Phys. Rev. Lett.*, **10**, 277.

[36] Howard S. and Roy S. K. (1987). Coherent states of a harmonic oscillator. *Am. J. Phys*, **55**, 1109.

[37] Barut, A.O., and Girardello, L. (1971). New "coherent" states associated with non-compact groups. *Commun. Math. Phys.*, **21**(1), 1.

[38] Gilmore, R. (1972). Geometry of symmetrized states. *Ann. Phys.*, **74**(2), 391–463.

[39] Perelomov, A.M. (1972). Coherent states for arbitrary Lie group. *Commun. Math. Phys.*, **26**(3), 222–236.

[40] Perelomov, A.M. (1975). Coherent states and symmetric spaces. *Commun. Math. Phys.*, **44**(2), 197–210.

[41] Díaz-Bautista, E., Negro, J., and Nieto, L. M. (2019). Partial coherent states in graphene. *J. Phys.: Conf. Ser.*, **1194**, 012025.

[42] Díaz-Bautista, E. (2020). Schrödinger-type 2D coherent states of magnetized uniaxially strained graphene. *J. Math. Phys.*, **61**, 102101.

[43] Castillo-Celeita, M., Díaz-Bautista, E., and Oliva-Leyva, M. (2020). Coherent states for graphene under the interaction of crossed electric and magnetic fields. *Ann. Phys.*, **421**, 168287.

[44] Motamedinasab, A., and Anbaraki, A. (2020). Superposed graphene coherent states. *Chinese J. Phys.*, **65**, 139.

[45] Díaz-Bautista, E., Negro, J., and Nieto, L. M. (2021). Coherent states in the symmetric gauge for graphene under a constant perpendicular magnetic field. *Eur. Phys. J. Plus*, **136**, 505.

[46] Gerry, C., Knight, P., and Knight, P. L. (2005). *Introductory quantum optics.* (Cambridge University Press: Cambridge).

[47] Nauenberg, M. (1989). Quantum wave packets on Kepler elliptic orbits. *Phys. Rev. A*, **40**(5), 1133.

[48] Gaeta, Z. D., and Stroud Jr., C. R. (1990). Classical and quantum-mechanical dynamics of a quasi-classical state of the hydrogen atom. *Phys. Rev. A*, **42**(6308).

[49] Wu, L. A., Murphy, M., and Guidry, M. (2017). SO(8) fermion dynamical symmetry and strongly correlated quantum Hall states in monolayer graphene. *Phys. Rev. B*, **95**, 115117.

[50] Fernández, D.J., and Martínez-Moreno, D.I. (2020). Bilayer graphene coherent states. *Eur. Phys. J. Plus*, **135**, 739.

[51] Fernández, D. J., and Ortiz-Campa, D. (2022). Graphene generalized coherent states. *Eur. Phys. J. Plus*, **137**, 1012.

[52] Bluhm, R., Kostelecký, V. A., and Porter, J. A. (1996). The evolution and revival structure of localized quantum wave packets. *Am. J. Phys.*, **64**(7), 944-953.

[53] Robinett, R. W. (2004). Quantum wave packet revivals. *Phys. Rep.*, **392**, 7-9.

[54] Yeazell, J. A., and Stroud Jr., C. R. (1988). Observation of spatially localized atomic electron wave packets. *Phys. Rev. Lett.*, **60**(15), 1494.

[55] Romera, E., and de Los Santos, F. (2009). Revivals, classical periodicity, and zitterbewegung of electron currents in monolayer graphene. *Phys. Rev. B*, **80**(16), 165416.

[56] Bužek, V., Jex, I., and Quang, T. (1990). K-photon coherent states. *J. Mod. Opt.*, **37**, 159.

[57] Bužek V. (1990). SU(1,1) squeezing of SU(1,1) generalized coherent states. *J. Mod. Opt.*, **37**, 303.

[58] Jex I. and Bužek V. (1993). Multiphoton coherent states and the linear superposition principle. *J. Mod. Opt*. **40**, 771-783.

[59] Castillo-Celeita, M., Díaz-Bautista, E., and Fernández, D. J. (2019). Polynomial Heisenberg algebras, multiphoton coherent states and geometric phases. *Phys. Scr.*, **94**, 045203.

[60] Fernández, D. J., and Hussin, V. (1999). Higher-order SUSY, linearized nonlinear Heisenberg algebras and coherent states. *J. Phys. A: Math. Gen.*, **32**, 3603-3619.

[61] Carballo, J.M., Fernández, D.J., Negro, J., and Nieto, L.M. (2004). Polynomial Heisenberg algebras. *J. Phys. A: Math. Gen.*, **37**, 10349.

[62] Bermudez, D., Contreras-Astorga, A., and Fernández, D.J. (2014). Painlevé IV coherent states. *Ann. Phys.*, **350**, 615.

[63] Fernández, D.J., and Morales-Salgado, V.S. (2016). SUSY partners of the truncated oscillator, Painlevé transcendents and Bäcklund transformations. *J. Phys. A: Math. Theor.*, **49**, 195202.

[64] Díaz-Bautista, E., and Fernández, D.J. (2019). Multiphoton supercoherent states. *Eur. Phys. J. Plus*, **134**, 61.

[65] Fernández C, D. J., and Martínez-Moreno, D. I. (2023). Multiphoton coherent states for bilayer graphene. *Phys. Scr.*, **98**, 045219.

[66] Castaños, O., López-Peña, R., and Man'ko, V.I. (1995). Crystallized Schrödinger cat states. *J. Russ. Laser. Ress*, **16**, 477.

[67] Dell'Anno, F., De Siena, S., and Illuminati, F. (2006). Multiphoton quantum optics and quantum state engineering. *Phys. Rep.*, **428**, 53.

[68] Motamedinasab, A., and Anbaraki, A. (2021). Even and odd superposition of bilayer graphene coherent states and their non-classical properties. *Phys. Scr.*, **96**, 065101.

[69] Díaz-Bautista, E., Concha-Sánchez, Y., and Raya, A. (2019). Barut–Girardello coherent states for anisotropic 2D-Dirac materials. *J. Phys.: Condens. Matter*, **31**, 435702.

[70] Martínez-Moreno, D.I., Negro, J., and Nieto, L. M. (2023). Polar coherent states in bilayer graphene under a constant uniform magnetic field. arXiv:2307.01213.

[71] Betancur-Ocampo, Y., and Díaz-Bautista, E. (2020). Phase-space representation of Landau and electron coherent states for uniaxially strained graphene. *Phys. Rev. B*, **101**, 125402.

[72] Betancur-Ocampo, Y., Díaz-Bautista, E., and Stegmann, T. (2022). Valley-dependent time evolution of coherent electron states in tilted anisotropic Dirac materials. *Phys. Rev. B*, **105**, 045401.